NUMERICAL AND EXPERIMENTAL INVESTIGATION OF INDUCTIVELY
COUPLED PLASMA CATHODE FOR ELECTRIC PROPULSION
APPLICATIONS

by

Sina Jahanbakhsh

B.S., Mechanical Engineering, Iran University of Science and Technology, 2012

Submitted to the Institute for Graduate Studies in
Science and Engineering in partial fulfillment of
the requirements for the degree of
Master of Science

Graduate Program in Mechanical Engineering
Boğaziçi University
2015

NUMERICAL AND EXPERIMENTAL INVESTIGATION OF INDUCTIVELY
COUPLED PLASMA CATHODE FOR ELECTRIC PROPULSION
APPLICATIONS

APPROVED BY:

Assist. Prof. Murat Çelik   . . . .
(Thesis Supervisor)

Assist. Prof. Jeremy Mason   . . . .

Assist. Prof. Ahmet Öncü   . . . .

DATE OF APPROVAL: 18.August.2015

ACKNOWLEDGEMENTS

ABSTRACT

NUMERICAL AND EXPERIMENTAL INVESTIGATION OF INDUCTIVELY COUPLED PLASMA CATHODE FOR ELECTRIC PROPULSION APPLICATIONS

Plasma cathodes are insert free devices that are developed to be employed as electron sources in electric propulsion applications as a practical alternative to more commonly used hollow cathodes. Inductively coupled plasma (ICP) cathode, or Radio Frequency (RF) plasma cathode, is introduced in recent years. Because of their compact geometry, and simple and efficient plasma generation, RF plasma cathodes have certain advantages over hollow cathodes. In this thesis, RF plasma cathodes have been investigated theoretically and experimentally. Extraction of electron from plasma cathode devices, and especially RF plasma cathode, strongly depends on the formation of a secondary plasma known as "anode spot." Previous Experimental studies show that the anode spot electron density and electron temperature is higher than the bulk plasma. Before the formation of the anode spot, the extracted electron current from the device is very low. By the formation of the anode spot, extracted current increases dramatically. In this thesis, it is demonstrated that the anode spot is a non-equilibrium steady state (NESS) plasma. The non-equilibrium nature of the anode spot is put forward as the reason for high electron generation and high electron density inside it. The jump in the extracted electron current is due to high electron generation inside the anode spot. Two different concepts of RF plasma cathode are designed and manufactured. Experimental measurements have been conducted to study the effects of geometric and operational parameters. Experimental studies in this thesis show that operation of the RF plasma cathode device strongly depend on the geometric parameters such as orifice diameter, chamber length, chamber diameter, antenna geometry, as well as the operational parameters such as RF power and gas mass flow rate.

ÖZET

ELEKTRİK İTKİ UYGULAMALARI İÇİN İNDÜKTİF ETKİLEŞİMLİ PLAZMA KATODUNUN NÜMERİK VE DENEYSEL ARAŞTIRMASI

Plazma katotları elektrik itki uygulamalarında elektrik kaynağı olarak daha yaygın olarak kullanılan oyuk katotlara pratik bir alternatif olarak kullanılmak için geliştirilmiş yayıcısız cihazlardır. İndüktif Etkileşimli Plazma (İEP) ya da Radyo Frekans (RF) plazma katot son yıllarda gündeme gelmiştir. Kompakt geometrileri, basit ve verimli plazma oluşumu sayesinde RF plazma katotlar oyuk katotlar üzerinde belirli avantajlara sahiptirler. Bu tezde, RF plazma katotlar ve bu cihazların çalışmasının teorik ve deneysel olarak incelenmiştir. Bilindiği gibi plazma katot cihazlarında, özellikle RF plazma katotlarda, elektron çekimi "anot noktası" olarak bilinen ikincil plazmanın oluşumuna kuvvetle bağlıdır. Literatürdeki deneysel çalışmalar anot noktası elektron yoğunluğunun ve sıcaklığının yığın plazmasından yüksek olduğunu göstermiştir. Anot noktasının oluşumundan önce cihazdan çekilen elektron akımı çok düşüktür. Anot noktasının oluşumuyla birlikte çekilen akım hızla artmaktadır. Bu tezde, anot noktasının bir dengesiz durağan durum plazması olduğu gösterilmiştir. Anot noktasının dengesiz doğası, içerisindeki yüksek elektron oluşumu ve yüksek elektron yoğunluğunun nedeni olarak öne sürülmüştür. Çekilen elektron akımındaki ani artışın sebebi anot noktasının içerisindeki yüksek elektron oluşumudur. Söz konusu ani artış bu tezde sunulan deneylerin sonuçlarında da gözlemlenmiştir. Geometrik ve operasyonel parametrelerin etkilerinin belirlenmesi için deneysel ölçümler yapılmıştır. Bu tezdeki deneysel çalışmalar RF plazma katot cihazının plazma oluşum ve elektron çekim karakteristiklerinin orifis çapı, oda uzunluğu, oda çapı, anten geometrisi gibi geometrik parametrelere, aynı zamanda RF gücü ve gazın kütlesel akış debisi gibi operasyonel parametrelere kuvvetle bağlı olduğunu göstermiştir.

TABLE OF CONTENTS

LIST OF FIGURES

LIST OF TABLES

LIST OF SYMBOLS

A	Area
as	(subscript) Anode spot
D_O	Orifice diameter
d	Gap distance
E	Energy
e	(subscript) Electrons
e	Elementary charge
F	Force
f	Velocity distribution function
g	Acceleration of gravity
g	(subscript) Gas
I	Current
I_{sp}	Specific impulse
i	(subscript) Ions
iz	(subscript) Ionization
J	Current density
k_B	Boltzmann's constant
K_{iz}	Ionization reaction rate
L	Length
m	Mass
$\dot{m}_p$	Propellant mass flow rate
N	Number
n	Number density
P	Power
Q	Heat flux
T	Temperature
th	(subscript) Thermal
u	Speed
u_B	Bohm's speed

V	Potential
V_b	Breakdown potential
V_f	Floating potential
v	Velocity
v_{ex}	Exhaust velocity
W_0	Thermal velocity of kappa distribution
α	Townsend's ionization coefficient
Γ	Particle flux
γ	Secondary electron emission rate
$\Delta\phi_{DL}$	Potential drop across double layer
κ	Kappa index
λ	Mean free path
ν	Frequency
σ	Cross section
τ	Thrust

LIST OF ACRONYMS/ABBREVIATIONS

CCP	Capacitively Coupled Plasma
DC	Direct Current
EP	Electric Propulsion
ICP	Inductively Coupled Plasma
LCIF	Laser Collision-Induced Fluorescence
MGC	Machinable Glass Ceramics
NESS	Non-Equilibrium Steady State
RF	Radio Frequency

1.   INTRODUCTION

Electric propulsion (EP) is a technology which employs electrical energy in order to accelerate the propellant and generate propulsion in spacecraft [1]. The main aim of an EP system is to convert the electric power of the spacecraft to the kinetic energy of the propellant. An electric thruster could have various operational condition such as steady or pulsed. The acceleration of the propellant could be thermal, electrostatic, electromagnetic, or mixed [2].

The most important advantage of EP is that in this type of the space propulsion the propellant is separated from the energy source, while in the chemical propulsion the energy comes from the chemical energy of the propellant itself. When the propellant is accelerated by the electrical energy, the speed of propellant could reach to many thousands of meters per second [3]. Exhaust velocity of the propellant is directly related to "specific impulse," an important parameter which determines the efficient use of the propellant. The specific impulse is defined as the ratio of the thrust to the rate of the weight of ejected propellant. The specific impulse for constant thrust and mass flow rate is defined as [1]

$$I_{sp} = \frac{\tau}{\dot{m}_p g} \tag{1.1}$$

where τ is the thrust obtained by the thruster, $\dot{m}_p$ is the mass flow rate of the propellant, and g is the acceleration of the gravity at the earth's surface. Considering that the thrust is equal to the average exhaust velocity of the propellant times its mass flow rate ($\tau = v_{ex} \dot{m}_p$), the specific impulse could also be defined as

$$I_{sp} = \frac{v_{ex}}{g} \tag{1.2}$$

This equation shows that when a thruster operates at higher propellant exhaust velocities, its specific impulse is also higher, which is the case for the EP thrusters [1]. Common types of EP thrusters are:

- *Resistojets*: Reistojets employ electrothermal heating to increase the temperature of the propellant. In this type of thrusters, a resistor element, or whole thruster chamber, are heated by electric power. The propellant is heated by passing through these parts. This heated propellant passes through a nozzle, and generates thrust. In resistejots, the propellant temperature depends on the electrothermal heating, which limits the exhaust velocity of the propellant. Hence, these types of thrusters also have limited I_{sp} values (< 500 s) [1].

- *Arcjets*: Similar to the resistojets, arcjets also employ electrothermal heating, only with a different method. In arcjets, a high current arc is generated near the nozzle of the thruster, and propellant is heated by passing through this arc. The I_{sp} of the arcjets is limited to less than about 700 s [1].

- *Ion Thrusters*: In ion thrusters, one of the plasma generation methods are used in order to ionize a large fraction of the propellant gas inside a chamber. Then, the ionized gas is accelerated through electrically biased grids. This electrostatical acceleration of the ions gives them high exhaust velocities. Due to the high exhaust velocities, ion thrusters have very high specific impulses (from 2000 s to 10000 s or higher). Also, their efficiency is the highest among different types of the thrusters [1].

- *Hall Thrusters*: In Hall effect thrusters, an electric field and a magnetic field are used perpendicularly. While the electrostatic field accelerates ions to high exhaust velocities, the magnetic field traps electrons and prevents them from streaming back to the high potential side. The trapped electrons collide with the propellant gas and ionize it. The efficiency and specific impulse of the Hall thrusters are lees than the ion thrusters. On the other hand, the thrust generation for an applied power is higher in Hall thrusters [1].

Different operational parameters for various types of thrusters are shown in Table 1.1.

1.1. Electron Sources and Ion Beam Neutralization in Ion Thrusters

There are certain number of electrons in thruster (and spacecraft with an ion thruster installed on it), because there is no ground in space to work as an infinite sink

Table 1.1. Operation parameters of different types of the thrusters [1].

Thruster	Specific Impulse	Input Power (kW)	Efficiency Rage (%)	Propellant
Cold gas	50-70	-	-	Various
Chemical (monopropellant)	150-225	-	-	N_2H_2 H_2O_2
Chemical (bipropellant)	300-450	-	-	Various
Resistojets	300	0.5-1	65-90	N_2H_4 monoprop
Arcject	500-600	0.9-2.2	25-45	N_2H_4 monoprop
Ion thruster	2500-3600	0.4-4.3	40-80	Xenon
Hall thruster	1500-2000	1.5-4.5	35-60	Xenon

or source of electrons. Ion thrusters obtain their thrust from acceleration of ions. Ions ejected from the thruster form a dense positive charged beam outside the discharge chamber. This positive beam can affect the thruster and spacecraft operation. By ejecting positive ions from the thruster, there will be extra electrons in the thruster and thus in the spacecraft, creating an unwanted electric potential that will be very harmful for spacecraft components. In addition, forming a negative potential on the surface of thruster will change the direction of the positive ions that are ejected from the discharge chamber, and this will reduce the thrust force created by ions. Also, the ions, that are ejected from the discharge chamber, create an electric field outside the chamber that prevents other ions from being ejected from the chamber, and this causes operating the thruster with less efficiency [4,5].

By considering these problems, charge neutralization outside of the discharge chamber is an important need in ion thrusters. This operation takes place by a device named neutralizer cathode (referring to its negative charge).

Neutralizer is a key element in the operation of an ion engine, and its efficient operation is important to many of thruster issues including performance (efficiency, specific impulse, stability, reliability, etc.) and lifetime [6]. A schematic of an ion thruster and its neutralizer is shown in Figure 1.1.
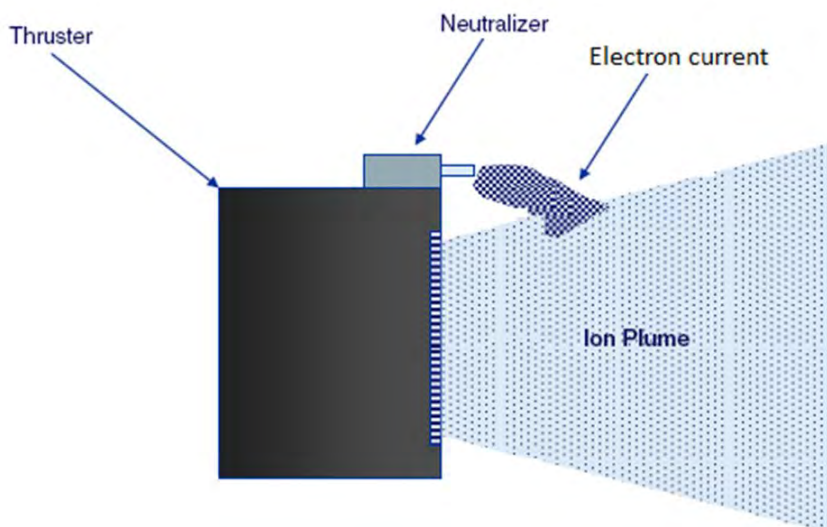
Figure 1.1. Schematic of ion thruster and its neutralizer [7].

Mixing of the electrons and ions in the neutralization process is a challenging problem. In order to neutralize both the ion charge density and ion current, the electrons that are emitted with random velocities from a small cathode on one side of the ion beam, have to spread out across the whole cross section, and also have to adapt their average velocity to the ion bulk movement [8]. This phenomenon is described as "current coupling." Actually, it is easily accomplished in practice, yet the exact process remains unknown. Currently the neutralization process is described through an "effective collision frequency" that binds electrons to the ion beam [9].

The first ion thrusters developed in 1960s (electron-bombardment ion thrusters), employed directly heated Tungsten filaments as a source of electrons in the neutralization process. But, Tungsten has a high work function, so the filaments had to be heated to a temperature as high as 2600 K to emit electron current densities on the order of 1 A/cm^2. To reach this temperature, it needs a high heater power, nearly the power that is needed to create plasma itself. This will reduce the efficiency of the thruster considerably. Also, filament's lifetime is limited by rapid evaporation of its material at the high temperature and by erosion of the tungsten surface which is bombarded by ions. This type of cathode has a lifetime of hundred hours or less [1].

To solve these problems, hollow cathodes were introduced. Hollow cathodes in-

clude a hollow refractory tube and an orifice plate on the downstream end of it. Inside the tube, there is a cylindrical insert that is pushed against the orifice plate. This insert is an active electron emitter. The material of the insert is chosen between materials that have a low work function, in order to have better electron emission. The cathode tube is covered with a heater that heats insert in order to start discharge. The electrons that are emitted from the insert have collisions with gas injected from the cathode tube, and this forms plasma inside tube. This plasma is used to extract electrons through the orifice and neutralize the thruster ion beam [1]. Typical hollow cathode geometry is shown in Figure 1.2.
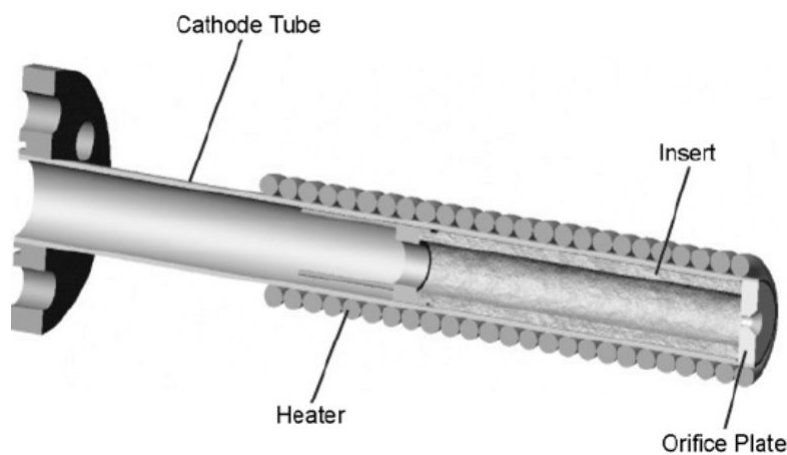
Figure 1.2. Typical hollow cathode geometry [1].

Hollow cathodes provide high electron current density by using low electric power and gas. However, they have some disadvantages. Hollow cathode's lifetime is limited by the evaporation of the insert. Actually, application of ion thrusters in the long duration space missions is very beneficial. On the other hand, the lifetime of hollow cathodes is limited by 3 or 4 years, where there is a need to a neutralizer device that can work in the 6 to 10 years missions. Also, oxygen and water impurities in the propellant can dramatically increase the evaporation operation. In addition, the insert works in a relatively high temperature and must be heated before starting the neutralizer operation. This uses a considerable power and also prevents the neutralizer from switching on or off fast [10, 11].

In order to overcome these problems, plasma cathode devices have been intro-

duced in recent years. Plasma cathodes are insert free devices that use a bulk plasma inside a chamber in order to extract electrons. Various methods have been used for bulk plasma generation in the plasma cathodes. Examples include capacitively [10] or inductively coupled [12, 13] plasma sources, which operate without magnetic fields. Other examples are electron cyclotron resonance (ECR) [14,15] and helicon [11] sources that use magnetic fields.

Helicon sources can produce the highest plasma densities for a given RF power. But, they need strong magnetic fields and high RF powers. ECR and capacitive sources do not operate efficiently in the low power and low mass flow rates that is typical for the operation of a cathode [11].

Inductively coupled plasma source is considered as one of the preferred choices for the plasma cathode device. Inductively coupled plasma cathode (RF plasma cathode) can reach to significant plasma densities (10^{16} to 10^{18} m^{-3}) and have high total electron extraction current. Because of the preferable aspects of inductively coupled plasma cathodes, several research groups have fabricated and conducted experimental research about these types of cathodes. In the next section, our goal is to introduce the works that have been done in the field of RF plasma cathode.

1.2. RF plasma Cathode

As was presented in the previous section, the idea of RF plasma cathode is to use RF fields to create plasma discharge and extract electrons from this plasma discharge. Until recently, two groups have developed RF plasma cathode and the configurations that they have used are the same in many aspects, but with some differences.

The principle of producing an ICP is shown in Figure 1.3. In ICP, an RF coil (or antenna) is used to create electromagnetic fields. These fields achieve and sustain ionization, and create plasma. During this process, the axial magnetic fields that are created by RF coil and azimuthal plasma current are coupled [16].
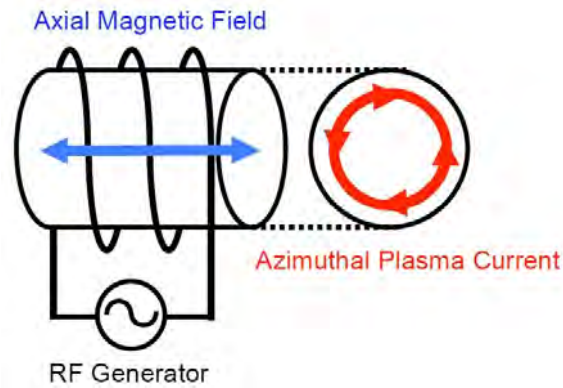
Figure 1.3. The principle of ICP formation [16].

The base configuration that the Japanese research group (from Tokyo Metropolitan University) has used is shown in Figure 1.4. The Rf plasma cathode components are:

(i) Plasma chamber that is made of Pyrex

(ii) Downstream plate that is made of Mica. This plate is used in order to sustain and increase gas pressure inside the plasma chamber.

(iii) RF coil that is wrapped around the plasma chamber

(iv) Ion collector that is used to collect and neutralize ions inside the plasma chamber. The collector is also used as an electrode to ignite the plasma.

(v) Xenon gas inlet

(vi) Electron extraction orifice in the center of Mica plate

(vii) Anode target, placed 50 mm downstream of the mica plate (Figure 1.4b) [16] [12]

Information about the size of the components is tabulated in Table 1.2.

Table 1.2. Size of components of RF plasma cathode [17].

Item	Size
Chamber Diameter	40 mm
Chamber Length	46 mm
Orifice Diameter	2 mm
Total Number of Coils	5
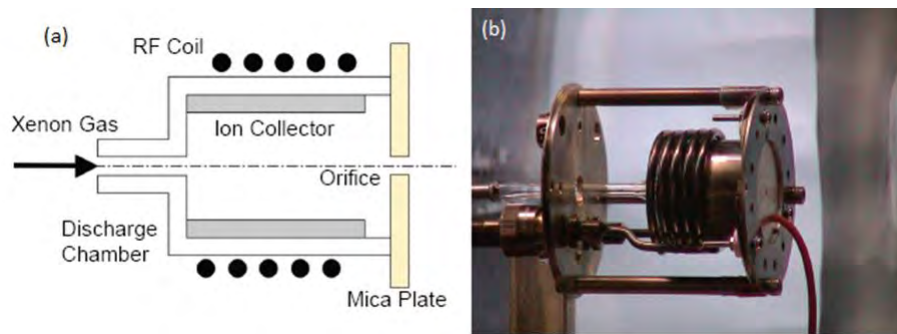
Figure 1.4. a) Schematic illustration of RF plasma cathode. b) Side view of RF plasma cathode and target [12].

Xenon gas enters the discharge chamber from inlet, and then the RF coil is used to apply RF power (at 13.56 MHz) to the gas inside the discharge chamber. By doing this, a plasma discharge will be created inside the chamber. The target plate, that is biased positively, represents the ion beam ejected from the ion thruster. So, the electrons inside the chamber move through the orifice towards the target plate. The ion collector, that is grounded to represent the potential difference between the neutralizer and the ion beam, neutralizes the ions inside the plasma. In fact, ion collector injects electrons to the plasma to compensate the electrons extracted from the plasma and hold the plasma system neutral [12].

The experimental setup used in the Japanese group's experiments is shown in Figure 1.5. The cathode system is inside a vacuum chamber. Neutral xenon gas is fed into the discharge chamber via a mass flow controller. The RF coil is connected to the RF source (13.56 MHz) through a matching network, which reduces reflected power to maximize input power to the load. The RF power creates RF electric field in the circumferential direction inside the coil. The free electrons of the system are coupled to this electric field, and then the plasma is produced [12]. Figure 1.6 shows the electrical configuration of the RF plasma cathode experiment.

The Japanese group have done experiments on this RF plasma cathode device by changing the main parameters (RF input power, mass flow rate and target voltage). The main consideration in these experiments was the electron current extraction from
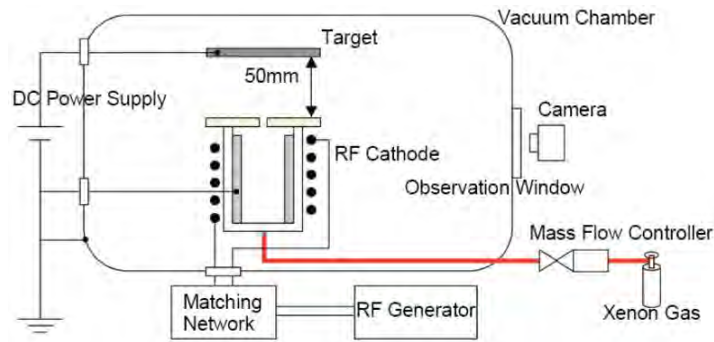
Figure 1.5. Schematic illustration of RF plasma cathode and the experimental setup [16].
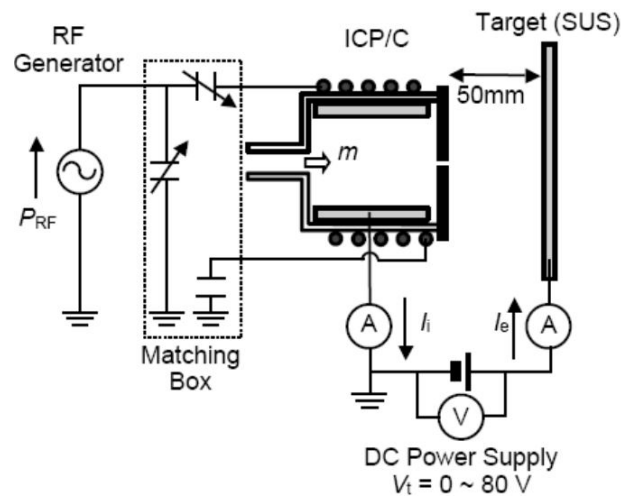
Figure 1.6. Electrical configuration of RF plasma cathode experiment [17].

the RF plasma cathode.

Experimental results for various target voltages and mass flow rates at $80W$ RF power are shown in Figure 1.7. For the small mass flow rate case, the extracted current does not change considerably. But by rising the mass flow rate, changing the target voltage has a significant influence on the extracted electron current. As can be seen from the diagram, there is a specific target voltage for every mass flow rate for which the current rises sharply. This voltage is named *transition* voltage. Mode transition for 80 W RF power and 2 sccm mass flow rate condition is shown in Figure 1.8 [12].

Experimental results for various RF input power and mass flow rates at 40 V
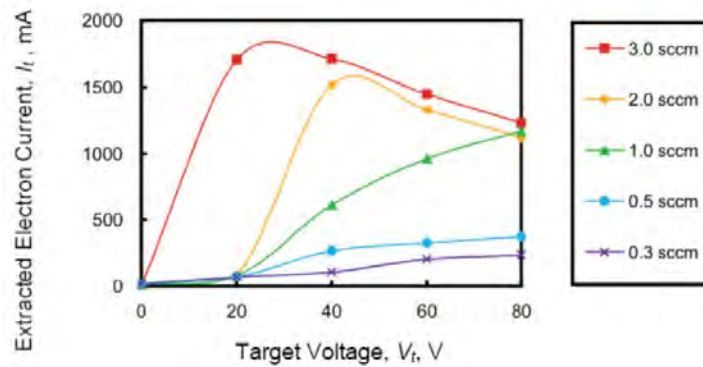
Figure 1.7. Current-voltage characteristics of RF plasma cathode at 80 W of RF input power [12].
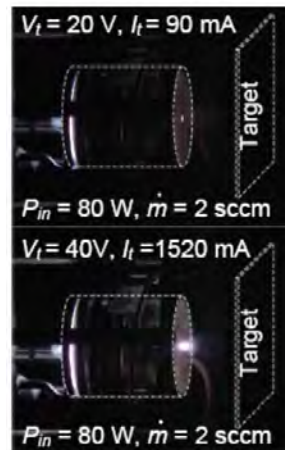
Figure 1.8. Transition mode for 80 W RF power and 2 sccm mass flow rate condition [12].

target voltage are shown in Figure 1.9. It can be seen from the diagram that at sufficient mass flow rates, extracted electron current is roughly proportional to the RF input power. In the low mass flow rates, extracted current does not change considerably by increasing the RF power. The problem is that there is a maximum for electron extraction for a specific mass flow rate, and in low mass flow rate, the amount of extracted electron reaches the maximum amount by small RF powers. So, there is no change in the extracted current by increasing the RF power [12].

In this study, the group reported that they have extracted 1.7 A of electron current with a flow rate of 3 sccm, 80 W of RF power input at 13.56 MHz and 20 V of
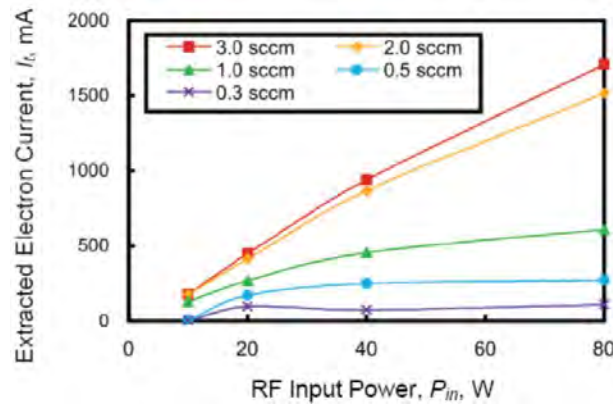
Figure 1.9. Extracted electron current as a functions of RF power and mass flow rate at 40 V target voltage [12].

target voltage.

In 2009, this group performed a study about evaluating the performance of RF plasma cathode. They used two designs and three configurations in their study. Details of these two designs are shown in Table 1.3. The three configurations are: i) Design 1 working in diode configuration (RF plasma cathode plus a target plate, ii) Design 1 as the main cathode of a DC ion thruster, iii) Design 2 as the neutralizer of an RF ion thruster [17].

Table 1.3. Cathode designs details used in the 2009 study [17].

Design	1	2
Chamber Material	Pyrex	Alumina
Chamber Diameter (D)	40 mm	10 mm
Chamber Length (L)	46 mm	18 mm
Orifice Diameter (D_O)	2 mm	1 mm
Total Number of Coils (N_{coil})	5	10

The first configuration is just like the first study of this group. The schematic of this configuration has been shown in Figure 1.6. The results for this configuration have been discussed earlier. The second configuration is shown in Figure 1.10. In DC ion thrusters, permanent magnets are used to confine the discharge. Also, in ICP the magnetic field produced by the RF field is used to sustain the plasma. There was a fear

that these two magnetic fields will act mutually and affect the confinement of plasma discharges inside DC ion thruster and RF plasma cathode. To test this, the group has performed experiments with the second configuration [17].
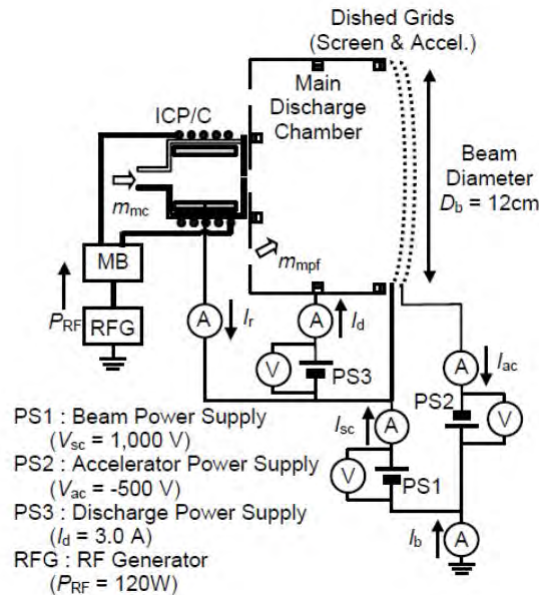
Figure 1.10. RF plasma cathode as a main cathode of a DC ion thruster [17].

The results for this configuration in comparison with the diode configuration are shown in Figure 1.11. It shows that the magnetic fields do not affect each other and RF plasma cathode can be used as the main cathode of DC ion thruster without problem. Additionally, these experiments show that the electron emission current is mostly related to the condition outside the cathode. So, in the main cathode configuration, the emitted electron current is considerably higher in comparison with the diode configuration [17].

The third configuration is shown in Figure 1.12. The main motivation for doing the experiments with this configuration was the concern about RF ion thruster and RF plasma cathode working together, because they may affect each other negatively [17].

The experiments showed that the RF ion thruster and RF plasma cathode can work together. Figure 1.13 shows the current loop for this configuration. RF ion engine
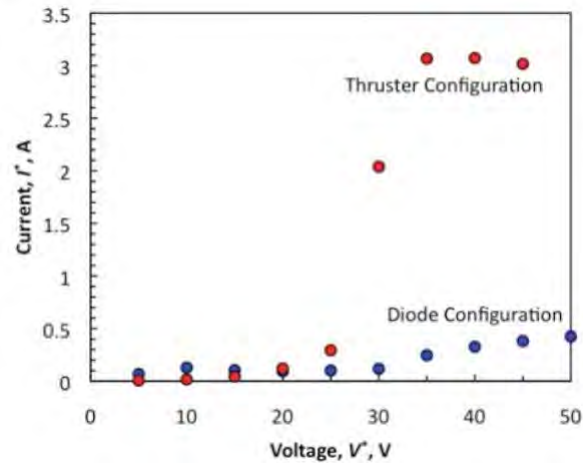
Figure 1.11. Comparison of emitted electron current with diode configuration and thruster configuration for design 1 (for 120 W of RF power and 0.8 sccm mass flow rate) [17].

reaches thrust force of 1.6 mN, specific impulse of 1500 s and thrust to power ratio of 18.9 mN/kW [17].

Through this study, the group concluded that the performance of this configuration and generally RF plasma cathode is not appropriate for practical use for small satellite missions and a parametric study should be done to improve the performance of cathode and thruster [17].
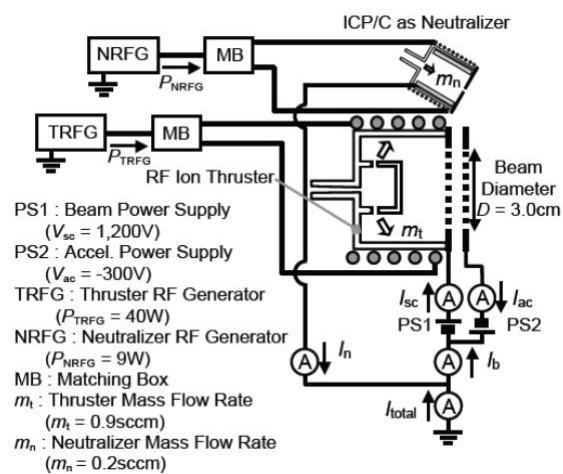
Figure 1.12. Configuration of RF ion thruster with RF plasma cathode as neutralizer [17].
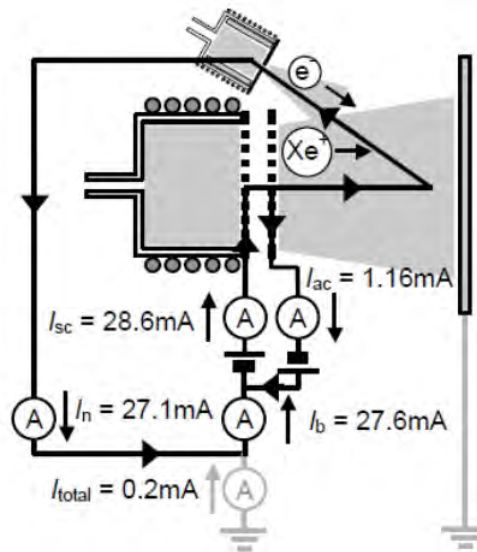
Figure 1.13. urrent loop for RF ion thruster and RF plasma cathode configuration (P_t = 40 W, P_n = 9 W, m_t= 0.9 sccm, m_n = 0.2 sccm) [17].

The second concept of RF plasma cathode, designed by American researchers (at Princeton Plasma Physics Laboratory), is shown in Figure 1.14. Discharge chamber is made of stainless steel. It has two openings, one on the top (gas inlet) and the other on the bottom (extracting tube). RF antenna is cylindrical and it is placed inside the discharge chamber, but encapsulated in a glass shell. The starting filament (ignition electrode) and Langmuir probes are placed at the top of the chamber. The sizes of components of this RF plasma cathode device are shown in Table 1.4 [13].

In this configuration, positively biased electrode is an NW-16 elbow connector that is insulated from the extracting tube. Xenon gas enters the chamber via a gas inlet, and plasma is ignited by a starting filament. The RF power (at 2 MHz) is applied to the gas inside the chamber from RF antenna. Electrons are extracted to the elbow connector that is biased positively. The other end of the elbow connector is connected to a vacuum chamber, where a probe is placed to measure the downstream gas pressure, as an indicator of chamber pressure and mass flow rate. The pressure inside the chamber is estimated to be an order of magnitude greater than the measured pressure [13] .

Table 1.4. Size of components of PPPL RF plasma cathode [13].

Item	Size
Chamber Diameter	75 mm
Chamber Length	100 mm
Glass Shell Diameter	25 mm
Extraction Tube Diameter	15 mm
Extraction Tube Length	38 mm
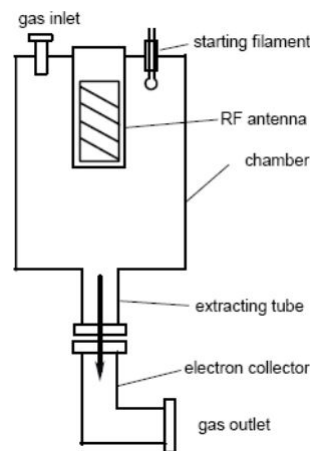
Figure 1.14. Schematic of the PPPL RF plasma cathode [13].

The extracted electron current to the elbow as a function of target voltage is shown in Figure 1.15. As can be seen in this figure, electron extraction starts at 10 V and reaches its maximum value at 30 V [13].

Extracted electron current as a function of RF power at the downstream gas pressure of 0.5 mTorr and the extracting voltage of 30 V is shown in Figure 1.16. The extracted current is nearly proportional to the RF power. It can be seen that there is a maximum extractable current for a specific mass flow rate in this experiment too (as the first configuration). At P = 0.5 mTorr, in the power range between 20 and 200 W, the plasma cathode efficiency is about 20 mA/W, corresponding to 50 eV per extracted electron [13].

It is known that there is an optimal consumption of gas pressure on characteristic
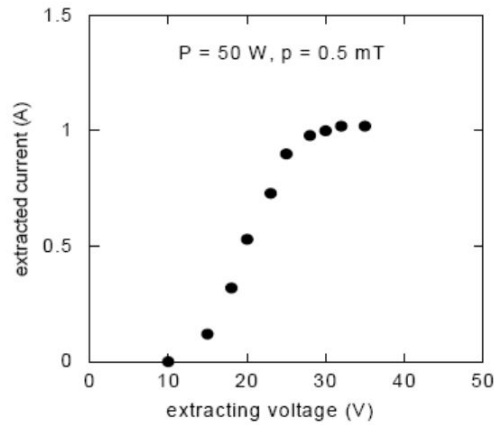
Figure 1.15. Extracted electron current versus extracting voltage [13].
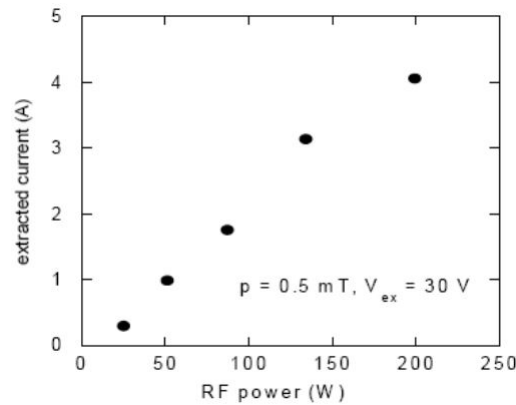
Figure 1.16. Extracted current versus RF power[13].

size of the bounded plasma that provides maximum number of ionization per discharge power. The extracted current dependence on the downstream gas pressure (Figure 1.17) indicates its optimal value around 2-3 mTorr. This value corresponds to the pressure inside the chamber around 10 mTorr. At this optimal pressure, the plasma cathode efficiency is about 25 mA/W [13].

This group performed a parametric study in 2009. A schematic of experimental setup of this study is shown in Figure 1.18. In this study, unlike the previous one, group used a 2.5 cm diameter movable electrode as the positively biased electrode [18]. The effect of electrode bias voltage and distance between positively biased electrode and RF plasma cathode on the extracted current was considered in this study. Also, total cathode efficiencies (mA/W) for different mass flow rates and RF powers are measured
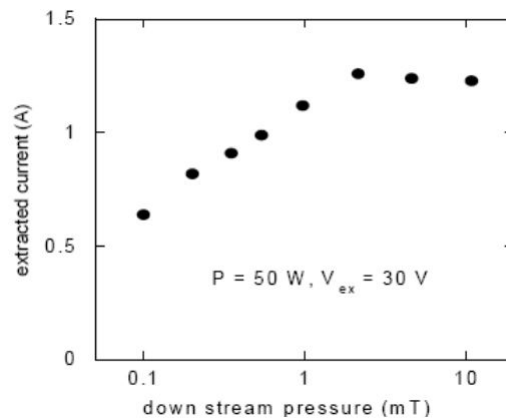
Figure 1.17. Extracted current versus downstream pressure [13].

[18].
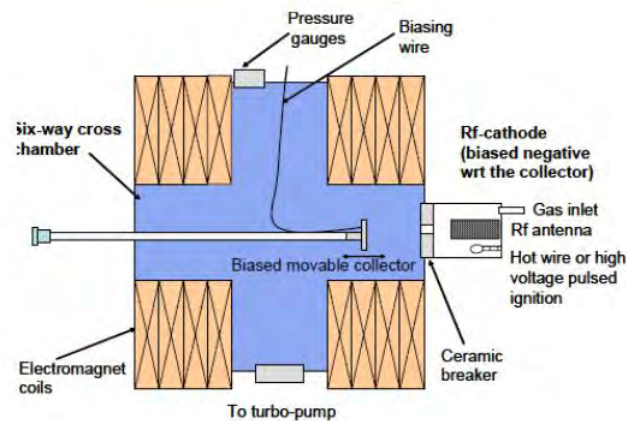
Figure 1.18. A schematic of experimental setup of the parametric study [18].

Figure 1.19 shows the effect of positively biased electrode bias voltage and its distance from the RF plasma cathode on the extracted electron current. It is obvious from this figure that electron current saturates by increasing the bias voltage. By reducing the distance between the positively biased electrode and the RF plasma cathode, the corresponding saturation bias voltage reduces too, but saturation current for all the distances is almost the same [18].

Another conclusion from Figure 1.19 is that for the same bias voltage, by increasing the distance between positively biased electrode and cathode, extracted electron current will decrease. It is because of decreasing electric potential produced by electrode on the exit orifice of the cathode by increasing its distance from it [18].

In this study, partial cathode efficiency is defined as the ratio of RF power to extracted current, and the total cathode efficiency is defined as the ratio of total power (RF and DC) to extracted current [18].
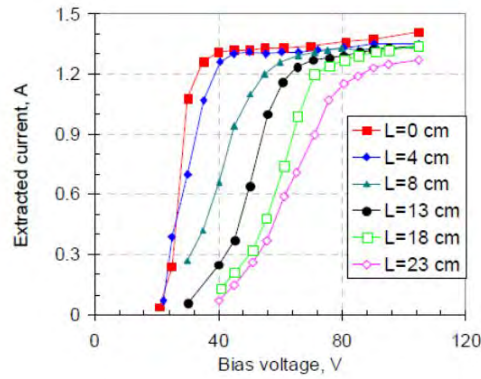
Figure 1.19. The effect of electrode bias voltage and its distance from RF plasma cathode on the extracted electron current [18].

In Figure 1.20 the total cathode efficiency for different xenon mass flow rates and RF powers are presented. It is shown that for a specified mass flow rate and RF power, by increasing the extracted electron current, total current efficiency increases, until it reaches a maximum value (saturation voltage). From this point on, the extracted current will not increase, and increasing the bias voltage would only reduce the total cathode efficiency. For larger mass flow rates and RF power, the total cathode efficiency will reach larger amounts and is more dependent on the extracted voltage. The maximum partial efficiency that they reached at this study was 30mA/W [18].
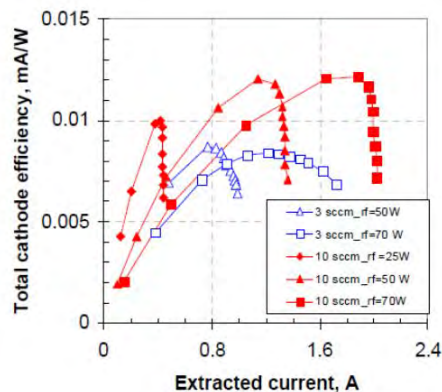
Figure 1.20. Total cathode efficiency for different xenon mass flow rates and RF powers [18].

2. THEORY OF PLASMA CATHODE DEVICES

Plasma cathodes are devices that employ a primary plasma discharge which is generated inside a chamber in order to extract electron current. Various methods have been used in the plasma generation part of these devices. The device takes its name from the method of plasma generation. After plasma is formed, an extraction setup, which consists of two electrodes (one of them grounded and the other biased positively with respect to the ground) and a DC power source, is employed in order to extract electrons from the plasma. The grounded electrode is placed inside the chamber of the device and the positively biased electrode is placed outside of it, near the orifice of the chamber. So, by applying a potential difference between these two electrodes, an electron current will flow from the grounded electrode to the positively biased electrode. A schematic of a basic plasma cathode device is shown in Figure 2.1.
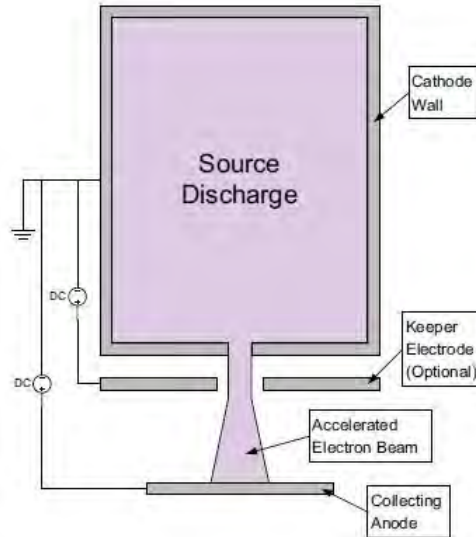
Figure 2.1. Schematic of a basic plasma cathode [3].

Electron current extraction from plasma cathode depends on both plasma generation part and electron extraction part [3]. Thus, in order to model the operation of radio frequency cathode (or any other plasma cathode device), both of these parts and also their interaction should be taken to account. So, the theory of radio frequency plasma cathode consist of two parts: first, modeling a quasineutral inductively coupled

plasma and second, modeling of plasma sheath and effects of applying a bias voltage on the plasma.

Theory of quasineutral inductively coupled plasma is developed widely and some zero-dimensional and multi-dimensional models have been introduced by numerous scientists. Each of these theories consider ICP from a specific point of view, for example, fluid model, electromagnetic model, electrodynamic model, etc. Also, plasma-wall interaction and sheath theory has been investigated and numerous models have been introduced.

In contrast, theory of electron current extraction from ICP is considered in recent years. For this reason, there are limited models that can be used in this field. Experiments [12, 19] show that applying a sufficiently high bias voltage to the source (or bulk) plasma will create a secondary structure inside the cathode which is known as anode spot or fireball. Formation of the anode spot is the most important feature of the plasma cathode device. Anode spot formation affects the current extraction considerably and should be taken into account in the modeling of plasma cathode device performance.

In this chapter, the theoretical basis of ICP plasma modeling, plasma sheath and electron extraction will be discussed.

2.1. Theory of Quasineutral (Bulk) Plasma

In order to solve the problem of inductively coupled plasma, one should employ Maxwell kinetic theory and solve Boltzmann's equation

$$\frac{\partial f}{\partial t} + \mathbf{v} \cdot \frac{\partial f}{\partial \mathbf{r}} + \frac{\mathbf{F}}{m} \cdot \frac{\partial f}{\partial \mathbf{v}} = \left(\frac{\partial f}{\partial t}\right)_c \tag{2.1}$$

where $f = f(\mathbf{r}, \mathbf{v}, t)$ is the velocity distribution function, $\mathbf{v}$ is velocity vector of a particle, $\mathbf{F}$ is external force acting on the plasma, and $\left(\frac{\partial f}{\partial t}\right)_c$ is the collision term and represents changes of velocity distribution function after collisions between two particles. But, direct solution of Boltzmann's equation is not possible. So, some assumptions have to be applied to this equation in order to simplify it [20].

In the operational condition of an RF plasma cathode, Knusden number is not very high and continuum assumption is still valid. So, we can integrate Boltzmann's equation in velocity space and obtain fluid equations for plasma. By multiplying Boltzmann's equation by n, number density, $\mathbf{v}$, velocity, and $m\mathbf{v}^2$, and integrating it over velocity space we can get continuity, momentum and energy equations for plasma. Then the continuity equation will be

$$\frac{\partial n}{\partial t} + \nabla \cdot (n\mathbf{u}) = S \tag{2.2}$$

where $\mathbf{u}$ is the mean velocity of particles, and S is the source term and is number of particles crated in per unit time per unit volume. Also, the momentum equation for plasma will be

$$\frac{\partial (n\mathbf{u})}{\partial t} + \nabla \cdot (n\mathbf{u} \otimes \mathbf{u}) = \frac{\mathbf{G}}{m} = \frac{n\mathbf{F}}{m} - \frac{\nabla \cdot \mathbf{P}}{m} + \frac{\mathbf{C}}{m} \tag{2.3}$$

In this equation $\mathbf{G}$ is total macroscopic force, $\mathbf{F} = q\left(\mathbf{E} + (\mathbf{u} \times \mathbf{B})\right)$ is the macroscopic electromagnetic force. $\mathbf{P} = m \int \mathbf{v}' \otimes \mathbf{v}' f d^3 v$ is the pressure tensor. Here $\mathbf{v}'$ is the thermal velocity of the particle, and we have $\mathbf{v} = \mathbf{u} + \mathbf{v}'$. "$\otimes$" denotes the outer product or tensor product of the two vector. $\mathbf{C}$ indicate the collision term in the momentum equation and shows the momentum loss due to collision between two species [20].

Pressure tensor can be considered as diagonal and isotropic. Also, applying ideal gas relation, we will have

$$\mathbf{P} = p\mathbf{I} = nk_B T \, \mathbf{I} = \frac{1}{3} mn\mathbf{v}'^2 \tag{2.4}$$

Second assumption can be applied to the collision term. We can consider only the collisions between charged particles and neutral particles. Also, we neglect the neutral particle velocity and consider it to be zero. In the third assumption, we assume that there is no magnetic field in the plasma. By applying these assumptions to Equation 2.3, we will have

$$\frac{\partial \mathbf{u}}{\partial t} + \mathbf{u} \left(\nabla \cdot \mathbf{u} \right) = \frac{q\mathbf{E}}{m} - \frac{k_B}{mn} \nabla \left(nT \right) - \bar{\nu}_m \mathbf{u} \tag{2.5}$$

where ν_m is the collision frequency, and $\bar{\nu}_m = \nu_m + S/n$ is the collision frequency, with taking into account the ionization. And as the last fluid equation for plasma, energy equation is obtained as

$$\frac{\partial en\varepsilon}{\partial t} + \nabla \cdot \left(en\varepsilon \mathbf{u} + \mathbf{P} \cdot \mathbf{u} + \mathbf{Q} \right) - qn\mathbf{F} \cdot \mathbf{u} = \Pi \tag{2.6}$$

Here e is Elementary charge, ε is particle total energy, including thermal and convective energy, $\mathbf{Q}$ is heat flux, and Π the net power density change in collisions and reactions. Now that we have obtained general fluid equations for all species, we can apply further assumptions specified for each species of the plasma [20].

2.1.1. Electron Transport

The continuity equation for electrons will be

$$\frac{\partial n_e}{\partial t} + \nabla \cdot \left(n_e \mathbf{u}_e \right) = S_e \tag{2.7}$$

The momentum equation for electrons of low collisional plasma can be obtained by an approximation named "drift diffusion" which neglects the inertia term and time derivative in the left hand side of Equation 2.5. So, we will have

$$n_e \mathbf{u_e} = \frac{-en_e}{m_e \bar{\nu}_m} \mathbf{E} - \frac{k_B}{m_e \bar{\nu}_m} \nabla (n_e T_e) \tag{2.8}$$

In order to simplify the energy equation, using the Maxwellian distribution, we can write the heat flux vector in terms of temperature gradient as

$$\mathbf{Q}_e = -\frac{5k_B T_e n_e}{2m_e \bar{\nu}_m} \nabla T_e \tag{2.9}$$

By neglecting convective energy of electron and considering only the thermal energy, we can obtain the mean energy of electron as

$$\varepsilon_{e,m} = \frac{3}{2} k_B T_e \tag{2.10}$$

By applying these assumptions to Equation 2.6, we will obtain electron energy equation as

$$\frac{3k_B}{2} \frac{\partial n_e T_e}{\partial t} + \nabla \cdot \left(\frac{5k_B}{2} n_e T_e \mathbf{u}_e + \mathbf{Q}_e \right) = -k_B n_e \mathbf{u}_e \cdot \mathbf{E} + \Pi_e \tag{2.11}$$

where the second term on the right had side represent the energy absorbed by electrons in one RF cycle [20].

2.1.2. Ion Transport

The continuity equation for ions is

$$\frac{\partial n_i}{\partial t} + \nabla \cdot (n_i \mathbf{u}_i) = S_i \tag{2.12}$$

In the ion momentum equation the "drift diffusion" approximation can not be applied, because inertia terms can not be neglected. So, for the ion momentum equation we will have

$$\frac{\partial \mathbf{u}_i}{\partial t} + \mathbf{u}_i \left(\nabla \cdot \mathbf{u}_i \right) = \frac{q\mathbf{E}}{m_i} - \frac{k_B}{m_i n_i} \nabla \left(n_i T_i \right) - \bar{\nu}_m \mathbf{u_i} \tag{2.13}$$

It is assumed that ion temperature is equal to neutral temperature, so an energy equation is not solved for ions [20].

2.1.3. Neutral Transport

For momentum equation of neutral particles, an approximate version of Navier-Stokes equation is solved:

$$m_n \frac{\partial \mathbf{u}_n}{\partial t} + m_n \mathbf{u}_n \left(\nabla \cdot \mathbf{u}_n \right) - m_n \eta_n \left(\nabla^2 \mathbf{u}_n + \frac{1}{3} \nabla (\nabla \cdot \mathbf{u}_n) \right) = \mathbf{F}_n - \frac{k_B}{n_n} \nabla (n_n T_n) \quad (2.14)$$

where η_n is the viscosity of the fluid and $\mathbf{F}_n$ is the viscosity force due to collisions with other species. Energy equation for neutral particles can be expressed as

$$\frac{\partial}{\partial t} \left(c_n n_n k_B T_n \right) + \nabla \cdot \left((c_n + 1) n_n \mathbf{u}_n T_n - k_B \kappa_n \nabla T_n \right) = \Pi_n \quad (2.15)$$

where c_n is heat capacity, κ_n is thermal conductivity and Π is power obtained in collisions and reactions with other species [20].

2.2. Plasma Sheath

When a solid surface is in contact with a plasma, the quasineutrality breaks down in a very thin region near the surface. This thin region is named "plasma sheath." Let's consider a floating plate that has no charge. Floating means that it is not connected to any electric potential. Also, let's consider a quasineutral DC plasma that is confined by two electrodes. When the surface is placed inside the plasma, the electron and ion currents to the surface will be [21]

$$J_e = -e\Gamma_e = -\frac{1}{4} e n_e \bar{v}_e = -e n_e \sqrt{\frac{kT_e}{2\pi m}} \quad (2.16)$$

$$J_i = e\Gamma_i = \frac{1}{4} e n_i \bar{v}_i = e n_i \sqrt{\frac{kT_i}{2\pi M}} \quad (2.17)$$

where m is electron mass and M is ion mass. We know that the electron temperature inside the plasma is much higher than the ion temperature (approximately one hundred

times) and electron mass is much lower then ion mass. Thus, the electron current to the surface will be much higher than the ion current. So, when we place the floating surface inside the plasma, it starts to collect negative charge, and so it starts to gain a negative potential. Then, this negative potential will prevent later coming electrons to reach the surface, and only the electrons with energies higher than a certain value would reach the surface. This phenomenon is shown in Figure 2.2 [21]. Actually, this negative potential will be such that electron and ion currents to the wall will be equal.
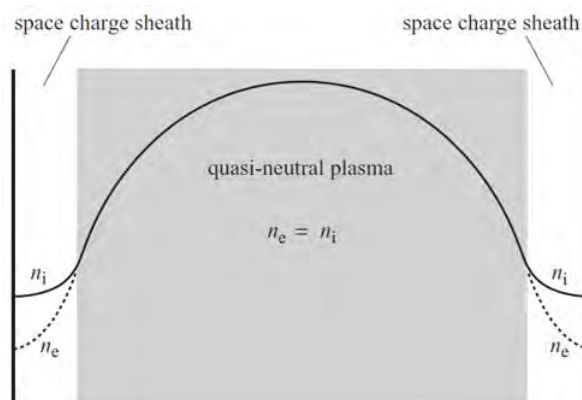
Figure 2.2. Sheath creation in a bounded plasma [21].

In order to obtain a relation between electron density and local potential inside a plasma, we consider that pressure and electric forces balance each other in Equation 2.8, and it is only in one dimension. If we put it in order, and integrate it, we will have

$$n_e(x) = n_{e0} \exp\left(\frac{e\phi(x)}{k_B T_e}\right) \tag{2.18}$$

where n_0 is the plasma density in the reference point and $\phi(x)$ is the potential difference from the reference point in a plasma. This equation is known as Boltzmann equilibrium and is an important and frequently used relation in plasma analysis.

As was mentioned above, sheath region is a region where the quasineutrality assumption breaks down. In order to find a criterion for the plasma sheath transition, we consider a condition shown in Figure 2.3. Here it is assumed that at sheath boundary $(x = s)$, $\phi = 0$, $n_{is} = n_{es} = n_s$ and ϕ', which corresponds to the electric field, is not zero, but is nearly zero $(\phi' \approx 0)$ [21].
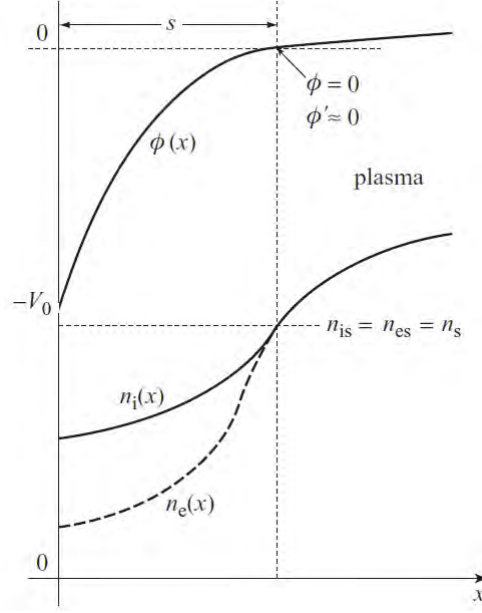
Figure 2.3. Condition of plasma-sheath transition region [21].

In isothermal condition and cold ions ($T_i = 0$), and low-pressure plasma, which means that we can neglect the collision terms, and using Boltzmann's equilibrium, we obtain an important criterion for plasma-sheath transition

$$u_B = \left(\frac{k_B T_e}{M} \right)^{1/2} \tag{2.19}$$

This equation is known as the Bohm's criterion, and u_B is Bohm's speed. This criterion says that plasma-sheath transition occurs where the ion speed becomes equal to the Bohm speed. Using this criterion and and equating Equations 2.16 and 2.17, we can find the floating potential (potential drop from plasma to a floating surface) as [21]

$$V_f = \frac{k_B T_e}{2e} \ln \left(\frac{2\pi m}{M} \right) \tag{2.20}$$

2.3. Summary of Previous Experimental and Theoretical Studies about the Electron Extraction from Plasmas

As indicated at the beginning of this chapter, the main goal of plasma cathode device is to extract electrons from the plasma that is generated inside the chamber of the device. This is achieved by applying a positive potential in front of the orifice of the plasma cathode device. The problem of extracting electrons from the orifice of the plasma cathode, and the electron extraction from bulk plasma by means of a positively biased electrode immersed inside the plasma are the same. In both of these, a positively biased surface is in contact with a plasma. For plasma cathodes, the positively biased surface is the orifice area of the device, while for bulk plasma the positively biased surface is the surface of the electrode. In this section, the previous studies about the effects and phenomena related to the immersing a positively biased electrode inside a bulk plasma are summarized.

2.3.1. Different Sheath Regimes in the Presence of a Positively Biased Electrode

In order to extract electrons from a plasma, we need to have a positively biased surface. Also, walls of the plasma chamber should be biased negatively with respect to this surface. We consider the area and potential of positively biased electrode to be A_{be} and ϕ_{be} respectively, and area and potential of walls to be A_{w} and ϕ_{w}, and plasma potential as $\phi_p(\mathbf{r})$ which depends on position. Also, we denote $I_{e,be}$ and $I_{i,be}$ as electron and ion currents going to the biased surface and $I_{e,\mathrm{w}}$ and $I_{i,\mathrm{w}}$ as electron and ion fluxes going to the walls. From current conservation law we will have [20, 22]

$$I_T = I_{e,be} + I_{e,\mathrm{w}} = I_{i,be} + I_{i,w} \tag{2.21}$$

We know that electron flux to the biased surface and the wall can be found as

$$I_{e,be} = A_{be} n_0 \frac{v_{e,th}}{4} \exp\left(-\frac{e(\phi_p - \phi_{be})}{k_B T_e}\right) \tag{2.22}$$

$$I_{e,\mathrm{w}} = A_\mathrm{w} n_0 \frac{v_{e,th}}{4} \exp\left(-\frac{e(\phi_p(\mathbf{r}) - \phi_\mathrm{w})}{k_B T_e}\right) \tag{2.23}$$

where $v_{e,th}$ is the mean thermal velocity of electron

$$v_{e,th} = \left(\frac{8k_B T}{\pi m}\right)^{1/2} \tag{2.24}$$

Also, the ion current to the biased surface and walls is using Bohm speed and Boltzmann equilibrium

$$I_{i,\mathrm{w}} = A_\mathrm{w} n_0 u_B \exp(-\frac{1}{2}) \tag{2.25}$$

$$I_{i,be} = A_{be} n_0 u_B \exp(-\frac{1}{2}) \tag{2.26}$$

By applying these equations to Equation 2.21, we will have

$$(A_\mathrm{w} + A_{be}) u_B \exp(-\frac{1}{2}) = \frac{v_{e,th}}{4}\left[A_\mathrm{w} \exp\left(-\frac{e(\phi_p - \phi_\mathrm{w})}{k_B T_e}\right) + A_{be} \exp\left(-\frac{e(\phi_p - \phi_{be})}{k_B T_e}\right)\right] \tag{2.27}$$

In order to simplify this expression, we can write

$$\mu = 4 \exp(-\frac{1}{2})\frac{u_B}{v_{e,th}} = \left(2\pi \exp(-1)\frac{m}{M}\right)^{1/2} \approx \sqrt{\frac{2.3m}{M}} \tag{2.28}$$

using this, Equation 2.27 can be rewritten as [20, 22]

$$\mu(A_\mathrm{w} + A_{be}) = A_\mathrm{w} \exp\left(-\frac{e(\phi_p - \phi_\mathrm{w})}{k_B T_e}\right) + A_{be} \exp\left(-\frac{e(\phi_p - \phi_{be})}{k_B T_e}\right) \tag{2.29}$$

Now, we begin to consider different regimes that can exist. The first regime is that biased electrode and wall collect both electrons and ions. This condition is known as ionic sheath. A schematic of potential distribution in this regime is shown in Figure 2.4. If the bias voltage becomes larger than $kT_e/2$, biased surface will collect all the

electron flux. So, Equation 2.29 becomes [20, 22]:

$$\mu(A_{\mathrm{w}} + A_{be}) = A_{be} \exp\left(-\frac{e(\phi_p - \phi_{be})}{k_B T_e}\right) \tag{2.30}$$

and hence

$$\phi_p - \phi_{be} = \frac{k_B T_e}{e} \ln\left(\frac{A_{be}}{\mu(A_{\mathrm{w}} + A_{be})}\right) \tag{2.31}$$

Thus we can see that plasma potential follows the bias potential. As mentioned, in order to consider that no ion is lost to the biased electrode, the biased voltage should be greater $k_B T_e/2$. By applying this to Equation 2.31, we will get

$$\frac{A_{be}}{A_{\mathrm{w}}} \geq \left(\frac{\exp(1/2)}{\mu} - 1\right)^{-1} \approx 1.7\mu \tag{2.32}$$
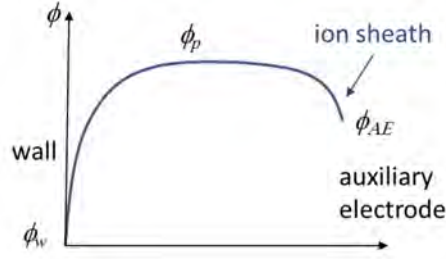
Figure 2.4. Potential distribution in ionic sheath regime [20].

The second condition is the situation that biased surface does not collect any ion and collects the electron current that corresponds the saturation current, $A_{be} n_0 v_{e,th}/4$. Actually, this corresponds to very small areas of biased surface, such as probes. When biased surface area is very small, this surface does not apply any perturbation to the plasma and the above mentioned assumptions take place. By applying these assumptions to Equation 2.29, we will have [20, 22]

$$\mu A_{\mathrm{w}} = A_{\mathrm{w}} \exp\left(-\frac{e(\phi_p - \phi_{\mathrm{w}})}{k_B T_e}\right) + A_{be} \tag{2.33}$$

By solving this we can get

$$\phi_p - \phi_w = -\frac{k_B T_e}{e} \ln\left(\mu - \frac{A_{be}}{A_w}\right) \qquad (2.34)$$

In order for this equation to be true

$$\frac{A_{be}}{A_w} < \mu \qquad (2.35)$$

A schematic of potential distribution in electron sheath condition is shown in Figure 2.5. Considering Equation 2.34, we can see that plasma potential does not follow the bias voltage and is independent of the bias voltage [20, 22].
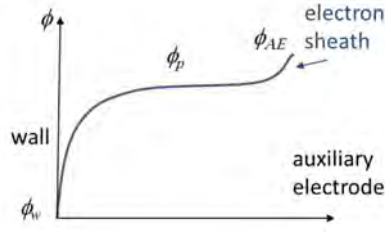
Figure 2.5. Potential distribution in electronic sheath regime [20].

The third regime is the regime between the previous ones. So we will have

$$\mu \leq \frac{A_{be}}{A_w} < 1.7\mu \qquad (2.36)$$

It is shown that a double sheath should form in this condition in order to preserve quasineutrality, and balance the ion and electron currents out of the plasma. A schematic of this condition is shown in Figure 2.6. As can be seen in this figure, double sheath is like a combination of electronic sheath and ionic sheath. A minimum potential, denoted as ϕ_D, exists near the biased surface in which $\phi_{be} > \phi_p > \phi_D$. In this regime, no electrons are lost to the walls and no ions are lost to the biased electrode. So, from Equation 2.29 we can write

$$\mu A_w = A_{be} \exp\left(-\frac{e(\phi_p - \phi_D)}{k_B T_e}\right) \qquad (2.37)$$

Recreating this equation we can get

$$\phi_p - \phi_D = \frac{k_B T_e}{e} \ln \left(\frac{\mu A_\mathrm{w}}{A_{be}} \right)$$

(2.38)

By applying the condition of Equation 2.36 to this, we can get [20, 22]

$$0 < \phi_p - \phi_D < \frac{k_B T_e}{2e}$$

(2.39)

In order to a double sheath to form in the exit orifice of a plasma cathode, two
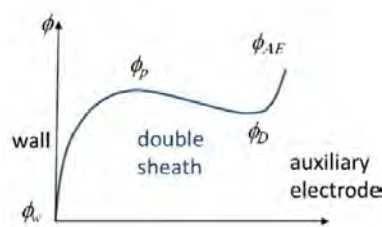
Figure 2.6. Potential distribution in double sheath regime [20].

conditions have to be satisfied:

(i) Bias voltage should be sufficiently positive ($\phi_{be} \gg T_e/e$)

(ii) The ratio of ion collecting area to the electron collecting area (exit orifice area) should satisfy Equation 2.36 [23].

2.3.2. Effect of Bias Voltage on the Bulk Plasma

It was mention in the introduction of this chapter that the plasma cathode consists of two mechanisms: a) plasma generation mechanism, b) electron extraction mechanism. The experimental investigations show that these two mechanisms do not work separately and influence each other. Electron extraction from plasma cathode does not perturb only the plasma potential. Previuos theoretical studies have proposed that applying a bias voltage and extraction of electron from plasma creates density gradients that can change the effective electron extraction area, making it larger. So, the maximum extractable current will not be the saturation electron current through the

orifice and will be much higher than that [3].

Applying a potential difference between the electrodes of plasma cathode in order to extract electrons from primarily generated plasma inside the chamber of the device, and immersing a positively biased electrode inside a bulk plasma are two types of the same problem. So, the experimental and theoretical studies regarding one of these two cases can be used for the investigation of the other. Actually, both of these cases are part of a more general problem known as double layers in plasma physics. Despite the lack of theoretical models for current extraction from a bulk plasma, numerous experimental studies [24–26] have been conducted.

As described in the previous section, plasma potential profile near a positively biased surface which works in the electron sheath regime decreases monotonically with a positive curvature to the bulk plasma potential. But, actually it is true only for low bias voltages. When a positively biased surface is exposed to a plasma, it affects the plasma properties dramatically. The applied power by a biased surface is mostly spent on accelerating electrons towards the surface and hence increasing the electron energy. High energy electrons cause more ionization near the biased surface. This leads to phenomena like anode glow and anode spot [26].

Baalrud *et al.* [26] have proposed that by increasing the bias voltage, electron energy due to acceleration towards the bias surface increases to a value that is equal to the ionization energy of the neutral particles. Ions, which are born due to this mechanism, have the same energy with thermal energy of neutral gas. The newly born ions are warded off from the biased surface and newly born electrons are attracted towards the bias surface. But, the electrons are attracted with much higher speed $(v_e = \sqrt{\frac{m_i}{m_e}} v_i)$. It leaves a region that has positive space charge near the biased surface. In this way, anode glow and double layer sheath are created. An example of an anode glow created in front of a positively biased electrode is shown in Figure 2.7 inside the red circle. As can be seen in this figure, anode glow is a thin (on the order of tens of Debye length) and shiny region near the biased surface [26].
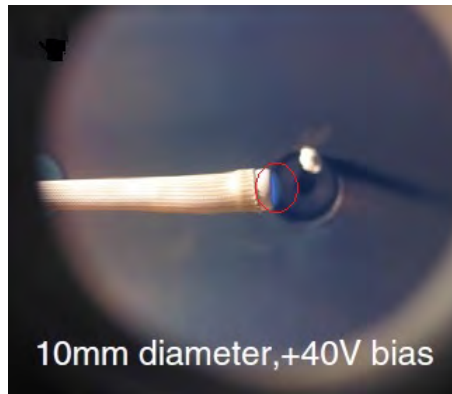
Figure 2.7. Anode glow near a positively biased surface [26].

Baalrud *et al.* [26] have proposed that by increasing the bias voltage to a greater value increases the ion density in the positive region in front of the bias surface. When the ion density and electron density inside a Debye cube near the bias surface become equal, a quasineutral plasma will be formed. In order for the ions to be lost from this quasineutral plasma to the bulk plasma, they should reach the Bohm speed. The region where the ions are accelerated to the Bohm speed should be quasineutral too and should have a potential drop near T_e/e, where T_e is the local electron temperature. In order for this to occur, the electron sheath has to expand to a length of hundreds of Debye lengths. So, when the ion density becomes equal to the electron density in the anode glow, it will be abruptly transitioned to a new structure. This large quasineutral, spherical and luminous region in front of the positively biased electrode is named "anode spot." The critical bias voltage which the rapid transitions from anode glow to anode spot happens is inversely proportional to the neutral gas pressure ($\Delta\phi \propto \frac{1}{n_g}$). The reason is that by increasing the neutral density more ionization occurs near the biased surface and quasineutrality is set at lesser bias voltages [26].

Two types of anode spots near positively biased surfaces are shown Figure 2.8. In Figure 2.8a, a spherical shaped anode spot near a 10 mm diameter biased surface is shown. In Figure 2.8b a larger biased surface with 55 mm diameter is used and a cylindrical shaped anode spot is formed near it.

Plasma potential distribution from biased surface to bulk plasma in the presence

(a) Fireball   (b) Firerod
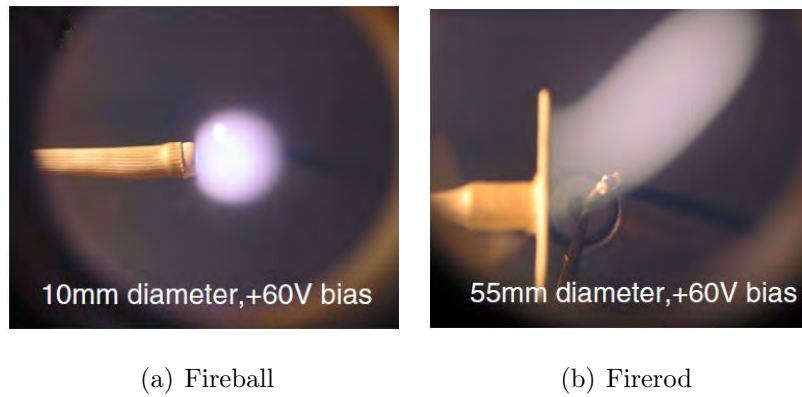
Figure 2.8. Two types of anode spot near positively biased surfaces [26].

of anode spot is shown in Figure 2.9. As expressed, with establishment of an anode spot in front of the bias surface, the double layer expands to hundreds of the Debye lengths. This length is equivalent to the ion-neutral collision length scale. The potential drop from the quasineutral region of the anode spot to the bulk plasma is equal to the electron-impact ionization energy of the neutral gas.
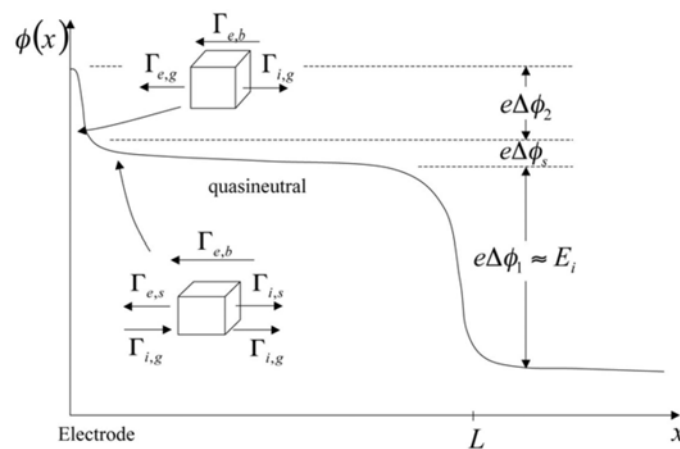
Figure 2.9. Potential distribution for anode spot [26].

Potential distribution trends between biased surface and bulk plasma for electron sheath, anode glow and anode spot regimes are shown in Figure 2.10.

Images of the generation of an anode spot in the orifice of an RF plasma cathode, obtained by laser collision-induced fluorescence (LCIF) measurements [19] are shown in Figure 2.11. This figure shows that by applying a potential difference outside the orifice of the RF plasma (and extracting electron current from it), an anode spot forms
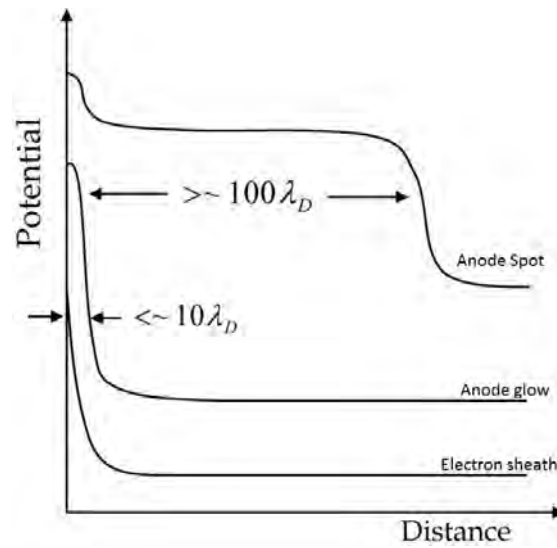
Figure 2.10. Potential distribution for different regimes of the electron sheath [26].

near the orifice of the cathode, and increasing the applied bias potential increases the size of the anode spot. This size becomes maximum when bias voltage is increased to a critical value, and from that point on increasing the bias voltage does not increase the size of the anode spot [19].
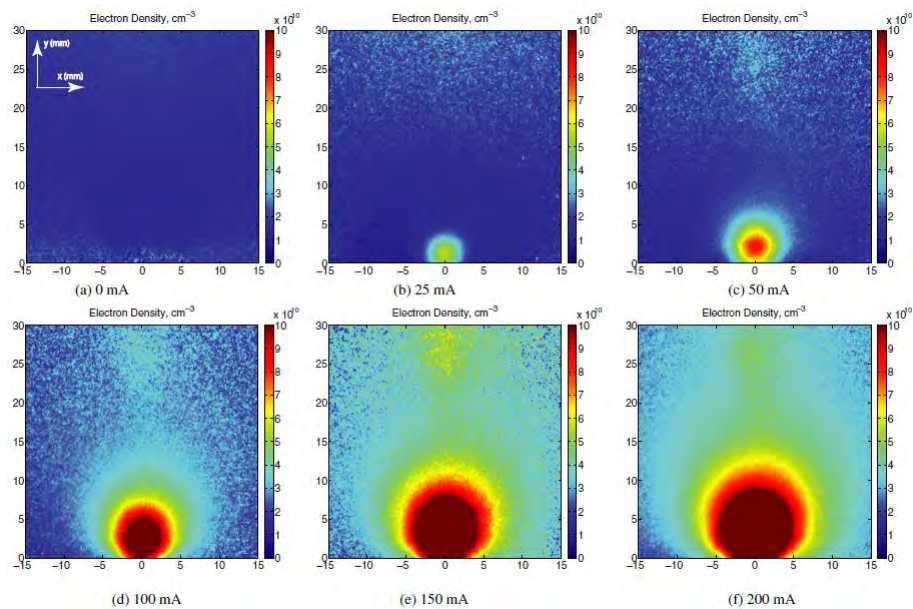
Figure 2.11. LCIF measurements, by Weatherford *et al.* [19], of the electron density for various extracted electron currents obtained by applying a positive bias to a bulk plasma.

Before establishing the anode spot, the extracted electron current by positively

bias electrode is not considerable. By establishing an anode spot near the biased surface, a jump in the extracted current occurs. The current jump has been observed in all plasma cathode studies [3, 12, 23]. Theoretical studies in the literature have proposed that when an anode spot is created in front of the biased surface (or orifice of a plasma cathode), the electron extraction area becomes the surface area of the anode spot [24]. The I-V characteristic for a positively biased surface immersed in a plasma is shown in Figure 2.12. It is obvious that before establishing the anode spot, the extracted current is very small, and establishing an anode spot causes a jump in extracted electron current. So, formation of the anode spot is thought to be the main reason for the transition of electron extraction from the low current mode the high current mode. Obviously, considering a Maxwellian energy distribution for the electrons and calculating the saturation current through the orifice area in order to obtain the extracted current will be deceiving.

When the anode spot reaches its maximum size by increasing the bias voltage, the extracted current reaches its maximum value as well, and no more current can be extracted by increasing the bias voltage further [19]. Another phenomenon that can be seen in Figure 2.12 is the hysteresis in the I-V characteristic. It means that after the anode spot is formed, by decreasing the bias voltage, the anode spot will continue to exist to much lower bias voltages than the critical bias voltage [26].
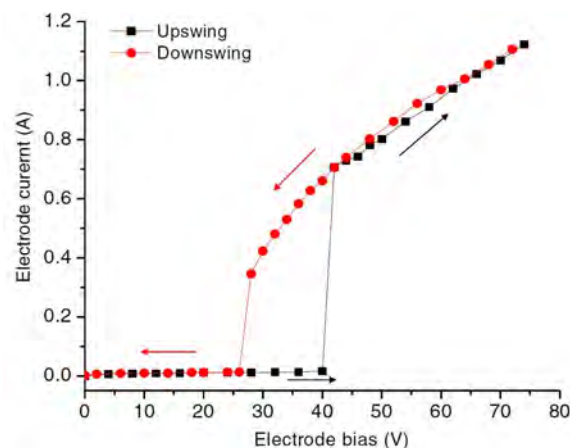
Figure 2.12. I-V characteristics for a positively biased surfaced [26].

It is important to note that by considering the maximum extractable current

from the plasma cathode as the electron saturation current (current density of $\frac{1}{4}en\bar{v}_{th}$) through the orifice for Maxwellian distribution, will give a value much smaller than the measured electron currents. Measured and calculated values for electron current from an experimental study are shown in Figure 2.13. It is obvious that calculated value is much below the extracted current, and the measured current is nearly 8 times greater than the calculated current. So, considering the Maxwellian distribution for electron energies, and orifice area as the electron extraction surface will not give correct results about the electron extraction from plasma cathode device [3]. Actually, establishing orifice plasma (anode spot) is the most important factor that affects the electron extraction from plasma cathode. So, the formation of orifice plasma must be considered in the current extraction calculation from a plasma cathode.
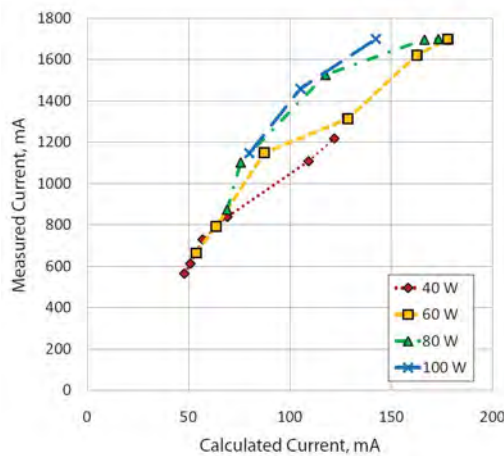
Figure 2.13. Measured and calculated values for electron current for a plasma cathode [3].

Baalrud *et al.* [26] have proposed that if the effective area for electron extraction becomes too large such that the ionization inside the bulk plasma cannot balance the extracted electron current, there should be an obstacle for electrons going to the biased surface. This can be done by establishing a double sheath or ion sheath (potential dip). In the presence of an ion sheath an anode spot cannot form because electrons are accelerated, hence there will be no extra ionization and anode spot cannot form. So, in order to decrease the electron current to obtain the global balancing of the electron and ion currents, a double sheath forms instead of an electron sheath. In the ion sheath portion of the double sheath anode spot does not exist. It attenuates the anode spot

and forms a cylindrical-shaped firerod. So, it can be said that near small bias areas, or small orifice areas in the cathode plasma, where $A_b \ll \mu$, a fireball forms. For larger bias surfaces or orifices where $A_b < \mu$, a firerod forms [26].

So, by using small orifices, the same electron current can be extracted and at the same time, less neutral particles can escape from the plasma cathode chamber the propellant gas is used more efficiently [23]. Also, a smaller orifice can raise the bulk plasma density by increasing the neutral gas pressure inside the plasma chamber and makes more electrons available to be extracted [3].

Formation of anode spot leads to considerable changes in the bulk plasma. The most important effects of the anode spot formation in the bulk plasma are:

(i) Plasma potential locking: By formation of an anode spot, the bulk plasma potential locks to the bias potential. As is shown in Figure 2.14, at the anode glow regime plasma potential is not affected much by the bias potential. But, by formation of an anode spot plasma potential jumps and locks to a the bias potential by a nearly constant value. This constant value, which is the difference between bulk plasma potential and bias voltage, is the neutral gas ionization potential plus a few Volts.
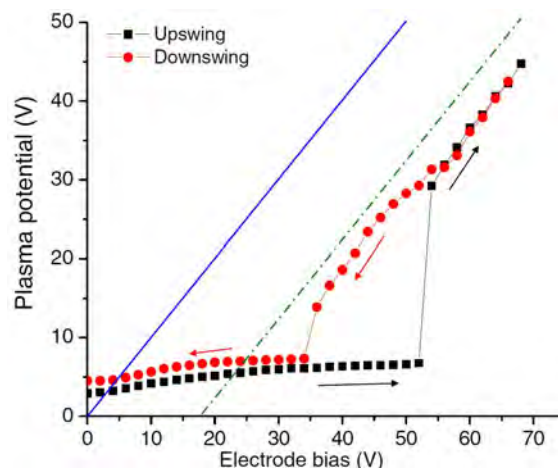
Figure 2.14. Bulk plasma potential in the anode glow and anode spot regimes [26].

(ii) Formation of an anode spot also affects the bulk plasma density and electron temperature. As shown in Figure 2.15, by applying a bias voltage and forming

an electron sheath, the electron temperature of the bulk plasma increases. Then, by the formation of an anode spot, electron temperature experiences a sudden increase and jumps to a high value [26].
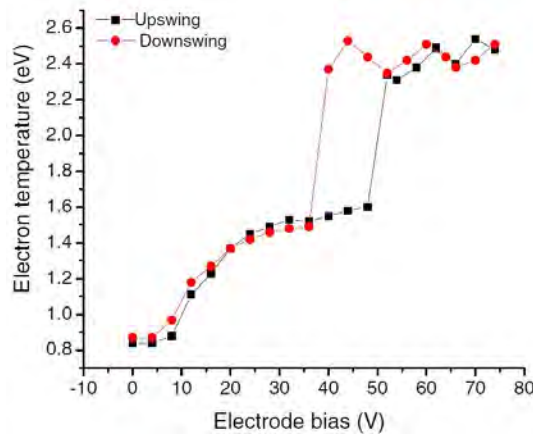
Figure 2.15. Bulk plasma electron temperature in the anode glow and anode spot regimes [26].

All of the phenomena introduced in this section in regards to the current extraction from a bulk plasma can be categorized in 4 stages:

  (i) Electron sheath regime
  (ii) Plasma breakdown and formation of anode spot
 (iii) Anode spot growth
 (iv) Anode spot size saturation and collapse

This stages are shown in Figure 2.16. The subsequent section will discuss these stages in detail.

2.3.3. Plasma Breakdown and Formation of the Anode Spot

Before formation of the anode spot, the applied bias cannot cause an electron current flow from the grounded electrode to the positively biased electrode, and in fact plasma acts as a dielectric insulator between these two electrodes. A schematic of this condition is shown in Figure 2.17.

Figure 2.16. Different regimes of plasma in the presence of an applied bias potential[27].

Starting from zero bias potential, the electron current to the biased electrode increases exponentially to a very low value. This is because of the decreasing potential barrier in the ion sheath. When the bias potential reaches the bulk plasma potential, the small current flow saturates, and increasing the bias voltage to higher values leads to the formation of an electron sheath. In the electron sheath regime, the biased voltage does not perturb the plasma potential, because the electric field cannot penetrate into the plasma and the potential between the plasma and anode is gathered in the electron sheath [28].
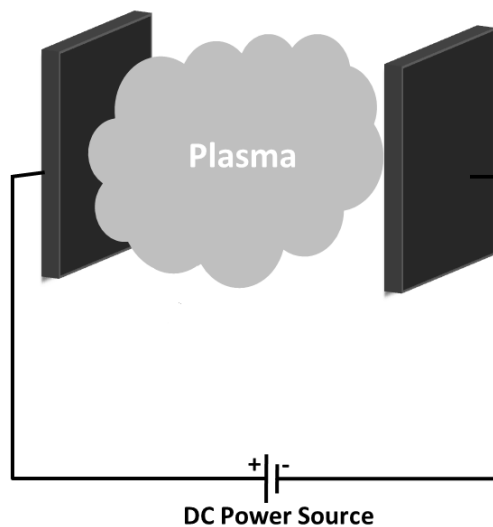
Figure 2.17. Schematic of bulk plasma and DC electrodes before formation of the anode spot.

The electron sheath regime in the presence of a biased electrode is shown in Figure 2.18. As can be seen in this figure, the electrons, that enter the electron sheath and are accelerated towards the anode, can be considered as electrons which are emitted

from a virtual cathode placed in the electron sheath edge. So, by this approach, the formation of the anode spot will be the problem of breakdown of gas between two parallel electrodes (anode and virtual cathode). The only difference is that the gap between the two electrodes does not remain constant and changes with the size of the electron sheath.
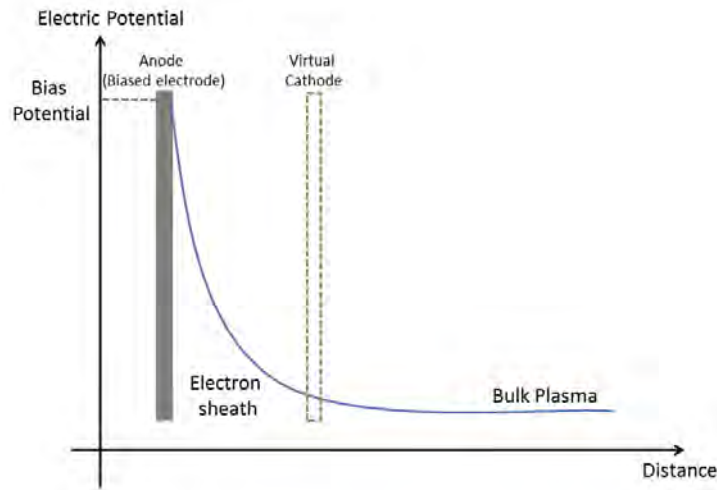
Figure 2.18. Electron sheath regime in the presence of a biased electrode.

The problem of breakdown of gas between two parallel electrodes has been considered widely in plasma physics and the most applied models for it are Paschen's law and Townsend's theory. In 1889, Paschen showed that if a sufficiently high potential is applied between the two electrodes, the gas breakdown occurs suddenly and the gas becomes a conductor. He studied this phenomenon experimentally and obtained curves for the relation between minimum voltage needed for breakdown and the pressure of the gas and the gap between two electrodes. He figured out that the minimum voltage is a function of the product of the gas pressure p and the gap between the elctrodes d [29]. The experimental results from Paschen's study are known as "Paschen's curves" and have been used widely. Figure 2.19 shows the Paschen's curves for different gases. Despite experimental results, there was no theoretical model for the gas breakdown mechanism at that time.

In 1909, Townsend proposed a model for the breakdown of the gas between two parallel plates. His theory also accounted for the minimum breakdown voltage ob-
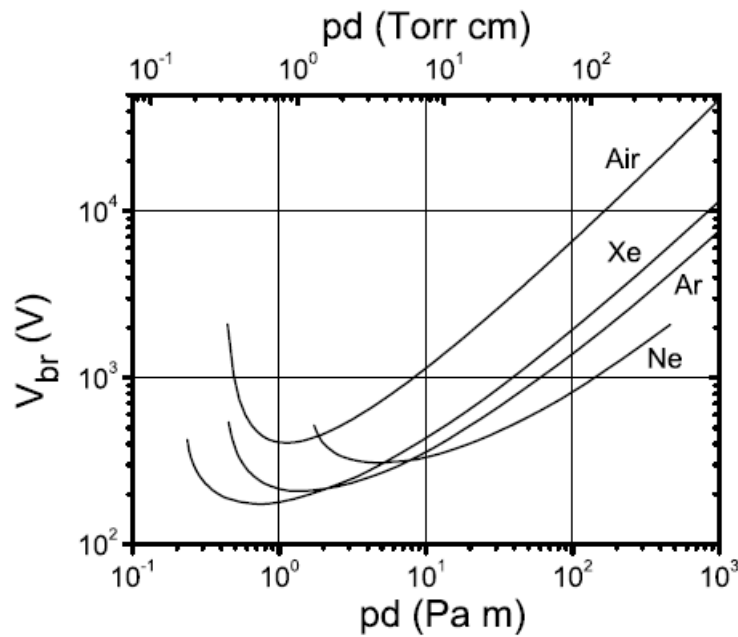
Figure 2.19. Paschen's curves for different gases [29].

served in Paschen's experiments. Townsend's theory described microscopic processes as electron impact ionization of neutral gas atoms, multiplication of charge in electron avalanches, and secondary electron emission due to ion impact in the cathode. Townsend's theory is still used as a reliable description of gas breakdown in low-pressure discharges [29]. Without going into details, a brief description of the Townsend's theory will be presented.

As it is known, charged particles have two kinds of motions: a)thermal or random b)drift or directed. In the study of the gas discharge breakdown, we are interested in the drift motion of the charged particles. Force balance for the drifted electrons is done by equating the electric field force $(-eE)$ and the rate of change of the electron momentum $(mv\nu)$, if we assume that the momentum is transferred from electrons to neutral gas when they have collision with frequency of ν. So, for this model the mean free path for the collisions (λ) must be much smaller than the dimensions of the system under study $(\lambda \ll d)$. Then the drift speed of the electrons can be found from the force balance equation as [30]

$$v_{drift} = \left(\frac{e}{m\nu}\right) E = \mu E \qquad (2.40)$$

where μ is the mobility of the electrons. Generally, mobility of the electrons is an inverse function of the gas pressure. It means that when the gas pressure increases, it becomes harder for electrons to move. Also, mobility is strongly dependent on the electron energy, but is assumed to be constant in simple models. The mobility can be related to the diffusion by the Einstein's relation $D/\mu = k_B T/e$, where D is diffusion [30].

When an electron travels a distance equal to one mean free path for ionization (λ_{iz}), this electron generates one electron-ion pair on average. So the number of new electrons that are generated in each slab dx of the gap between the two plates is [30]

$$dN = N dx/\lambda_{iz} \tag{2.41}$$

where N is the local number of the electrons. So, solving this equation we can find a relation for the increase of the electron and ion populations depending on the distance from the electrode [30]

$$N = N_0 \ \exp(x/\lambda_{iz}) \tag{2.42}$$

where N_0 is the electron population at $x = 0$ or cathode electrode. In order to obtain a relation for the ionization mean free path, Townsend used the total scattering mean free path λ and considered the ionization reaction as a process triggered by drift energy obtained from the electric field $E\lambda$ with an threshold energy of eV_{iz}. Doing this, he obtained the ionization rate constant known as Townsend's ionization coefficient[30]

$$\alpha = \frac{1}{\lambda_{iz}} = \frac{\text{constant}}{\lambda} \exp\left(\frac{-V_{iz}}{E\lambda}\right) \tag{2.43}$$

As was stated above, the mean free path is inversely related to the pressure, so

Equation 2.43 can be written as

$$\alpha = Ap \exp\left(\frac{-Bp}{E}\right) \tag{2.44}$$

where A and B are constants and are properties of the gas. After describing consequences of the electron motion, the consequences of the ion motion also should be taken into account in the model. Acceleration of the ions in the electric field towards the cathode electrode and hitting it, leads to secondary electron emission from the cathode with a rate of γ per incident ion. The processes of the ionization and electron emission will be self-sustaining when the emitted secondary electrons can exactly refill the ion particles in the gap. By considering Equations 2.41 and 2.42, we find that N_0 number of initial electrons will generate $\alpha N_0 exp(\alpha x)dx$ number of new ions in a slab dx at the point x of the gap. So, the total ion production in the whole gap will be $N_0\left(\exp(\alpha d) - 1\right)$. In order for the process to be self-sustained [30]

$$\gamma N_0(exp(\alpha d) - 1) = N_0 \tag{2.45}$$

or

$$\alpha d = \ln\left(1 + \frac{1}{\gamma}\right) \tag{2.46}$$

Combining this result and Equation 2.44 we can obtain

$$Apd \exp\left(\frac{-Bp}{E}\right) = \ln\left(1 + \frac{1}{\gamma}\right) \tag{2.47}$$

In planar geometry bias potential, $V_b = Ed$, so we can obtain the Paschen's law for minimum biased voltage needed for breakdown of the gas

$$V_{b,min} = \frac{Bpd}{\ln(Apd) - \ln[\ln(1 + \gamma^{-1})]} \tag{2.48}$$

where $V_{b,min}$ is the minimum bias voltage needed in order for the discharge to be self-

sustained (and breakdown of the gas). As can be seen in Figure 2.19, at higher pd values $V_{b,min}$ increases (high-pressure insulation condition), also at very low pd values $V_{b,min}$ goes to infinity (vacuum insulation condition) and there is a minimum for $V_{b,min}$ between these two [30].

2.3.4. Anodic Double Layers and Their Properties

It is known that anode spot is a quasineutral region attached to the anode and is separated from environment by a double layer boundary. In order to have a better understanding of the anode spot, we need to investigate double layers in more detail. Double layer is a local region which can sustain a relatively high potential drop, $\Delta\phi_{DL}$ and is surrounded by plasma. Normally, the potential drop through the double layer is higher than thermal potential of the plasma, $k_B T_e/e$. Double layers made in laboratories have been observed to have a potential drop between $10 - 10^5$ volts [31].

A schematic of variation of potential, electric field and net charge density in a double layer and surrounding plasmas is shown in Figure 2.20. As can be seen in this figure, usually the potential in double layers changes monotonically. But, there are some double layers that have some maximums and minimums in their potential distributions. The electric field inside the double layer is due to the space charges of the endpoints of the double layer. The net negative charge in the low-potential side of the double layer and the net positive charge in high potential side of it create an electric field according to the Poisson's equation. Because of different densities for charges inside the double layer, the quasineutrality condition does not hold inside it. In other words, double layer is not a quasineutral region. But, sum of the negative and positive charges inside the double layer is zero. It means that double layer region is neutral as a whole [31]. Actually, in order to match the conditions between the surrounding plasmas, it is necessary that net charge and electric field be zero at boundaries of the double layer [32]. The plasmas on the two sides of it are quasineutral (Figure 2.20c). For the potential drops ($\Delta\phi$) on the order of $10 - 10^2$ volts, and plasma densities on the order of $10^{15} - 10^{16}$ m^{-3}, double layer thickness is on the order of few millimeters, while the electron and ion collision mean free paths are much higher. So, the double layer

region can be considered collisionless. Double layers formed in laboratory experiments usually carry electric current. But carrying a current is not a necessary condition for the formation of a double layer. Instead, the dominant forces in the double layers are electrostatic and inertia forces [31].
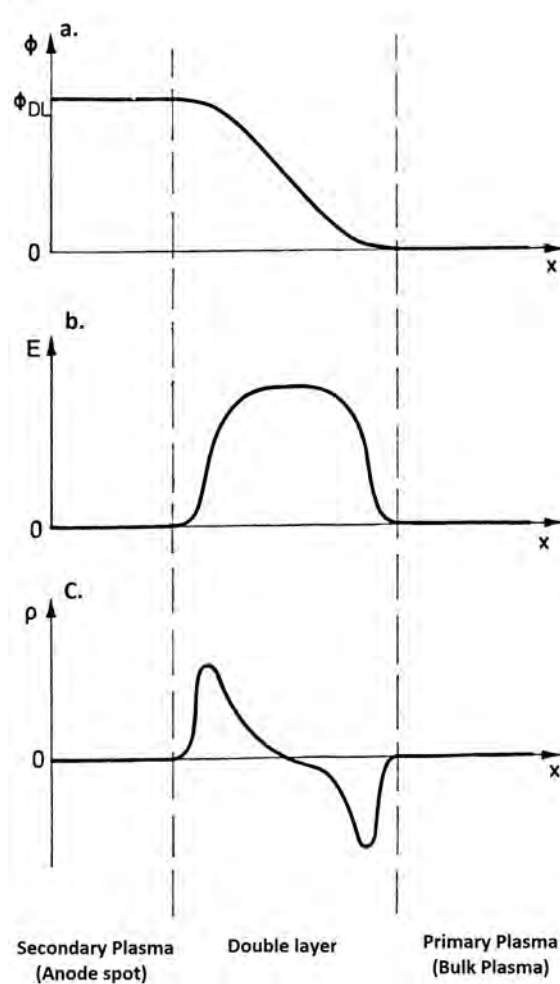
Figure 2.20. Schematic of variation of a) potential, b) electric field and c) net charge density in a double layer and surrounding plasmas [31].

Double layers are categorized depending on their different properties. For example, if the potential drop across the double layer is considered, they can be divided into two categories: strong double layer for $\Delta\phi_{DL} \gg k_B T_e/e$ and weak double layer for $\Delta\phi_{DL} \approx k_B T_e/e$. Another way to categorize the double layers is by their electric current characteristics. Double layers can be classified as current-carrying and current-free double layers by this criterion.

Some important conditions for double layers are obtained from the theoretical investigations. These conditions make the double layer stable and self-consistent. Langmuir [33] has studied strong double layers and has derived a relation between the ion current density and the electron current density inside the double layer. This relation which is based on the momentum balance in the layer is

$$\frac{j_i}{j_e} = \left(\frac{m_e}{m_i}\right)^{1/2} \tag{2.49}$$

Equation 2.49 is known as Langmuir's condition for double layers. The second important condition for double layers is the Bohm's condition. This condition was actually developed for plasma wall sheath, but it can also be applied to the high and low-potential side of the double layer. The Bohm's condition for plasma sheath is

$$u_i \geq \left(\frac{k_B T_e}{m_i}\right)^{1/2} \tag{2.50}$$

If we apply this condition to the high-potential side, we will have:

$$u_{i,as} > \left(\frac{k_B T_{e,as}}{m_i}\right)^{1/2} \tag{2.51}$$

where $u_{i,as}$ is the ion velocity at boundary of the double layer in the anode spot and $T_{e,as}$ is electron temperature in the anode spot. For low-potential side

$$u_{e,bulk} > \left(\frac{k_B T_{i,bulk}}{m_e}\right)^{1/2} \tag{2.52}$$

where $u_{e,bulk}$ the electron velocity at the boundary of the double layer in bulk plasma and $T_{i,bulk}$ is the ion temperature in the bulk plasma. Equations 2.51 and 2.52 are known as Bohm's conditions for the double layer [31].

A widely employed model for the particle populations in the presence of a double layer is shown in Figure 2.21. These particle populations can be divided into two groups: Free particles and trapped particles. Free particles are the group of particles

that can pass through the double layer and are accelerated by its electric field. So, electrons in the low-potential side and ions in the high-potential side are free particles. These particles obtain energy when they pass through the double layer and become electron and ion beams when they exit the double layer. Trapped particles are group of particles that are reflected by the double layer and cannot pass the potential barrier of the double layer. So, the ions in the low-potential side and the electrons in the high-potential side of the double layer are the trapped particles [31]. Also, some studies have suggested that special types of the double layers could be modeled by the presence of only three of these particle populations [34–36].
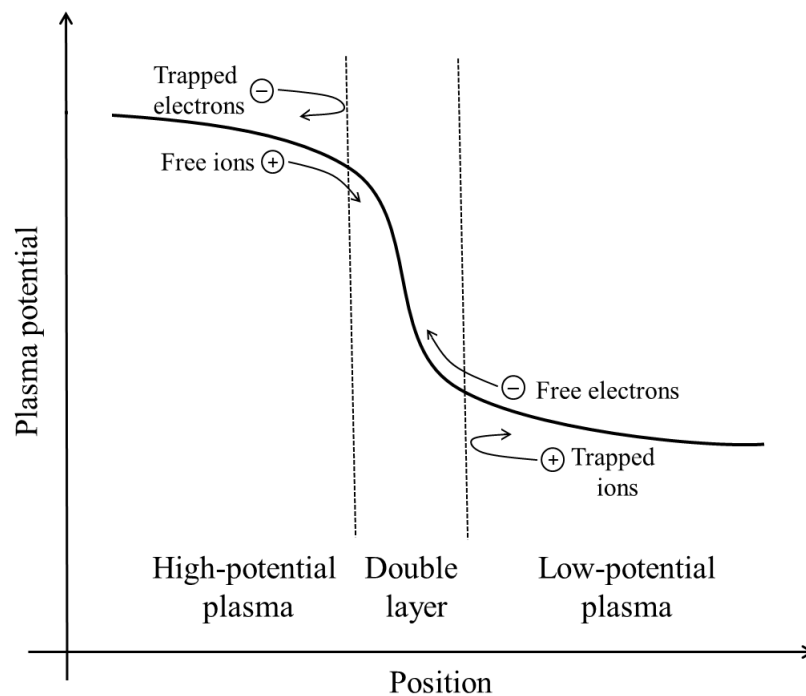
Figure 2.21. Schematic of various particles in anode spot and bulk plasma.

Experimental studies [37–40] show that by the acceleration of the free electrons in the double layer, their density reduces and becomes very low at the double layer exit. In contrast, the density of the trapped electrons, that are thermal electrons of the high-potential side plasma (which in our case is anode spot plasma), starts from zero at the position near the exit of the double layer and increases to a high value at the high-potential side plasma. Finally, the density of the trapped electrons becomes several times of the free electron density.

Figures 2.22 and 2.23 show examples of experimental results for electron densities in the double layers and high potential side plasma. Figure 2.22 is a unique measurement that indicates energy distribution function $f(\sqrt{E})$ versus energy E for various axial positions. In this figure the superimposed curve shows the plasma potential. We can see that in the low-potential side of the double layer, there is only one electron population, the free electrons that come form the low-potential plasma. By increasing the potential, this electron population moves to high energies in the energy distribution curve and becomes more energetic by acceleration in the double layer. But, its density decreases by increasing the electron drift velocity. The second electron population that can be seen in this figure, is the trapped electrons population. It starts to form at the end of double layer and its density grows to higher values inside the high potential plasma.

Figure 2.23 shows the densities for the free and trapped electrons in separate curves. Here the decay of the free electron density and the growth of the trapped electron density can be seen more clearly. At the end, the free electron density does not become zero and high potential plasma does not thermalize all of the free electrons beam [37].
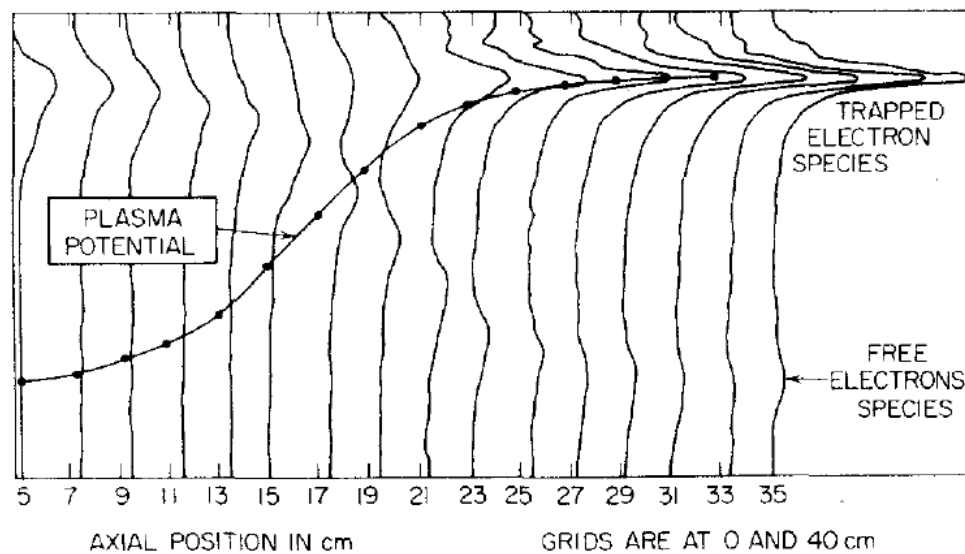
Figure 2.22. Energy distribution function $f(\sqrt{E})$ versus energy E for various axial positions. The superimposed curve shows the plasma potential [37].
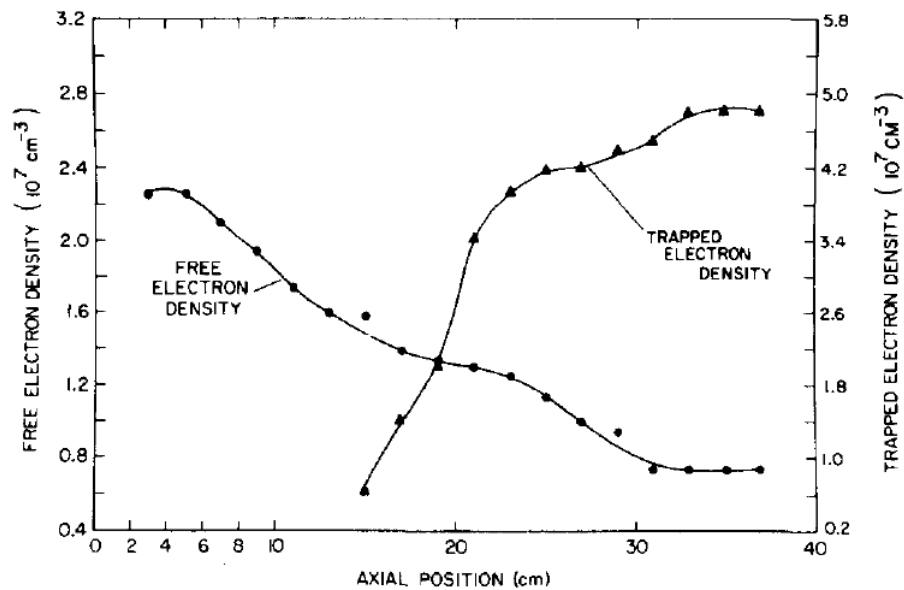
Figure 2.23. Free and trapped electron densities inside the double layer and the high-potential side plasma (corresponding to the potential profile in Figure 2.22) [37].

Figure 2.24 shows experimental results for the overall electron density (which is the sum of the trapped and free electrons). From this figure, we can conclude that the overall electron density drops inside the double layer (where only the accelerated low-density free electrons are present) and starts to increase from the point that trapped electrons are added. The LCIF measurements for electron density, shown in Figure 2.11, have some differences with the results in Figure 2.24. Figure 2.11 indicates that electron density does not drop in the double layer and also anode spot electron density is much higher than the bulk plasma electron density. Both of these results show the importance and dominance of the trapped electron population in the high-potential side. Actually, the electron beam decays rapidly in the high-potential side and causes more ionization and high electron temperature in high-potential side plasma [38]. So, the free electron density in the high-potential side can be neglected compared with the trapped electron density [31].

Experimental results for plasma potential, electron temperature and electron density for multiple anodic double layers are shown in Figure 2.25. From plasma potential diagram we can conclude that two double layers exist in this system. The low-potential region with approximately constant potential, is the bulk plasma. The second constant
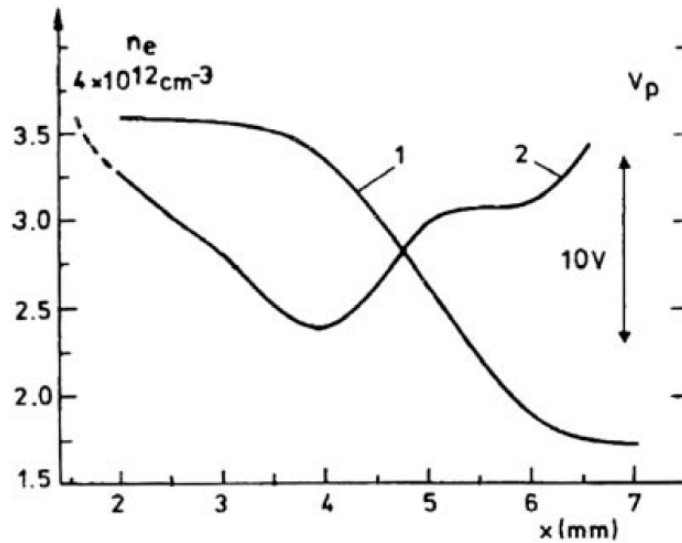
Figure 2.24. Overall electron density and electric potential for the low-potential plasma, double layer and high-potential plasma regions [41].

potential region corresponds to the high-potential side of the first double layer. The region with highest potential near the anode corresponds to the second double layer high potential plasma. Figure 2.25b shows that electron temperature increases by increasing the plasma potential. Figure 2.25c shows that electron density falls in double layer regions and increases in the plasma regions due to contribution of high volume ionization by the drifted electron beams. The electron density in the high-potential side of the double layer is much higher than the low-potential side, which is consistent with the results from LCIF measurements shown in Figure 2.11 [39].

In the next section a 0D model that is developed as a part of this thesis work, and is based on the previous theoretical studies in the literature, is presented.

2.4. 0D Model of the Plasma Cathode Device Based on the Previuos Theoretical Studies

As described in the previous section, plasma cathode device operation is considerably affected by the creation of the anode spot at the exit orifice of the device. So, any simulation method that does not account for the presence of the anode spot will
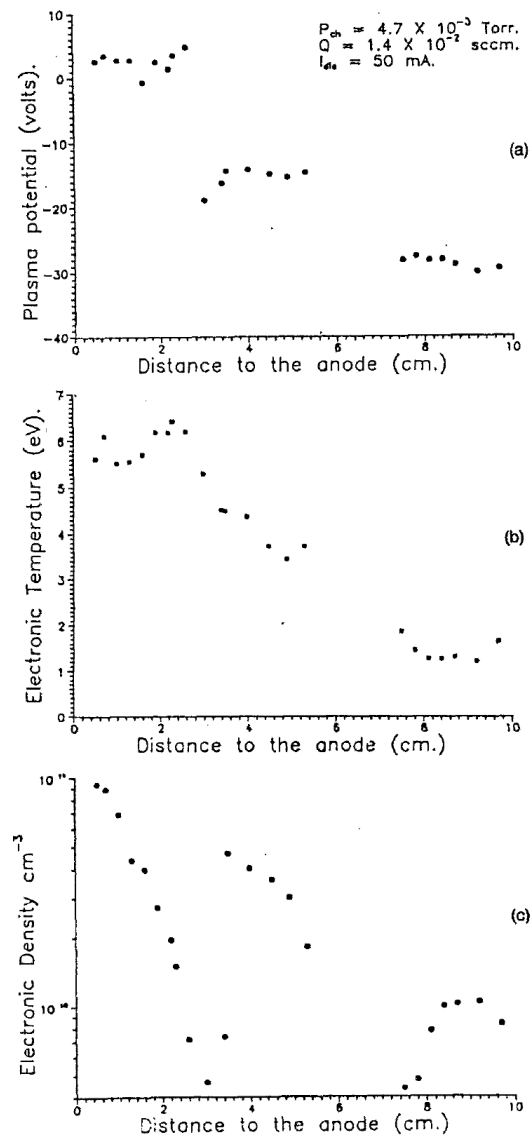
Figure 2.25. Values for a) plasma potential, b) electron temperature, and c) electron density for a multiple double layer system [39].

not give accurate results. In this section a 0D model for the operation of the plasma cathode device is introduced. This model describes the additional effects of applying a biased voltage to a bulk plasma. A schematic of the 0D model elements considered for the plasma cathode operation is shown in Figure 2.26. In this figure $n_{e,bulk}$ and $T_{e,bulk}$ represent electron density and electron temperature in bulk plasma. Also, $n_{e,as}$ and $T_{e,as}$ represent electron density and electron temperature in anode spot.
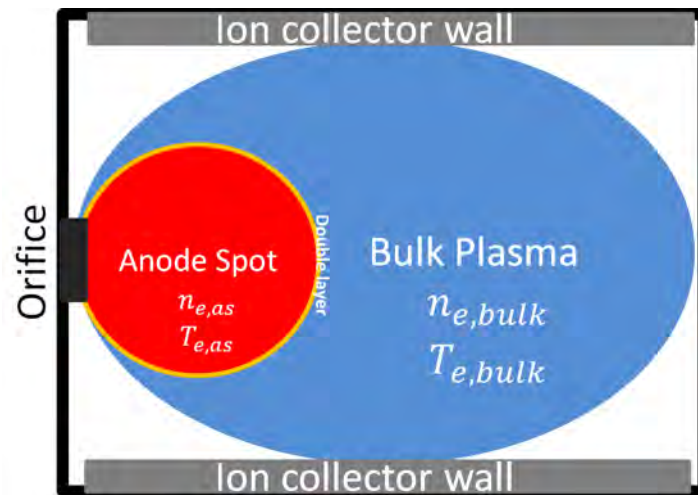
Figure 2.26. Schematic of the 0D model elements considered for the plasma cathode operation.

2.4.1. Proposed DC Circuit for the Plasma Cathode Device Operation

If we consider the basic operation and goal of plasma cathode device, we can find out that the device is a DC circuit such that its aim is to deliver DC current from one electrode (grounded electrode) to the other electrode (positively biased electrode). So, to model the operation of the device, a DC current circuit could be created. The importance of the circuit models in theoretical investigations of potential structures is known widely in cosmic plasma science [42].

As was stated in the previous section, before the formation of anode spot, the current flowing through the two electrodes is nearly zero. This behavior can be modeled by placing a capacitor in the DC circuit. It is well-known that a capacitor in DC circuit prevents any current flow in circuits and acts as an isolator in the circuit. But, when the potential difference between the two electrode of the capacitor reaches a certain value, known as breakdown voltage, the dielectric of the capacitor becomes conductor and the current can flow in the circuit. So, after the breakdown, the capacitor will be replaced by a conductor and will act as a wire in the DC circuit [43]. In the case of anode spot formation, the dielectric for the capacitor is neutral gas and the breakdown voltage is the potential difference between the bulk plasma and the biased electrode which leads to the abrupt formation of the anode spot.

When the anode spot forms (or the dielectric breakdown of the capacitor occurs) the current starts to flow between the electrodes through the bulk plasma (or current flows in the circuit). In this situation every potential difference including the double layer can be modeled as a resistor in the DC circuit. It is because double layer and other potential differences in the system act as electrical loads for the DC power source and transfer electrical energy to thermal or kinetic energy of particles [32].

Figure 2.27 shows the potential distribution for the bulk plasma and anode spot in the presence of an anode spot. $V_{p,bulk}$ shows the potential difference between grounded ion collector electrode and the bulk plasma. V_{iz} is the potential difference between bulk plasma and anode spot or the potential difference between the two sides of the double layer. $T_{e,as}$ is the anode spot electron temperature. In the presence of anode spot, the bulk plasma is locked to the bias voltage, by a value $V_{iz} + T_{e,bulk}$. So, for plasma potential we can write:

$$V_{p,bulk} = V_{bias} - (V_{iz} + T_{e,as}) \qquad (2.53)$$

Figure 2.28 shows the proposed model of the applied DC power and current circuit of
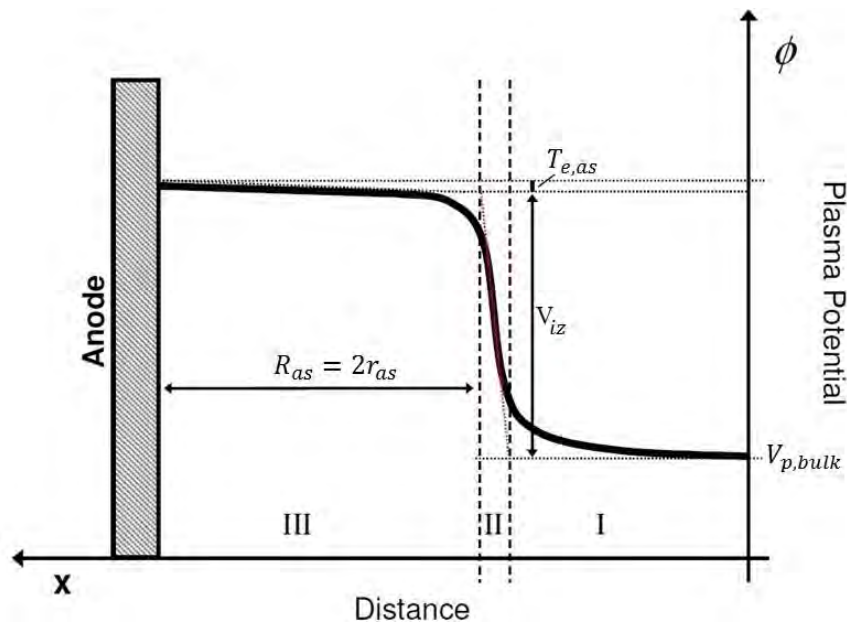
Figure 2.27. Bulk plasma and anode spot potential distribution [23].

the plasma cathode device. In this circuit, bulk plasma and anode spot are modeled as two resistors. $I_{e,extracted}$ is the extracted current from the plasma cathode. $V_{p,bulk}$ is the potential difference between grounded wall and bulk plasma, in other words, it is the bulk plasma potential. $I_{gen,bulk}$ is the electron current generated inside the bulk plasma, and is represented as a current source in the DC circuit. $I_{th,bulk}$ is the electron thermal current that is lost from the bulk plasma through the anode spot surface. Also, the ion current that is generated in the anode spot and lost to the bulk plasma is considered as an electron current from bulk plasma to the anode spot. In the anode spot, only a portion (represented by the factor of γ_{iz}) of the accelerated electrons participate in the ionization reactions inside it and the others are lost directly through the cathode orifice. The γ_{iz} factor will be derived later. The directly lost electrons, fall through a potential of $V_{iz} + T_{e,as}$. As described in the previous section, the potential drop through the double layer of anode spot (V_{iz}) is equal to the neutral gas ionization energy. The electrons that participate in the reactions inside the anode spot (which have been accelerated through a potential of V_{iz} in the double layer), will generate an electron current which is represented by $I_{gen,as}$. Finally, the extracted electron current from the plasma cathode device will be the summation of electrons that are directly lost from the bulk plasma, $(1 - \gamma_{iz})I_{th,bulk}$, and the thermal current that is lost from anode spot quasineutral plasma through the orifice of the plasma cathode, $I_{th,as}$. Using this model for the DC circuit of the plasma cathode, we can obtain

$$P_{DC,bulk} = V_{p,bulk}\ I_{e,extracted} \tag{2.54}$$

$$P_{DC,as} = \gamma_{iz}\ V_{iz}\ I_{th,bulk} + V_{iz}\ I_{gen,as} \tag{2.55}$$

2.4.2. Anode Spot Formation

Based on the model proposed in Section 2.3.3, which considers the electron sheath regime as two parallel electrodes, Park *et al.* [27] have proposed a formulation for the
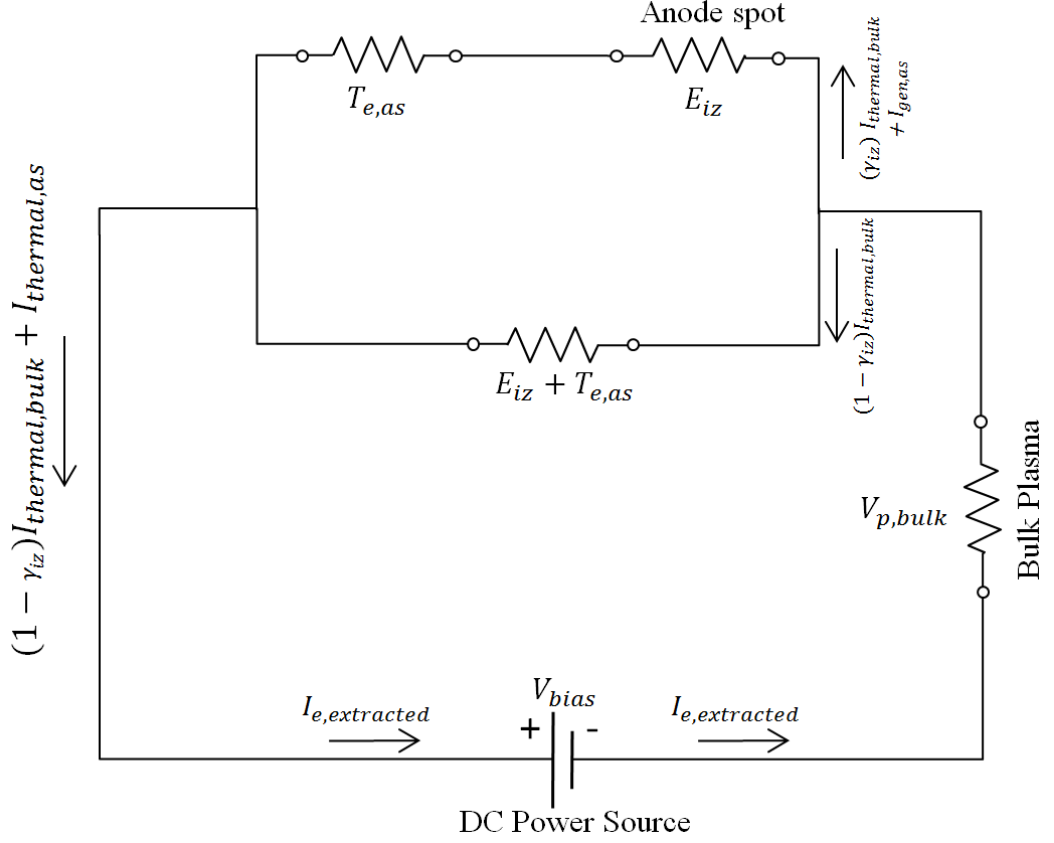
Figure 2.28. Schematic of the circuit of applied DC power.

bias voltage which leads to abrupt formation of the anode spot. First they have derived an equation for electron sheath thickness assuming collisionless sheath and $e\phi > k_B T_e$, where ϕ is the potential drop in the electron sheath. Solving electron flux equation and electron energy conservation and assuming saturation flux for electron flux at the edge of the electron sheath, Park et $al.$ have obtained for electron sheath thickness

$$s = \frac{2\sqrt{2}}{3}\pi^{1/4}\left(\frac{\varepsilon_0 T_e}{en_e}\right)^{1/2}\left(\frac{V_0}{T_e}\right)^{3/4} \tag{2.56}$$

where V_0 is the potential drop in the electron sheath. As it was described in Section 2.3.3, γ is the rate of generation of secondary electrons for incident ion current. But, in the case of electron sheath and the virtual cathode, electrons being injected from the bulk plasma to electron sheath are modeled as secondary electrons. Considering

this, we can use the Langmuir condition for plasma sheath

$$\gamma = k \left(\frac{m_i}{m_e}\right)^{1/2} \tag{2.57}$$

where k is a constant and equals to 0.387 [27]. If we consider the ion current to be negligible, $I_i \approx 0$. By combining the Paschen's law, Equation 2.48 and Equation 2.56, we can obtain a formula for the anode spot formation bias voltage

$$Ap \frac{2\sqrt{2}}{3} \frac{\pi^{1/4}}{T_e^{3/4}} \left(\frac{\varepsilon_0 T_e}{en_e}\right)^{1/2} V_b^{3/4} - \ln\left(1 + \frac{1}{\gamma}\right) \exp\left[Bp \frac{2\sqrt{2}}{3} \frac{\pi^{1/4}}{T_e^{3/4}} \left(\frac{\varepsilon_0 T_e}{en_e}\right)^{1/2} V_b^{-1/4}\right] = 0 \tag{2.58}$$

2.4.3. Particle Balance for Bulk Plasma

After the anode spot formation, it can be considered that all ions generated inside the plasma cathode are lost to the walls. It is equivalent to the assumption that no ion is lost through the orifice of the plasma cathode device. Because of the high potential difference between the bulk plasma and biased surface, this assumption seems to be appropriate. Applying this assumption, the particle balance for the bulk plasma will be:

$$n_{e,bulk} \; n_g \; K_{iz,bulk} \; \forall_{bulk} + I_{gen,as}/e = n_s \; u_B \; A_{wall} \tag{2.59}$$

where $n_{e,bulk}$ is the electron density in the bulk plasma, n_g is the neutral gas density, $K_{iz,bulk}$ is the ionization reaction rate for bulk plasma, $\forall_{bulk}$ is bulk plasma volume and $u_B = \sqrt{\frac{k_B T_{e,bulk}}{M_i}}$ is the Bohm velocity. n_s is plasma density at the sheath edge, which can be considered as $n_s = 0.5 n_{e,bulk}$ [44]. $I_{ion,as}/e$ is the value of the number of generated ions per second inside the anode spot and will be described later.

2.4.4. Power Balance for Bulk Plasma

In plasma cathode device, power is deposited to the bulk plasma by two mechanisms: RF power (or other mechanisms that the device is designed to work) and DC power. The DC power deposition in bulk plasma is presented in Equation 2.54. So, for the absorbed power for the bulk plasma we will have

$$P_{abs,bulk} = P_{DC,bulk} + P_{RF} = V_{p,bulk} \ I_{e,extracted} + P_{RF} \tag{2.60}$$

Assuming cold ions, the energy loss mechanisms from the bulk plasma are the electron current through the anode spot and collisions inside the bulk plasma. Electron flux through the bulk plasma is the electron thermal flux, $\Gamma_{th,bulk} = n_{e,bulk} \ v_{th,bulk}/4$, where $v_{th,bulk} = \left(\frac{8k_B T_{e,bulk}}{\pi m_e} \right)^{1/2}$ is the mean electron thermal velocity in the bulk plasma. So, I_{beam} can be found as:

$$I_{th,bulk} = e \ \Gamma_{th,bulk} \ A_{as} \tag{2.61}$$

where A_{as} is the anode spot surface area. In this model, the anode spot is considered as a sphere. The electrons that are ejected from the bulk plasma have an average thermal energy of $3/2k_B \ T_{e,bulk}$. So, for the energy that the electron flux through anode spot area is taking out of the bulk plasma we can write

$$P_{loss,th,bulk} = \Gamma_{th,bulk} \ E_{th,bulk} A_{as} = \frac{1}{4} \ n_{e,bulk} \ v_{th,bulk} \frac{3}{2} \ k_B \ T_{e,bulk} A_{as} \tag{2.62}$$

The second mechanism of power loss is through collisions inside the bulk plasma, which can be expressed by

$$P_{loss,coll,bulk} = n_{e,bulk} \ n_g \left[K_{iz,bulk} \ E_{iz} + K_{exc,bulk} \ E_{exc} \right] \forall_{bulk} \tag{2.63}$$

where E_{iz} and E_{exc} are ionization and excitation energy for the neutral gas and $K_{exc,bulk}$ is the excitation reaction rate for the bulk plasma.

Equating the absorbed and lost energies, we can obtain the power balance equation for the bulk plasma:

$$P_{DC,bulk} + P_{RF} = P_{loss,coll,bulk} + P_{loss,th,bulk} \qquad (2.64)$$

2.4.5. Particle Balance for Anode Spot

Because of the strong electric field inside the anode spot, all generated ions are lost to the bulk plasma. Because the anode spot is a quasineutral region, the ions that are lost to bulk plasma satisfy the Bohm criterion. So, the ion current will be

$$I_{i,as} = n_{i,as} \, u_{B,as} \, A_{as} \, e \qquad (2.65)$$

where $n_{i,as}$ is the ion density in the anode spot and $u_{B,as} = \sqrt{eT_{e,as}/M_i}$ is the Bohm speed for the anode spot plasma. The generated ions inside the anode spot have a current

$$I_{i,gen,as} = n_{e,drifted} \, n_g \, K_{iz,as} \, \forall_{as} \, e \qquad (2.66)$$

where $n_{e,drifted}$ is the drifted electron density in the anode spot which is equal to the ion density because of the quasineutrality. Equating Equations 2.65 and 2.66 we obtain

$$\forall_{as}/A_{as} = r_{as}/3 = \frac{1}{K_{iz,as} \, n_g} \sqrt{eT_{e,as}/M_i} \qquad (2.67)$$

In the anode spot, electrons are not in the equilibrium state and have a drift velocity. So, conventional reaction rates derived for Maxwellian distribution cannot be used to obtain the ionization rate for the drifted electron flux in the anode spot. Conde *et al.* [45] have derived an expression for ionization reaction rate of drifted electrons which

are fallen from a potential of V_{iz} and have thermal velocity of $v_{th,bulk}$:

$$K_{iz,as} = \sigma_o \, v_{th,bulk} V_{iz} \left[\frac{3 + 10u_o{}^2}{8u_o{}^3} \, \text{erf}(2u_o) + \frac{2 + u_o{}^2}{u_o{}^2 \sqrt{\pi}} + \frac{e^{-4u_o{}^2}}{2u_o{}^2 \sqrt{\pi}} \right] \qquad (2.68)$$

where $\sigma_o = (d\sigma/dE)_{E=E_{iz}}$ and $u_o = \sqrt{E_{iz}/(k_B T_{e,bulk})}$.

As was expressed earlier, electron flux entering from the bulk plasma to the low potential side of the double layer is $n_{e,bulk} v_{th,bulk}/4$. At the higher potential side of the double layer, where the electrons are accelerated by a potential difference of V_{iz}, the electron drift velocity is $\sqrt{2eV_{iz}/m_e}$, drifted electron flux is $\Gamma_{e,drifted} = n_{e,drifted} \sqrt{2eV_{iz}/m_e}$. Electron fluxes at low potential and high potential side of the double layer are equal, so we can write

$$n_{e,bulk} v_{th,bulk}/4 = n_{e,drifted} \sqrt{2eV_{iz}/m_e} \qquad (2.69)$$

From this equation, we can obtain

$$n_{e,drifted} = \frac{n_{e,bulk} \, v_{th,bulk}}{4\sqrt{2eV_{iz}/m_e}} \qquad (2.70)$$

In order to obtain the density of electrons that are generated inside the anode spot ($n_{e,gen,as}$), we need an extra equation. This equation can be the current conservation for the anode spot, which shows that the thermal electron current which is lost trough the orifice of the anode spot is equal to the generated electron current inside the anode spot plus the portion of drifted electron current which is thermalized in the anode spot:

$$I_{th,as} = \Gamma_{th,as} e A_{orifice} = \frac{1}{4} \, n_{e,gen,as} \, v_{th,as} e A_{orifice} = \gamma_{iz} \, I_{th,bulk} + I_{i,gen,as} \qquad (2.71)$$

2.4.6. Power Balance for Anode Spot

Power is brought to the anode spot by the electrons. Electrons that enter the anode spot has two types of energy: one is the electron thermal energy that they have obtained from the bulk plasma, calculated in Equation 2.62, and the other is the drifted energy that is modeled in Figure 2.28 and Equation 2.55 as $P_{DC,as}$. So, the absorbed energy for the anode spot is

$$P_{absorbed,as} = P_{DC,as} + \gamma_{iz} \ P_{loss,th,bulk} \tag{2.72}$$

As stated earlier, only a portion of the electrons that are ejected from the bulk plasma and drifted to the anode spot participate in the inelastic reactions inside the anode spot and are thermalized. The other electrons exit the anode spot without any reaction and energy loss. The applied DC power to the anode spot has been derived in Equation 2.55. In this equation, γ_{iz} is a coefficient that shows the fraction of drifted electrons that have participated in the reactions inside the anode spot. We know that the ionization collision frequency is $\nu_{iz,as} = K_{iz,as} \ n_g$. Also, the rate of number of electrons entering the anode spot through the double layer is $\dot{N}_{drifted} = I_{drifted}/e = I_{th,bulk}/e$. So, we can find γ_{iz} as

$$\gamma_{iz} = \frac{\nu_{iz,as}}{\dot{N}_{drifted}} = \frac{K_{iz,as} \ n_g \ e}{I_{e,drifted}} = \frac{K_{iz,as} \ n_g \ e}{I_{th,bulk}} \tag{2.73}$$

Energy loss mechanisms from the anode spot are the collisions and the energy of electrons that escape from the anode spot. The power loss via collisions can be written as

$$P_{loss,coll,as} = n_{e,drifted} \ n_g \ [K_{iz,as} \ E_{iz} + K_{exc,as} E_{exc}] \ \forall_{as} \tag{2.74}$$

where $K_{exc,as}$ is the excitation reaction rate for anode spot and is a function of $T_{e,as}$.

The energy of thermal electrons escaping through the orifice of the plasma cathode

device can be expressed as

$$P_{loss,th,as} = \Gamma_{e,th,as} \ E_{th,as} = \frac{1}{4} \ n_{e,gen,as} \ v_{th,as} \ \frac{3}{2} k_B \ T_{e,as} A_{orifice} \qquad (2.75)$$

where $A_{orifice}$ is the orifice area of the plasma cathode.

By equating the absorbed and lost energies for the anode spot, we can write the energy balance for the anode spot

$$P_{DC,as} + \gamma_{iz} P_{loss,th,bulk} = P_{loss,th,as} + P_{loss,coll,as} \qquad (2.76)$$

The aim of the 0D model proposed in this section was to capture the I-V characteristics of the plasma cathode device considering the formation of the anode spot at the orifice of the device. However, after the development of the model, it was realized that there is a problem with regards to Equation 2.67. According to the experimental studies, it was expected that by increasing the ionization rate inside the anode spot, the size of the anode spot would increase. However, according to Equation 2.67, which is obtained by the theory proposed by Baalrud *et al.* [26], by increasing the ionization rate inside the anode spot, the size of the anode spot decreases. Thus, Equation 2.67 clearly produces erroneous results. This result shows that the previous theoretical studies are not consistent with the experimental results found in the literature. Hence, a theoretical explanation of the physical system that is consistent with the experimental studies is required. In the following section, a new theoretical description of the anode spot are presented.

2.5. New Insights About the Theoretical Modeling of Anode Spot

As presented in Section 2.3, most of the previuos theoretical studies related to the anode spots [19,26,46] have neglected the electron generation inside the anode spot, and have addressed the bulk plasma as the source of the electron collected by the positively biased electrode. Such studies, also have assumed that all of the electron populations of

the anodic structures are in thermal equilibrium state, and have employed Maxwellian velocity distribution function in their theoretical investigations. On the contrary, the anodic structures such as anode spots, through which particle and energy fluxes are carried and the structure can only be sustained by the presence of these fluxes, are typical examples of non-equilibrium steady state (NESS) systems. In these types of the plasmas, the system is in steady state, and its properties do not change with time. But, the system is out of equilibrium. NESS systems can be obtained by applying external forces to a system initially in equilibrium in order to drive it out of equilibrium [47, 48]. In the case of the anode spot, the system initially in equilibrium is the bulk plasma and the driving force field is the electric field of the positively biased electrode.

Maxwellian distribution describes the systems that are stabilized to thermal equilibrium and their particles are low correlated. But, many of the plasmas observed in nature and in laboratory are not in thermal equilibrium state and cannot be described by Maxwellian distribution. One example of such plasmas could be the NESS plasmas. In order to capture the velocity distribution characteristics of these plasmas, an alternative kind of velocity distribution function has been introduced. This function is named "kappa distribution function." [49, 50] Kappa distribution function can be employed to investigate the nature of anodic structures more accurately. The NESS approach to the anode spot is especially helpful for identifying the mechanisms that sustain the anode spot and the particle populations that are dominant in the sustainment of the anodic structures. In this section a theoretical model is proposed, which suggests that the electrons generated inside the anode spot are the most important population of the system and account for most part of the extracted electron current by the positively biased electrode.

2.5.1. Particle Populations and Densities in the Presence of an Anode Spot

Formation of anode spot and double layer, results in the creation of additional particle populations in the previously unperturbed bulk plasma [24, 26]. In order to have a better understanding of the anode spot, one needs to investigate double layers in detail. A detailed review of double layer theory have been presented in Section 2.3.4.

Figure 2.29 shows a summary of the model that previous studies have proposed for the anode spot. Previous theoretical investigations, related to the anode spot phenomenon, have employed a three-particle model for the anode spot double layer, and have not included a trapped electron population in their models. As shown in Figure 2.29a, in these models the electron generation inside the anode spot is considered to be negligible. So, the only electron particles which are present inside the anode spot are the free electrons coming from the bulk plasma. Considering this, the previous studies have addressed the free electrons coming from the bulk plasma as the only population which accounts for the extracted electron current to the biased electrode [19, 24, 26, 46]. Figure 2.29b shows the way that previous studies explain the jump in the extracted current when the anode spot forms. In these studies, it is proposed that by the formation of the anode spot, the size of the area that the bulk plasma electrons extracted to the electrode changes to the surface area of the anode spot, hence a jump in the extracted electron current is observed.

An important example of such previous studies is the theoretical study done by Baalrud *et al.* [26]. In their paper, in order to obtain a relation for the anode spot size, Baalrud *et al.* have neglected the trapped electron population inside the anode spot and have equated the ion density to the free electron density inside the anode spot quasineutral plasma. From their analysis for the electron density inside the anode spot, by neglecting the trapped electron density, they have obtained [26]

$$n_{e,b} = \frac{\Gamma_{e,b}}{\sqrt{2\,e\,\Delta\phi_{DL}/m_e}} \approx n_{e,as} = n_{i,as} \tag{2.77}$$

where $n_{e,b}$, $n_{e,as}$ and $n_{i,as}$ are free (beam) electron density, total electron density and ion density in the anode spot, respectively. $\Gamma_{e,b}$ is the free electron flux at the high-potential side of the double layer, which is equal to the electron flux from the low-potential side of the double layer. $\Delta\phi_{DL}$ is the potential difference between the two sides of the double layer. The $\sqrt{..}$ term is the drift velocity of free electrons at the high-potential side of the double layer. In Equation 2.77, if one places the expression for the free electron flux at the low-potential side, which is the bulk plasma thermal saturation flux, $\Gamma_{e,b} = n_{e,p} v_{th,P}/4$, where $n_{e,p}$ is bulk plasma density, and $v_{th,p}$ is bulk plasma
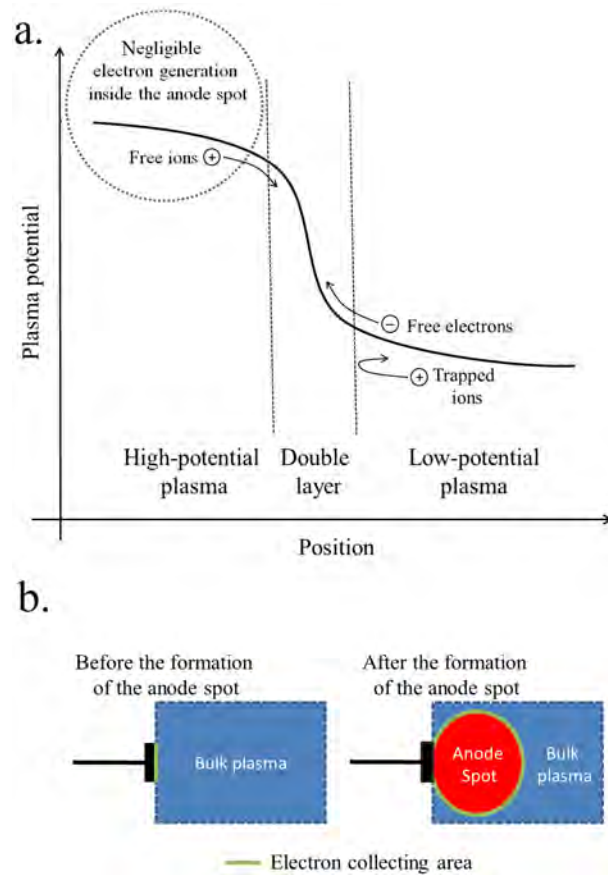
Figure 2.29. Summary of the previous theroretical models, a) Particle populations of the anode spot double layer and b) Proposed reason for the jump of the extracted electron current.

thermal velocity, one would obtain

$$\frac{n_{e,as}}{n_{e,p}} = \frac{v_{th,p}}{4\sqrt{2\,e\,\Delta\phi_{DL}/m_e}} \tag{2.78}$$

Experimental measurements done by Conde *et al.* [39] show that in the presence of anodic double layer, the free electron beam drift velocity at high-potential side is greater than two times the electron thermal velocity of the bulk plasma. So, considering Equation 2.78, Baalrud *et al.*'s formulation leads to $n_{e,p} \approx 8\,n_{e,as}$, which implies that bulk plasma electron density to be much larger than the anode spot electron density. This result could simply be depicted by examining the particle population model shown in Figure 2.29a. It is obvious that, by being accelerated inside the double layer, the density of the free electrons drops inside the anode spot. Consequently, the assumption

that the only electron population inside the anode spot is the free electrons coming from the bulk plasma, leads to the erroneous result that the electron density of the bulk plasma is higher than the electron density of the anode spot.

Contrary to this result, experimental measurements for the electron densities in the presence of an anode spot show that the anode spot is much denser than the bulk plasma [38–41]. In order to have a better understanding of the anode spot, it is useful to investigate the results of the experiments performed by Weatherford *et al.* [19], in which laser collision-induced fluorescence (LCIF) measurements are employed in order to study electron density and electron temperature in the presence of a positively biased electrode. In that study, the bulk plasma was an ICP plasma and the positive potential was applied to the bulk plasma through an orifice. The results of that study for the electron densities for various extracted electron current values (resulting from various applied bias potentials) are shown in Figure 2.11. This figure shows that the electron density inside the anode spot is nearly four or five times higher than the surrounding bulk plasma. Also, the electron density of the anode spot is approximately one order of magnitude higher than the electron density of the unperturbed bulk plasma (Figure 2.11a and 2.11f). From these measurements, it is obvious that the formation of the anode spot has a very drastic effect on the bulk plasma. This drastic effect is typical of NESS systems which affect their environments considerably [51, 52].

This contradiction between the previous theoretical studies and experimental measurements shows that the three-particle model of the anode spot double layer, shown in Figure 2.29, does not provide a true description of the anode spot. The assumption that the free electrons accelerated through the double layer are the only important electron population inside the anode spot is inconsistent with the experimental results. So, the previous theoretical studies, such as the one by Baalrud *et al.*, which have neglected the electron generation inside the anode spot, have actually omitted a potentially important mechanism that leads to the formation and the sustainment of the anode spot.

The above discussions show that anode spot double layer model should consist

of four particles. Also, the higher electron density inside the anode spot means that there is a significant electron generation inside it. The proposed model of the anode spot double layer is shown in Figure 2.30. In this model, the trapped electron are present inside the double layer. These trapped electrons mostly consist of the electrons generated inside the anode spot. Due to high electron generation, the electron density inside the anode spot is higher than the electron density of the bulk plasma. As shown in Figure 2.30b, the jump in the extracted electron current, which is observed by the formation of the anode spot, is due to the fact that anode spot is a high-density plasma, and when the anode spot forms, the electrode collects the electrons from this high-density plasma. The model proposed in Figure 2.30 is consistent with the experimental studies, and can describe the dynamics of the anode spot.
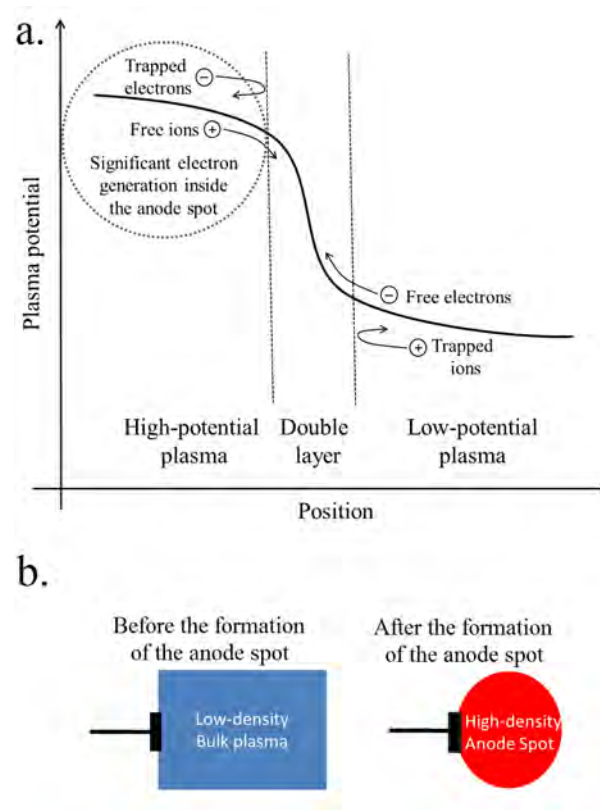
Figure 2.30. Summary of the theroretical model proposed in the present study, a) Particle populations of the anode spot double layer and b) Proposed reason for the jump of the extracted electron current.

Anode spot is an example of non-equilibrium steady state phenomena, which need an external force, and particle and energy fluxes to form and survive. By the

formation of the anode spot, the resulting system could be divided into three parts:

(i) *Anode spot*: Anode spot is a quasineutral plasma which is out of thermal equilibrium. It is actually an NESS plasma, since its properties are steady when the conditions are unchanged. Electron temperature and electron density of this plasma is much higher than the previously unperturbed bulk plasma. These values are also higher than the values corresponding to the perturbed bulk plasma. This is because of high ionization rate and higher electron generation inside the anode spot. Anode spot is sustained by electron flux entering from the bulk plasma and electron flux to the biased electrode. Electrons generated inside the anode spot constitute a potentially significant proportion of the extracted electron current to the biased electrode.

(ii) *Double layer*: Double layer acts as a boundary between the anode spot and the bulk plasma. It sustains a potential difference between these two. Only free particles are allowed to pass and trapped particles, except for the very highly-energetic ones, could not pass through the double layer. Double layer supplies the high-energy electrons needed to sustain the anode spot.

(iii) *Perturbed bulk plasma*: Perturbed bulk plasma acts as an environment for the anode spot. It is separated from the anode spot by a double layer boundary. Like the other NESS systems, the bulk plasma, as the environment, is affected by the anode spot considerably. Its electron density and electron temperature increases after the formation of the anode spot. Also, the regions of the perturbed bulk plasma, which are near the anode spot, are affected much more, and their electron temperature and density are higher than the other regions (Figure 2.11f). Perturbed bulk plasma only acts as a supplier of the high-energy electrons to the anode spot and its contribution to the electron current to the biased electrode is not considerable.

In the next section, it is shown that the non-equilibrium nature of the anode spot, in addition to the electron generation by the drifted free electrons, is one of the reason of high electron generation and high electron density inside it.

2.5.2. Kappa Distribution Function and Ionization Rates in NESS Plasmas

The proposed 0D model in Section 2.4 considers all electron population of quasineutral plasma in thermal equilibrium state and uses Maxwellian distribution function in order to describe them. But, in order to model the real system, we should consider that plasma cathode device is not in equilibrium state. To have a better understanding, it is better to describe the meaning of steady and equilibrium states from thermodynamics point of view.

Consider a system which has a definite condition with exact limitations (fixed boundary condition, concentration limitation, etc.). When a certain time passes, it will reach a steady state and its properties will be independent of time. This state is named "non-equilibrium steady state" or "steady state." Now consider a system that is isolated and does not have any limitations from the external world. After a time, this system will reach to a fixed state which no macroscopic processes occur in it. This state is a special case of steady state and is known as "equilibrium state." If there are no exact limitations, both closed and open systems can develop to their equilibrium states. When the system reaches the equilibrium state, it will not experience any macroscopic spontaneous process [53].

A non-steady, non-equilibrium state is the most general state for a thermodynamic system. In a non-steady non-equilibrium state the macroscopic state of the system experiences continuous variations with time. In non-equilibrium steady state the macroscopic system is not time dependent and its properties will not change with time, but the macroscopic processes will continue to occur. A non-equilibrium steady state is related to minimum entropy production when external forces are present in the system. In equilibrium states, the macroscopic processes cease to occur as well. So, steady state and equilibrium state are different and have distinct meanings in terms of thermodynamics. Hence, "steady state" is a special case of non-equilibrium states, and "equilibrium state" is a special case of steady states [53].

For a system in equilibrium, the velocity distribution function of particles stabi-

lizes to a Maxwellian distribution. Actually, Maxwellian distributions are developed to describe the systems that are stabilized to thermal equilibrium. But, many of plasmas observed in nature are not in equilibrium state and instead are in steady state [50]. These plasma systems cannot be described by Maxwellian distributions.

The steady plasmas out of equilibrium frequently have been observed in space where plasmas are weakly coupled, low-density and nearly collisionless. In these weakly coupled plasma systems, the interactions between individual particles are not dominant and total collective electrostatic forces of numerous particles govern the system. Strong individual interactions which can be effective in particle's motion (which is mostly dominated by its kinetic energy) are not common [50]. In order to capture the velocity distribution characteristics of these plasmas, an alternative kind of velocity distribution function has been introduced. This function is named "kappa distribution function" because of its additional parameter κ. In the case of anode spot, kappa distribution could be used to describe the trapped electron population inside the anode spot, considering that the free electron population inside the anode spot is comparatively small. This function is defined as

$$f(v) = \frac{1}{2\pi(\kappa w_0^2)^{3/2}} \frac{\Gamma(\kappa + 1)}{\Gamma(\kappa - 1/2)\,\Gamma(3/2)} \left(1 + \frac{v^2}{\kappa w_0^2}\right)^{-(\kappa+1)} \tag{2.79}$$

where $w_0 = \sqrt{(2\kappa - 3)k_B T/\kappa m}$ is the thermal velocity (or most probable speed) obtained for kappa distribution, m is the mass the of particles, T is temperature of the particles, n is the number density of the particles, v is their velocity, and $\Gamma(x)$ is the Gamma function. The κ index is a parameter that measures the system's "thermodynamic distance" from equilibrium. The physical meaning of this parameter is related to the correlation between the particles of the system [49]. Condition for this parameter is $3/2 < \kappa \le \infty$ where for $\kappa \to \infty$ the kappa distribution reduces to Maxwellian distribution (or reaches the equilibrium state) and for $\kappa \to 3/2$ the distribution reaches the endmost state from equilibrium, or "anti-equilibrium." Experimental results from space plasmas have shown that the κ index can be divided into two parts: near-equilibrium for $2.5 < \kappa \le \infty$ and far-equilibrium for $1.5 < \kappa \le 2.5$ [50]. Kappa distribution provides the best fit for the velocity distribution during space plsma experiments by

employing only 3 parameters (n, T, and κ). If a sum of two Maxwellian distributions (a bi-Maxwellian distribution) is used, it would have 4 parameters (n_1, T_1 and n_2, T_2). But, usually bi-Maxwellian distributions do not fit the experimental results as good as kappa distributions [49].

Kappa distribution was used by Vasyliunas in 1968 for the first time. He used this distribution to fit the empirical data collected by the OGO-1 satellite. Since then, it has been used widely in the field of space plasma physics. As can be seen from Equation 2.79, kappa distribution is a power law function of particle speed, in contrast with the Maxwellian distribution which is exponential function of particle speed [50]. Velocity distribution functions for different values of the kappa are shown in Figure 2.31. It can be observed that when the value of kappa approaches 3/2 (getting away from the equilibrium), the high speed (and high energy) tail of particles increases. In plasmas, this observation can be the result of various particle acceleration mechanisms such as DC parallel electric fields, field-aligned potential drops in reconnection regions, and wave-particle interaction by kinetic Alfven wave turbulence or cyclotron resonance. Actually, the mechanisms of particle acceleration and energization have been introduced as a justification for the high energy tail of the particle distribution observed in space plasmas [54]. Also, one of these mechanisms can be the potential jump of a double layer [55].
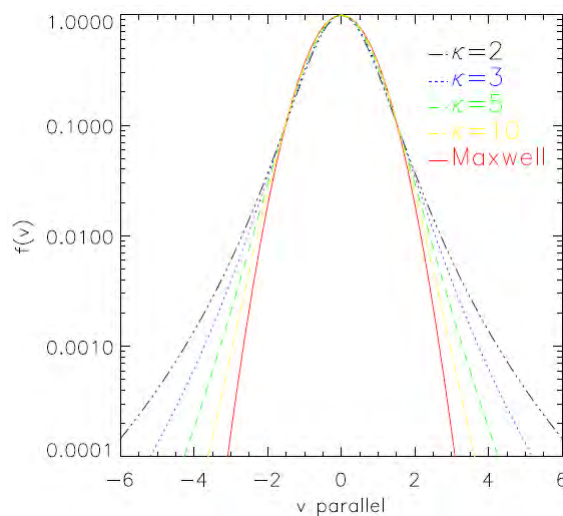
Figure 2.31. Kappa velocity distribution function for different values of kappa [49].

Using the most probable speed, a characteristic kinetic energy $E_0 = m\mathrm{w}_0^2/2$ can be obtained. This energy corresponds to the peak energy in differential flux. By using the second moment of the distribution function $U = \int d\mathbf{v} f(v) m v^2/2$ the mean energy per particle can be found as [56]

$$E_m = U/N = \frac{3}{2} E_0 \left(\frac{\kappa}{\kappa - 3/2} \right) = \frac{3}{2} k_B T \tag{2.80}$$

One of the most problematic issues for developing a distribution function for non-equilibrium systems is defining a physical meaning for the temperature out equilibrium. Traditionally, temperature of the plasmas have been calculated using the second moment of the distribution function. But, this was true for distributions that are in thermal equilibrium and it was not known that employing this method to the non-equilibrium distributions is allowed or not. In order to solve this problem it is shown that the two definitions of the temperature; i.e. kinetic and thermodynamic, are equivalent for kappa distribution function [50].

The kinetic definition of the temperature is based on the mean kinetic energy, $\langle K \rangle = \langle \frac{1}{2} m (\mathbf{u} - \mathbf{u}_b)^2 \rangle = \frac{3}{2} k_B T$ and is obtained by the second moment of the velocity distribution function. Because the mean kinetic energy gives the definition of the temperature (kinetically), it should be only a function of actual temperature and not any other parameter (such as kappa). The thermodynamic definition of the temperature is provided by relating the entropy S of the system by its internal energy U. When there is no potential energy, U is equal to mean kinetic energy $U = \langle K \rangle$. The thermodynamic temperature is defined as $T \equiv (\partial S/\partial U)^{-1} \cdot \left(1 - \frac{S}{\kappa \, k_B} \right)$. Only this relation for temperature is consistent with zero-th law of thermodynamics. Livadiotis and McComas [57] showed that the two definitions of the temperature are the same. So, they proved that the kinetic definition of the temperature for kappa distribution is consistent with the laws of thermodynamics, and obtained a well-defined temperature for the non-equilibrium steady state systems characterized by kappa distributions [50].

Equation 2.80 proves that the internal energy of the system is not dependent on the kappa index. This is consistent with the thermodynamic rules, because internal

energy is a characteristic property of the system, and can not change for various kappa value or for different steady states. So, each kappa value describes a steady state with an internal energy U which is independent of the kappa value. So, the temperature and kappa value are two independent parameters that describe a non-equilibrium steady state system [58].

Applying the kappa distribution to the plasma properties has important consequences. For example, in kappa distribution the number density will change as a power law (in Maxwellian distribution it changes exponentially). The plasma properties for kappa and Maxwellian distributions are compared in Table 2.1. In this table $R(r)$ is potential energy which includes gravitation, electrostatic and centrifugal forces. v_e is the escape velocity and A_κ is the fraction of Gamma function which is present in kappa distribution. It can be concluded that kappa distribution has higher escaping fluxes because it has more high-energy particles that can escape [49].

Table 2.1. Analytical expressions for properties of the Maxwellian and kappa distributions [49].

Parameter	Maxwellian Distribution	Kappa Distribution
Number Density	$n(r) = n_0 \exp(-\frac{R(r)}{w^2})$	$n(r) = n_0(r)\left(1 + \frac{R(r)}{\kappa w^2}\right)^{-\kappa + 1/2}$
Temperature	$T(r) = T_0$	$T(r) = T_0 \frac{\kappa}{\kappa - 3/2}\left(1 + \frac{R(r)}{\kappa w^2}\right)$
Escaping Flux	$F(r) = \frac{n_0 w(1 + v_e^2/w^2)}{2\pi^{1/2}} \exp\left(-\frac{v_e^2}{w^2}\right)$	$F(r) = \frac{n_0 A_\kappa w(1 + v_e^2/w^2)}{4(\kappa-1)\kappa^{1/2}[1 + v_e^2/(\kappa w^2)]^\kappa}$

A study has been conducted in order to investigate the effect of the applying kappa distribution in calculating the ionization rate inside a plasma. Ionization rate for a plasma is defined as

$$K_{iz} = \int_0^\infty \sigma(v_e)\, v_e\, f_e(v_e)\, dv_e \qquad (2.81)$$

where $\sigma(v_e)$ is ionization cross-section, and $f(v_e)$ is velocity distribution function [59].

This equation can be written in terms of energy $(E = \frac{1}{2}mv^2)$ as

$$K_{iz} = \int_0^\infty \sigma(E) \sqrt{\frac{2E}{m_e}} f_e(E) \, dE \tag{2.82}$$

Thomson (1912) has proposed a simple model for the evaluation of electron-impact ionization cross-section. This model considers an incident electron with velocity v which should transfer an energy E_{iz} to the valance electron which is at rest. Thompson derived an equation for the electron-impact ionization cross-section as

$$\sigma_{iz}(E) = \begin{cases} 0 & E \leq E_{iz} \\ \sigma_{iz}(E) = \pi \left(\frac{e}{4\pi\epsilon_0}\right)^2 \frac{1}{E} \left(\frac{1}{E_{iz}} - \frac{1}{E}\right) & E > E_{iz} \end{cases} \tag{2.83}$$

which is known as "Thompson cross-section." This function has a maximum value at $E = 2E_{iz}$ and and falls proportional to E^{-1} for $E \gg E_{iz}$. For electron temperatures $T_e \sim 4 \ll E_{iz}$ of Maxwellian distribution, an idealized form of ionization cross-section function can be used, because only the electron populations near the threshold energy are important and the high energy tail of the Maxwellian distribution is negligible. Considering this, the approximation of Thompson cross-section can be expressed as [59]

$$\sigma_{iz}(E) = \begin{cases} 0 & E \leq E_{iz} \\ \sigma_0 \frac{E - E_{iz}}{E_{iz}} & E > E_{iz} \end{cases} \tag{2.84}$$

where $\sigma_0 = \pi \left(\frac{e}{4\pi\epsilon_0 E_{iz}}\right)^2$. Using this formula for ionization cross-section and considering Maxwellian distribution, the ionization rate from Equation 2.82 can be found as [59]

$$K_{iz}(T_e) = \sigma_0 \, v_{th} \left(1 + \frac{2T_e}{E_{iz}}\right) \exp(-E_{iz}/T_e) \tag{2.85}$$

The formula for ionization cross section in Equation (2.84) is a linear function and is only an approximation for the exact cross section. But, this linear approximation can not be used in the calculation of kappa distribution ionization rate, because the

high energy tail is important for kappa distribution function. The experimental values, obtained by S. F. Biagi [60], for the ionization cross section for argon are shown in Figure 2.32 by solid circles. It can be seen that above a certain energy, the ionization cross section decreases for increased electron energy. But, the formula in Equation (2.84) does not account for the decrease of the cross section at high energies. Udiljak *et al.* [61] have derived a logarithmic fit for argon ionization cross section, which gives a very good match to the experimental results as seen in Figure 2.32. Formula of this logarithmic fit is expressed as

$$\sigma_{iz}(E) = 4.8 \times 10^{-20} \; \frac{\ln(E/E_{iz})}{\sqrt{E/E_{iz} + 0.1(E/E_{iz})^2}} \tag{2.86}$$
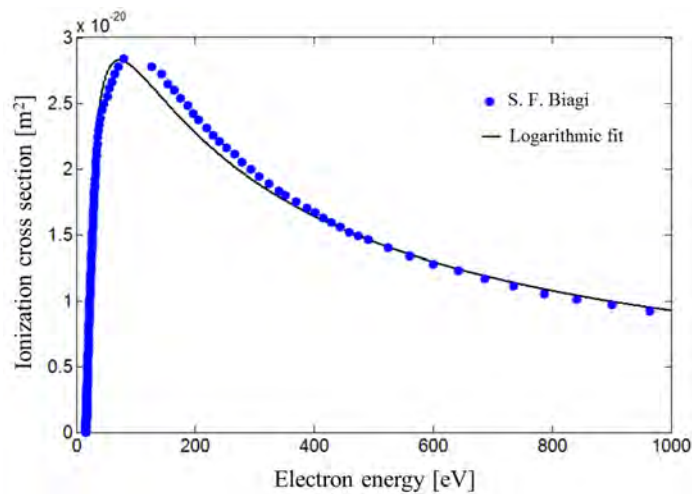
Figure 2.32. .

Experimental results obtained by S. F. Biagi [60] and logarithmic fit for ionization cross section for argon.

The electron impact ionization coefficient rates of argon for Maxwellian and NESS plasmas are calculated, using the linear approximation and logarithmic fit of the ionization cross section. The results for ionization rate of argon versus electron temperature, using the linear approximation of the cross section, are shown in Figure 2.33. The ionization rates, calculated by the logarithmic fit, are shown in Figure 2.34. Equation 2.85 is used in order to calculate the ionization of argon in Maxwellian distribution for the linear cross section. For the ionization rate of argon in kappa distribution,

Equation 2.79 and Equation 2.81 are employed, and the ionization rates are calculated numerically.

From the results of Figure 2.33 and Figure 2.34, it can be seen that employing the logarithmic cross section formula has almost no effect on the ionization rate of Maxwellian distribution. This is because of the very low fraction of the high-energy electrons in Maxwellian distribution that the higher value for ionization cross section, given by linear approximation of Equation 2.84, does not affect the ionization rate. But, for kappa distribution, for which high-energy electrons have a higher proportion, using the logarithmic formula for the ionization cross section affects the results for the ionization rate considerably. This difference is even more significant for low kappa values. But, by increasing kappa (approaching the Maxwellian distribution), the difference between the ionization rates for the two cross section formulas becomes less significant. This is the result of reduction in high-energy electrons with increasing kappa.

As can be seen in Figure 2.34, the ionization rate values for kappa distribution are significantly higher than the ionization rate values for Maxwellian distribution, for low electron temperatures. This higher ionization rate is due to the presence of more high-energy electrons in kappa distribution. But, with the increased electron temperature, the number of high energy electrons in Maxwellian distribution increases as well, and ionization rates tend to a same limit for kappa and Maxwellian distributions for electron temperatures higher than roughly 6 eV. For the kappa distribution, for electron temperatures lower than 6 eV, by decreasing the kappa value, the ionization rate increases. This suggests that as the plasma departs from equilibrium, the ionization rate increases.

Results of Figure 2.33 and Figure 2.34 show that for electron temperatures ranging from 1-3 eV, which are typical of laboratory plasmas, there is a significant difference between ionization rate of kappa distribution and of Maxwellian distribution by some orders of magnitude. This high electron generation of the trapped electrons, and the high electron generation of the drifted electrons coming from the bulk plasma, are the
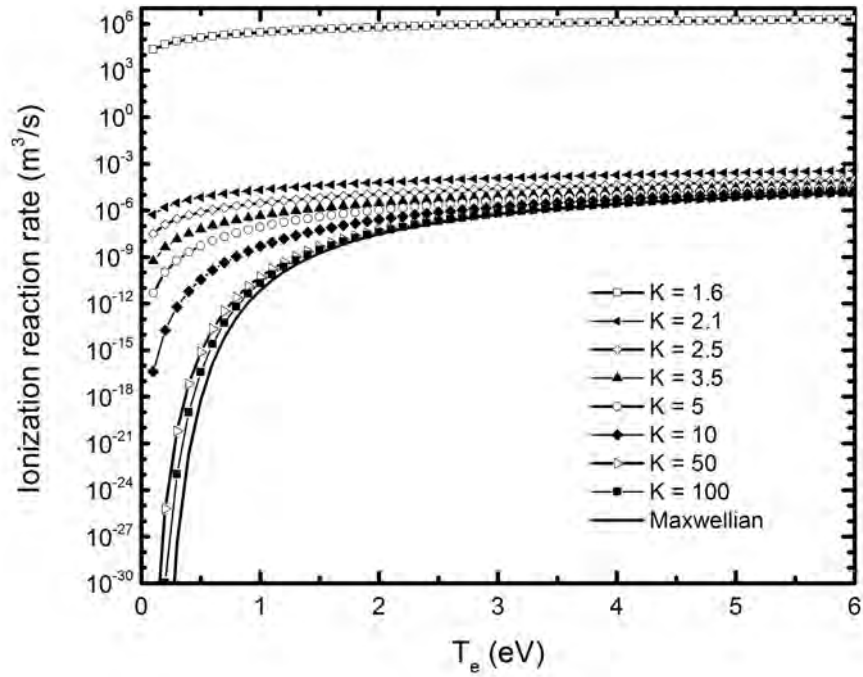
Figure 2.33. Results for the ionization rates of argon in Maxwellian distribution and kappa distribution for different values of kappa, using linear approximation of the ionization cross section.
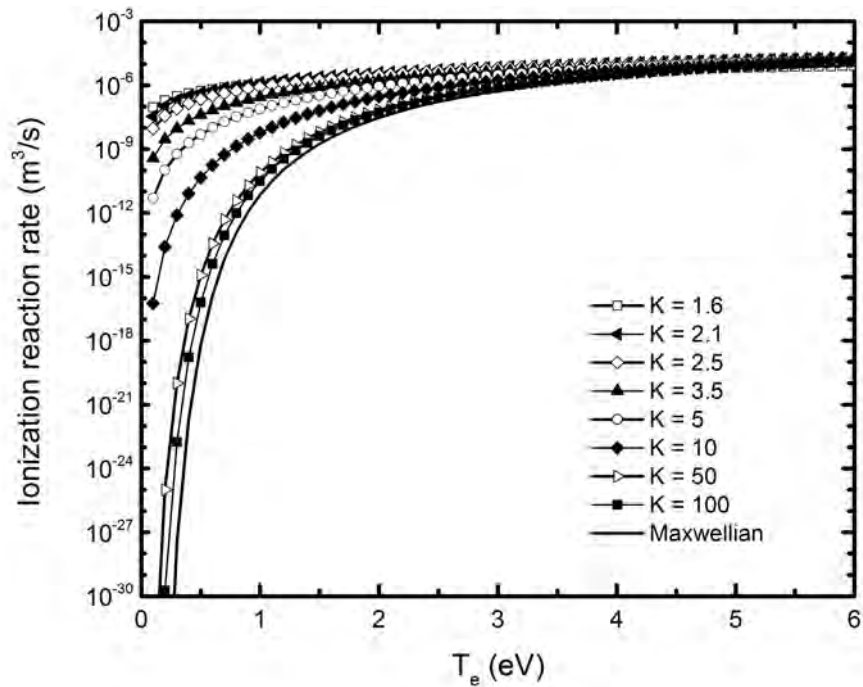
Figure 2.34. Results for the ionization rates of argon for Maxwellian distribution and kappa distribution for different values of kappa, using the logarithmic fit for the ionization cross section.

two mechanisms that make the anode spot a high-density plasma. This is in line with the previous discussions which stated that the anode spot forms due to an abrupt transition of equilibrium bulk plasma system to NESS plasma system. In the process of this abrupt transition, the electron temperature and the kappa parameter inside a certain region of the bulk plasma experience a sudden jump. So, considering the results of Figure 2.33 and Figure 2.34, this model predicts that the ionization rate of this region experiences a sudden jump as well. This would lead to a higher density plasma, the anode spot. Due to the higher ionization rates and generation of more electrons inside the anode spot, the electron current to the biased electrode would jump by the formation of the anode spot.

The value of the kappa parameter inside the anode spot, or the measure of how far is the plasma from equilibrium, depends on the electric potential applied by the electrode. After the formation of the anode spot, increasing the bias potential decreases the kappa parameter gradually, which increases the ionization rate inside the anode spot, and hence the extracted electron current increases.

3. RADIO FREQUENCY PLASMA CATHODE DESIGN AND EXPERIMENTAL SETUP

In this chapter, the design and fabrication processes of the RF plasma cathode and the materials used for its different components are presented. Also, facilities and different configurations which have been used to conduct the RF plasma cathode experiments are presented and described in detail.

3.1. Prototype RF Plasma Cathode

A prototype RF plasma cathode is manufactured in order to investigate the basic operational characteristics of the device. A 3D technical drawing and a picture of this prototype RF plasma cathode is shown in Figure 3.1. This design concept is taken from Hatakeyama *et al.*'s study [12]. The chamber of the prototype RF plasma cathode is integrated with the gas inlet and is made of pyrex. Its diameter is 4 cm. The RF coil is made of 4 mm diameter copper tube and has 5 turns. 0.5 mm thick molybdenum plate is used as the ion collector electrode inside the chamber of the RF plasma cathode. The chamber has an orifice in the center of its end surface. The diameter of this orifice is 2 mm. The gas inlet is a long pyrex tube and is also integrated with the chamber. There is a thin hole on the backside of the chamber, which allows the connection of the ion collector to the ground using a thin wire. The RF plasma cathode chamber and the RF coil are mounted on a back plate thorough the holes on the back plate. First, a fiber board (used for construction purposes) was chosen to be used as the back plate. But, because of the outgassing problem of this material, it was not possible to reduce the pressure inside the vacuum chamber. So, a teflon plate was used as the back plate, instead of fiber plate.

After some modifications on the design, number of prototype RF plasma cathodes are manufactured in order to conduct a parametric study. A picture of the experimental the setup and 2D drawing of the RF plasma cathode device used in the parametric
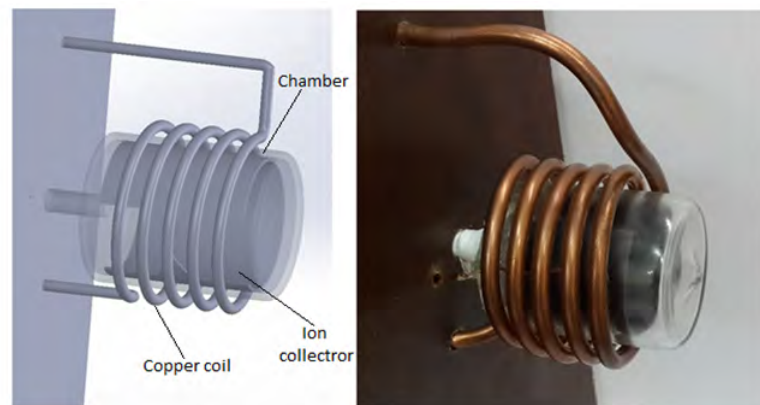
Figure 3.1. Prototype RF plasma cathode manufactured at BUSTLab.

study are shown in Figure 3.2. As can be seen in Figure 3.2, the prototype RF plasma cathodes used for the parametric study are similar to the RF plasma cathode described above, with some modifications on the installation of the cathode chamber and antenna on the back plate.
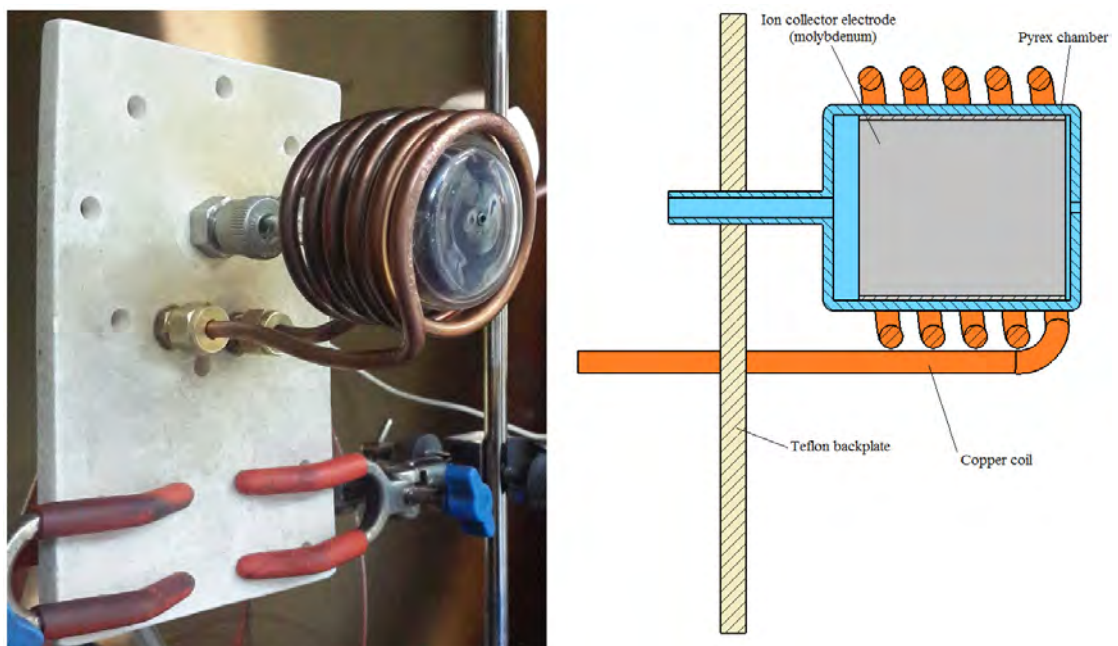
Figure 3.2. Picture of experimental setup and 2D drawing of the RF plasma cathode device used in the parametric study.

3.2. Vacuum Chamber Setup

The BUSTLab vacuum chamber, which is used during the experiments, is shown in Figure 3.3. This vacuum chamber is a 1.5 m diameter 2.7 m long tank. By using a mechanic pump and two cryogenic pumps, the pressure inside the vacuum chamber is sustained on the order of 3×10^{-5} Torr for 10 sccm argon flow rate. The mechanic pump and and its booster are used to reduce the pressure of the vacuum chamber to the order of 1 mTorr. Next, the mechanic pump is shut down and the cryogenic pumps' gates are opened to reduce the vacuum chamber pressure to 10^{-8} Torr levels. By feeding the argon gas to the device, the pressure rises to the order of 10^{-5} Torr and is sustained at that pressure.

Figure 3.3. BUSTLab vacuum chamber facility.

3.3. RF Power Source, Matching Network and RF Configuration

The RF power source and matching network devices used in the RF plasma cathode experiments are shown in Figure 3.4. RF power source is a product of T&C Power Conversion company. Its model is AG 1213W. This RF power source works at the frequency of 13.56 MHz. It can produce a maximum RF power of 1200 W. The matching network is a product of MFJ Enterprises. Its model is MFJ-989D. This device could be used for RF frequencies ranging from 1.8 to 30 MHz and Maximum RF power of 1500 W.
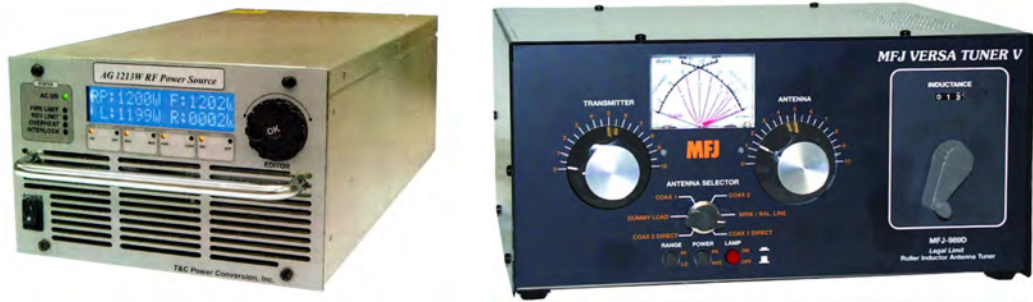
(a) RF power source　　　　　　　　　(b) Matching network

Figure 3.4. RF power source and matching network used in RF plasma cathode experiments.

MFJ-989D is a T-type matching network which manually matches the impedance of the RF coil and plasma to 50 Ω. Schematic of a T-type matching network is shown in Figure 3.5. As can be seen in this figure, a T-type matching network consists of two variable capacitors, one of them being on the RF power supply side and the other one on the RF coil side. A variable inductor is placed between the two capacitors, and this makes the circuit look like the letter 'T'. By adjusting the variable capacitors and inductors, the capacitance, inductance and additional resistance (resulting from impedance of the RF coil and plasma) are canceled and the impedance is matched to 50 Ω. Matching network is very important for the coupling of the power supply and RF coil and minimizing the reflected RF power.
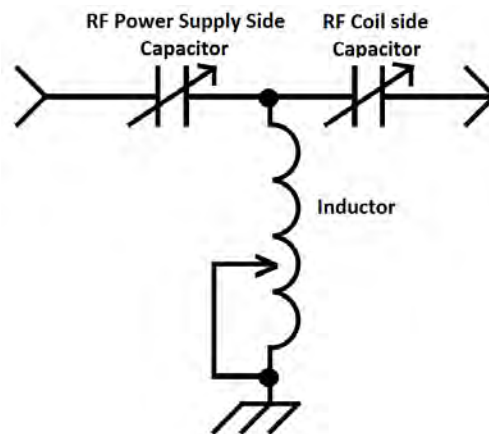
Figure 3.5. Schematic of T-type matching network[62].

A schematic of the RF configuration is shown in Figure 3.6. RF power source is connected to the matching network via an RG393 coaxial cable. Another RG393 cable

is used between the output of the matching network outside of the vacuum chamber. The RF power is carried from the outside of the vacuum chamber to inside by a N-type feed-through. Both sides of this feedthrough have female N-type connectors and the male N-type connectors at the ends of the cables are attached to the feedthrough. On the vacuum side, a third RG393 cable is used to carry the RF power. This RG393 cable is open-ended, and the metallic shield layer of it is attached to one end of the RF coil and the center core of the cable is attached to the other end of the RF coil.

RF coil is built using a 4 mm outer diameter hollow copper tube. Using this configuration, the RF power is applied to RF coil (and plasma) efficiently.
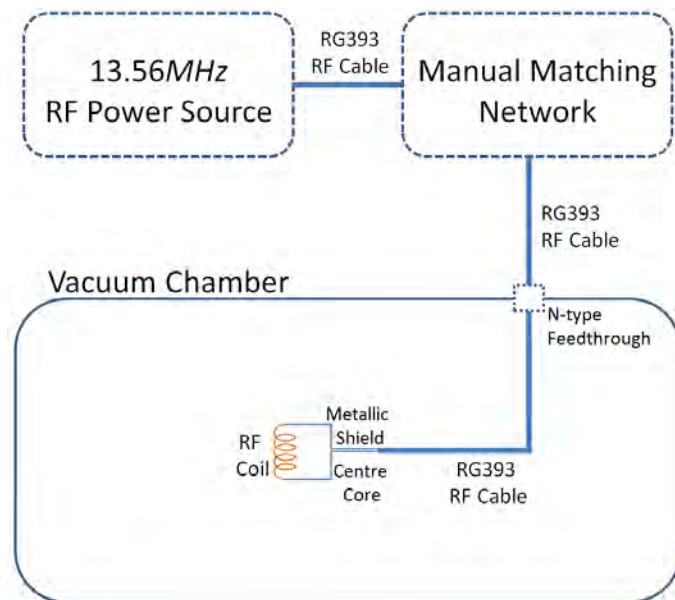
Figure 3.6. Schematic of the radio frequency configuration of the RF plasma cathode experiments.

3.4. DC Power Source Configuration

The DC power configuration of the RF plasma cathode is shown in Figure 3.7. The DC power supply employed in the RF plasma cathode experiments is a product of Glassman High Voltage Inc. and its model is PS/FL1.2F1.2. This device is a 1.5 kW DC power supply which could provide maximum DC voltage of 1250 V and maximum DC current of 1.2 A. The device could be programmed in order to apply different bias voltages. The electron current of the DC circuit could be read and saved in a computer

by connecting the DC power supply to the computer. So, the I-V characteristics of the RF plasma cathode could be obtained using this power supply.

The DC power is carried through a DC feedthrough into the vacuum chamber. Inside the vacuum chamber, the positive contact is connected to the biased electrode, and the negative contact is connected to the ion collecting electrode inside the RF plasma cathode. The bias voltage is increased gradually and the current is read from the device.
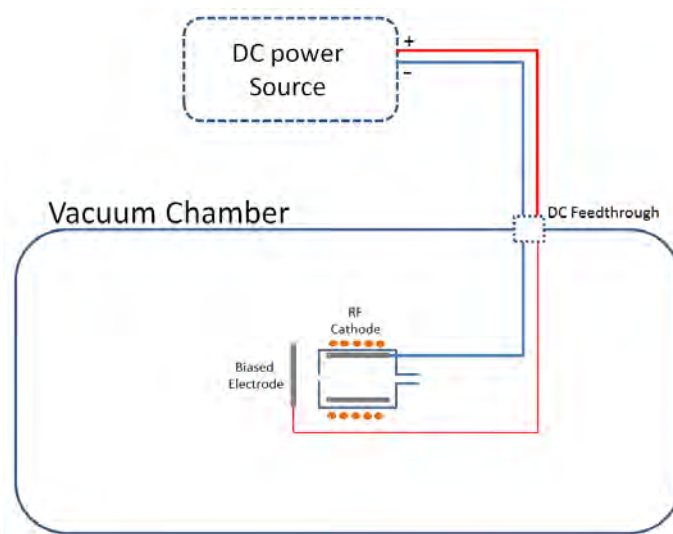
Figure 3.7. Schematic of DC power configuration of the RF plasma cathode experiments.

4. EXPERIMENTAL RESULTS

Experimental results of two different concepts of the RF plasma cathode device are described in this chapter. Effect of different geometric and operational parameters on the plasma generation and electron extraction characteristics of the RF plasma cathode are presented. Also, the effect of the operational parameters (mass flow rate and RF power) on the ICP plasma is studied by measuring electron density and electron temperature inside the chamber of the RF plasma cathode. These measurement are conducted by means of a home-built double Langmuir probe.

4.1. Results of the Prototype RF Plasma Cathode Experiments

Plasma cathode device operation consists of two parts: 1) plasma generation, 2) electron extraction. In the experimental study of the prototype RF plasma cathode both of these parts are investigated. The experiments are conducted to deduce the main operational characteristics of the RF plasma cathode.

4.1.1. Plasma Generation

Previous studies on the inductively coupled plasma (ICP) have shown that by applying the RF power to the coil, first a capacitively coupled plasma (CCP) forms at low RF powers. Then, by applying more RF power, a sudden change from CCP mode to ICP mode occurs, and the ICP plasma is generated. This abrupt change is known as E-H mode transition [21]. The E-H mode transition is also observed in RF plasma cathode. Figure 4.1 shows the lowest value of the forward RF power, which ignites CCP plasma, for various argon mass flow rates. For mass flow rates lower than 3 sccm, no CCP plasma was observed and ICP plasma was ignited directly. Figure 4.1 shows that by increasing the mass flow rate to 6 sccm, the power needed for CCP ignition becomes less, and for mass flow rates higher than 6 sccm, a constant power is needed to ignite the CCP plasma.
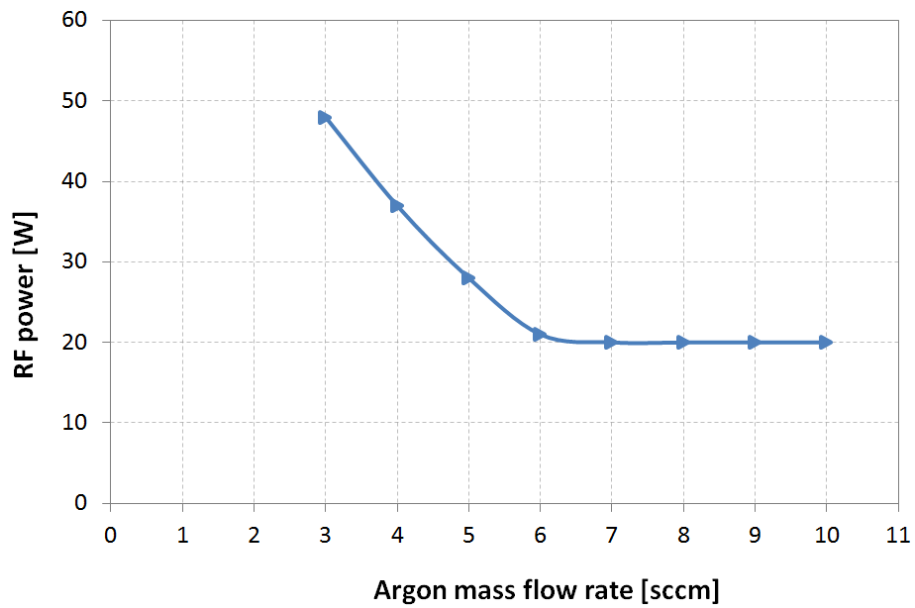
Figure 4.1. Lowest forward RF power needed for CCP generation inside the RF plasma cathode for various argon mass flow rates.

CCP plasma is very dim and is generated only in a small part of the cathode chamber. By increasing the RF power, the CCP plasma becomes more luminous and it encompasses a larger part of the chamber. At a certain value of the RF power, an abrupt transition from CCP to ICP occurs and the plasma becomes very luminous, like a fluorescent lamp. At this point, the ICP plasma is generated. The photograph of the RF plasma cathode operating at the ICP mode is shown in Figure 4.2
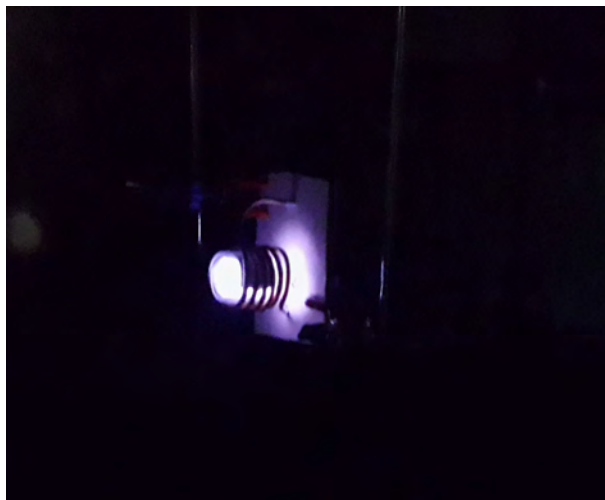
Figure 4.2. RF plasma cathode operating at the ICP mode.

Figure 4.3 shows the lowest forward RF power for ICP generation in the RF plasma cathode, for various argon mass flow rates. Similar to the CCP plasma, the forward power needed for the ICP generation decreases by increasing the mass flow rate from 0.5 to 6 sccm. For mass flow rates higher than 6 sccm a constant power is needed to ignite the ICP plasma inside the RF plasma cathode.
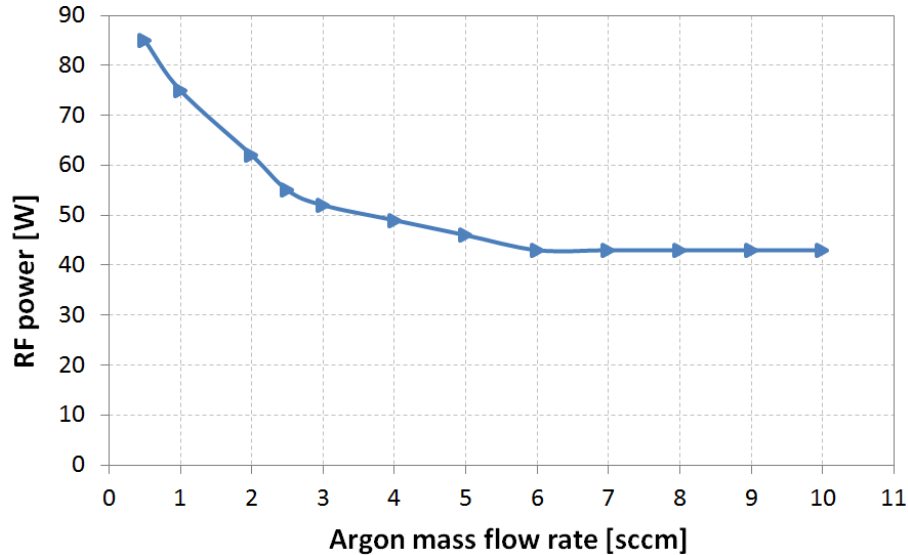
Figure 4.3. Lowest forward RF power needed for E-H mode tarnsition and ICP generation inside the RF plasma cathode for various argon mass flow rates.

After the ICP plasma generated, it could be sustained at lower values of the RF power. So, first the ICP plasma could be generated by higher RF powers, and after that, it could be sustained at very low RF powers. This phenomenon is known as hysteresis and is an important characteristic of the ICP plasma [21]. The RF power values, which could sustain the ICP plasma for various argon mass flow rates, are shown in Figure 4.4. It can be seen from this figure that by increasing the mass flow rate, the lowest RF power needed to sustain the ICP plasma decreases. At 10 sccm of argon mass flow rate, an RF power as low as 9 W is needed to sustain the ICP plasma, after it is generated.
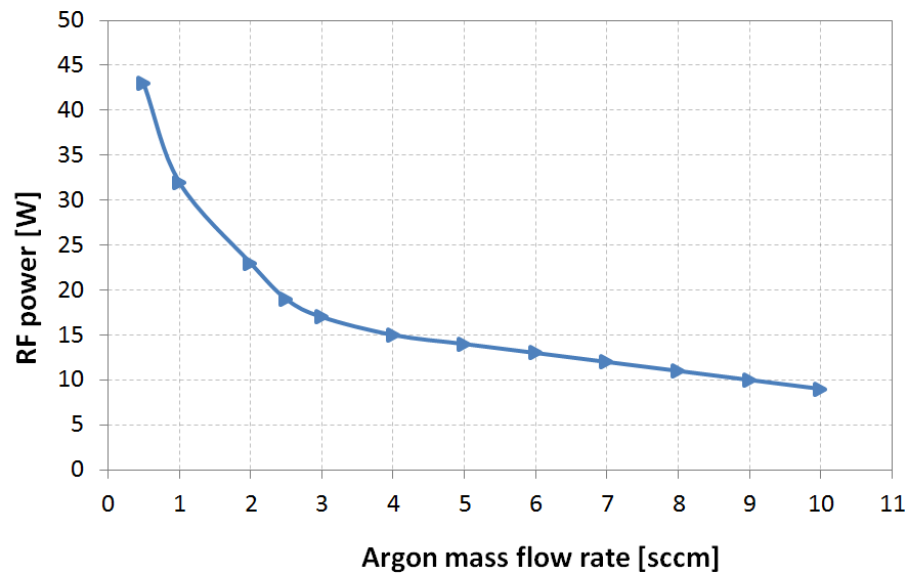
Figure 4.4. Lowest forward RF power which could sustain the ICP plasma inside the RF plasma cathode, after the ICP plasma is generated, for various argon mass flow rates.

4.1.2. Electron Extraction

In order to investigate the electron emission characteristics of the RF plasma cathode, a metallic plate was placed at a 1.5 cm distance from the frontplate of the cathode. The positive electrode of the DC power supply is connected to this plate, and the bias voltage is applied to the RF plasma cathode through it.

The I-V characteristics of the RF plasma cathode for 3 and 4 sccm argon mass flow rates are shown in Figures 4.5 and 4.6. It was observed that before the ignition of the ICP plasma, no current could be extracted from the RF plasma cathode, even by bias voltages as high as 200 V. So, in order to extract current from the cathode, the ICP plasma should be ignited first. At a certain flow rate, in order to extract electrons at the RF powers lower than the value needed for ICP ignition, first, the ICP is ignited by applying the minimum power, and then the power is reduced to the desired value. For example, in order to obtain the I-V characteristics of the device at 3 sccm argon mass flow rate and 25 W RF power, first 52 W (as the minimum power for ICP ignition at 3 sccm mass flow rate) is applied to the cathode, then the RF power is reduced to

25 W. I-V characteristics of the plasma cathode in Figures 4.5 and 4.6 show that at
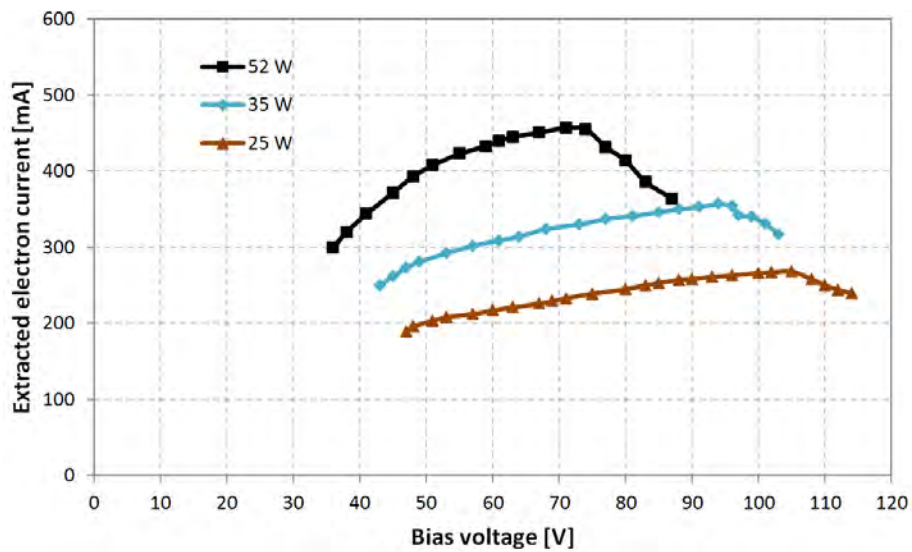
Figure 4.5. I-V characteristics of the RF plasma cathode for 3 sccm argon gas flow rate and variuos RF power values.
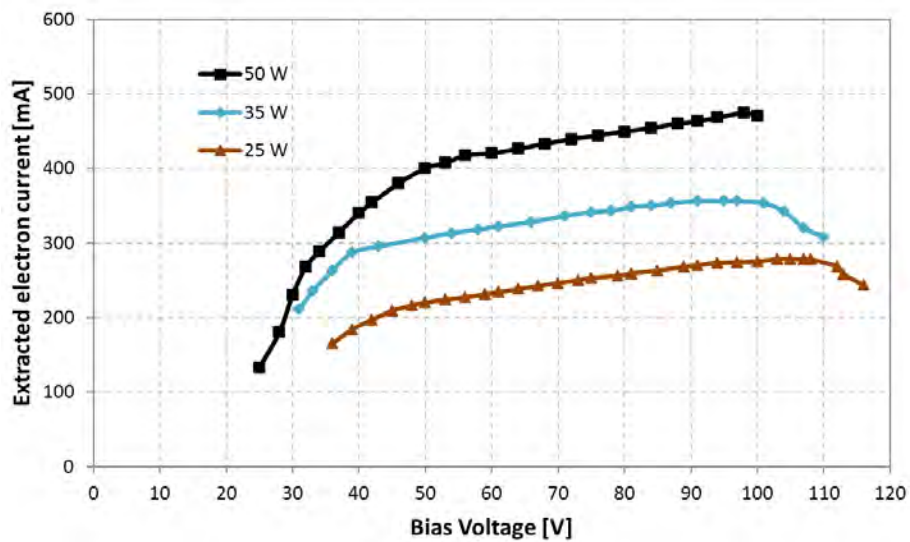
Figure 4.6. I-V characteristics of the RF plasma cathode for 4 sccm argon gas flow rate and variuos RF power values.

low bias voltages, the collected current is nearly zero. At a certain bias voltage, a jump in the extracted current is observed and secondary plasma, which is more luminous, is generated at the orifice of the cathode. As described in Chapter 2, this secondary plasma is anode spot. From this point on, by increasing the bias voltage, the extracted

current increases to a maximum value. When the bias voltage is increased to higher values, the plasma becomes unstable and the extracted current drops. When the bias voltage is increased to a certain value, the bias voltage effect extinguishes the ICP plasma and the extracted current becomes zero.

Figures 4.5 and 4.6 show that at a constant mass flow rate, for higher RF powers, the current jump occurs at lower bias potentials. For example, at 3 sccm mass flow rate, the current jump occurs at 36 V for 52 W, and at 47 V for 25 W. Also, by increasing the RF power, the extracted current increases. It is observed that the extinguishing of the ICP plasma due to high bias voltage occurs at higher voltages for lower value of the RF power. It means that at lower RF powers, the ICP plasma could be sustained at higher values of the bias voltage.

In order to investigate the effect of the mass flow rate on the extracted current, the I-V characteristics of the cathode at 3 and 4 sccm of argon mass flow rates, and 40 W of RF power are compared. As shown in Figure 4.7, by increasing the mass flow rate, the jump in the extracted current occurs at lower bias voltages. Also, at a certain bias voltage, the extracted current is higher for higher mass flow rates.
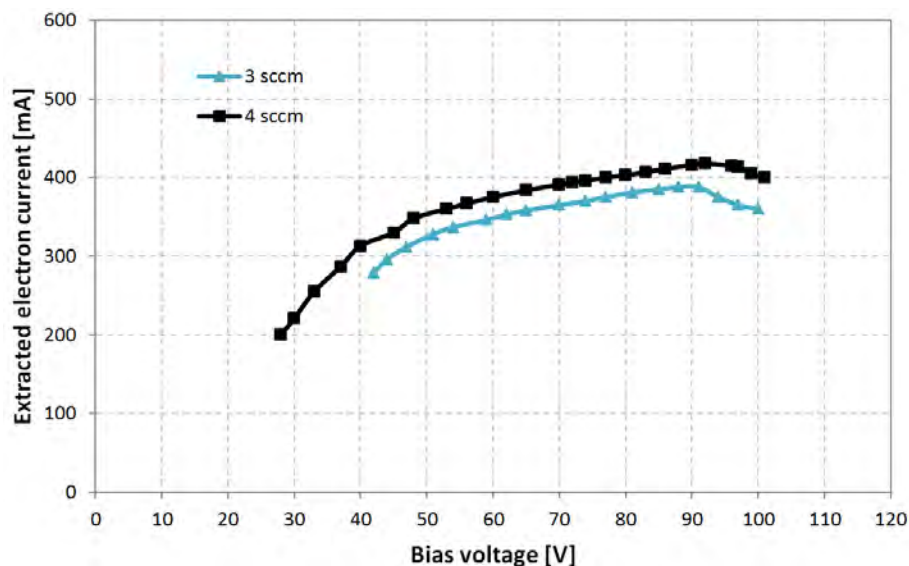
Figure 4.7. I-V characteristics of the RF plasma cathode for 3 and 4 sccm argon gas flow rate and 40 W RF power.

4.1.3. Operation of the RF Plasma Cathode with Cusped Field Hall Thruster

The plasma cathode was used as the electron source and neutralizer of a home-built 40 mm diameter cusped field Hall thruster (CFHT-40) at the BUSTLab. As expected, the RF plasma cathode operating at the ICP mode was capable of instantaneous initiation, and was able to sustain the thruster operation. It could provide currents as high as 1.2 A, which is the current limit of the DC power source used to operate the thruster. A photograph of the CFHT-40 thruster operating with the RF plasma cathode is shown in Figure 4.8. However, at the CCP mode, the cathode was not able to initiate the plasma of the thruster.

Figure 4.8. Cusped field Hall thruster operating with the RF plasma cathode.

4.2. Double Langmuir Probe Measurements of the RF Plasma Inside the Prototype RF Plasma Cathode

A home-built double Langmuir probe is employed in order to determine the effect of mass flow rate and RF power on the plasma parameters (electron density and electron temperature) of the RF plasma inside the cathode chamber. The double Langmuir probe is manufactured by Mert Satır, and the measurements that are presented in this section are conducted with his help. More details about the double Langmuir probe and its measurements could be found in Mert Satır's M.S. thesis [63]. The experimental results of the electron temperature and electron density for 70 W constant RF power and various mass flow rates are shown in Figures 4.9 and 4.10, respectively. In these experiments, the plasma always was in ICP regime. As can be seen from this figures, by

increasing the mass flow rate, the electron temperature decreases and electron density increases inside the ICP plasma. This is because by increasing the mass flow rate, more collisions occur inside the plasma, which leads to higher electron generation, and hence, higher electron density. On the other hand, by increasing the collisions inside the plasma, electrons lose more energy in collisions, which results in decreasing the electron temperature. The other observation is that for some value of the mass flow rate, the electron density reaches to a maximum values, and does not increase by increasing the mass flow rate. This is because of the energy of the electrons is not enough for further ionization and generation of further electrons. In this condition, the electron density of the plasma is limited by the applied RF power.
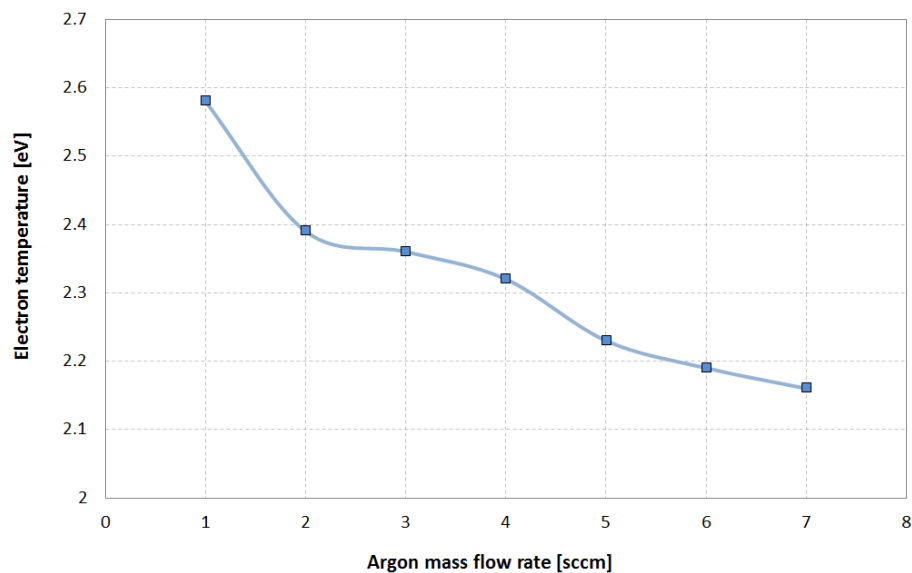
Figure 4.9. Electron temperature of the ICP plasma inside the prototype RF plasma cathode plasma for 75 W RF power and various mass flow rates.

Electron temperature and electron density of the RF plasma inside the prototype RF plasma cathode for 3.3 sccm of argon flow rate and various RF powers are shown in Figures 4.11 and 4.12, respectively. It can be observed from this figures that by gradually increasing the RF power, first a CCP plasma is formed, which has low electron density and electron temperature. By increasing the power, the density and temperature of the CCP plasma increases. For some values of the RF power, an abrupt transition from CCP to ICP plasma occurs, which has a dramatic effect on the electron temperature and electron density of the RF plasma. In this study, the electron
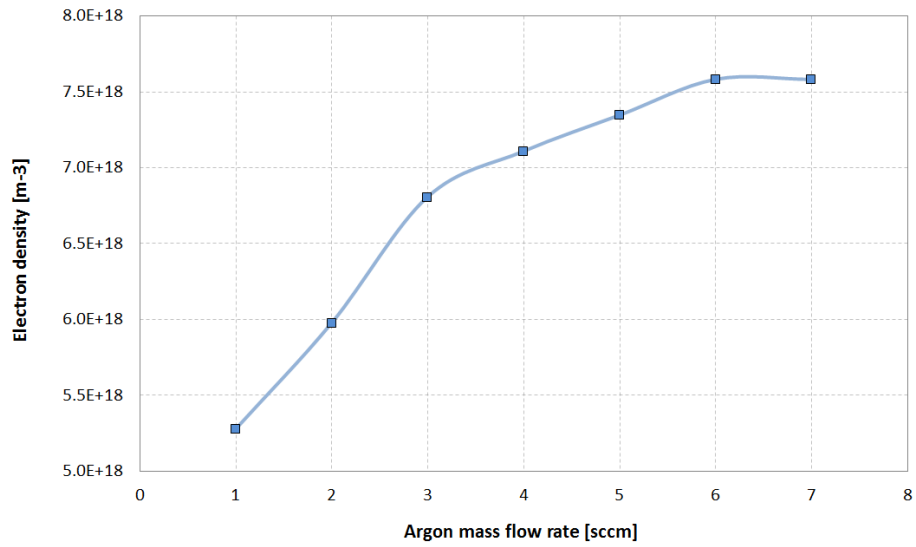
Figure 4.10. Electron density of the ICP plasma inside the prototype RF plasma cathode plasma for 75 W RF power and various mass flow rates.

temperature jumped from 2 eV at 95 W RF powers, to 3 eV at 120 W RF powers, by E-H mode transition. The electron density also jumps from 1.3×10^{16} m^{-3} to 10^{19} m^{-3}. After the formation of the ICP plasma, increasing the RF power gradually increases the electron temperature and electron density.
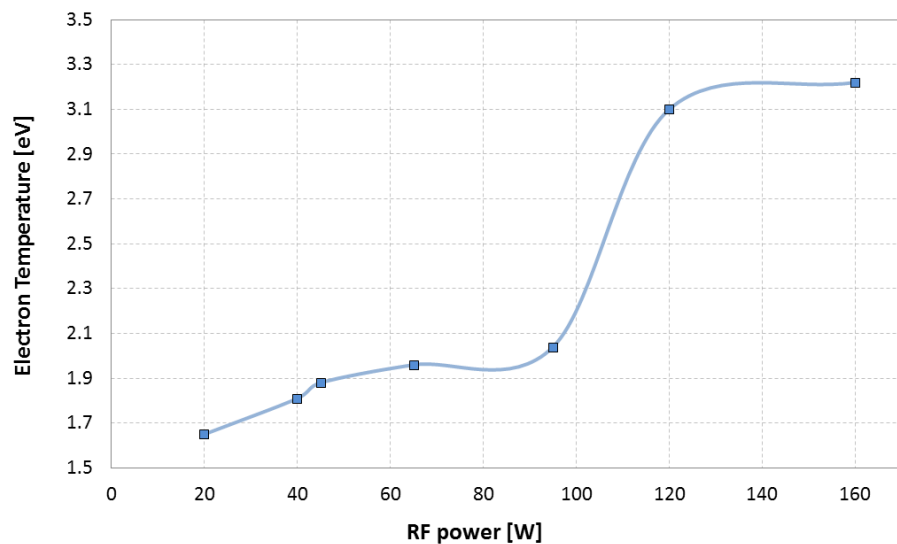
Figure 4.11. Electron temperature of the RF plasma inside the prototype RF plasma cathode for 3.3 sccm of argon flow rate and various RF powers.
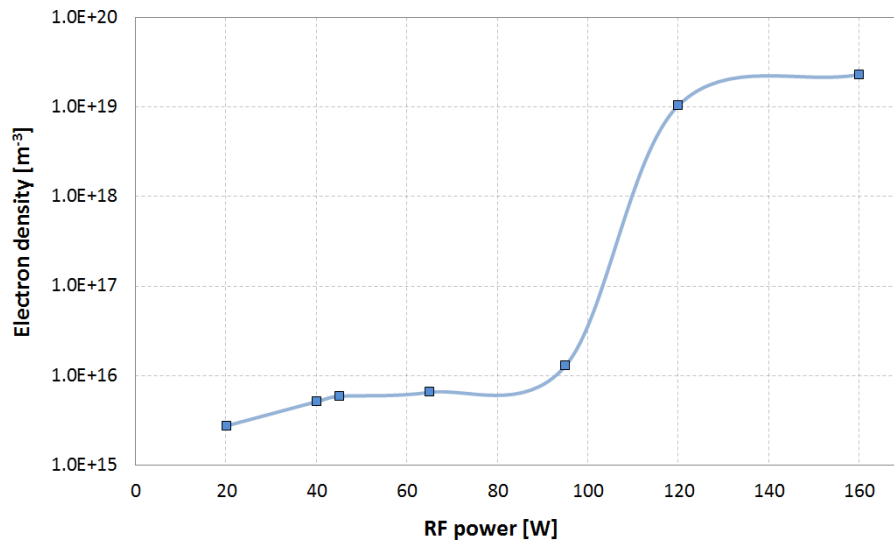
Figure 4.12. Electron density of the RF plasma inside the prototype RF plasma cathode for 3.3 sccm of argon flow rate and various RF powers.

4.3. Effect of Different Geometric Parameters on the RF Plasma Cathode Operation

In order to investigate the effect of different geometric parameters, five prototype RF plasma cathodes are manufactured. Sizes of different geometric parameters of these RF plasma cathodes are presented in Table 4.1. Using these RF plasma cathodes, the effect of chamber length, chamber diameter, orifice diameter, and ion collector electrode area on the plasma generation and electron extraction characteristics of the RF plasma cathode can be investigated.

Effect of the length of the chamber on the operation of the RF plasma cathode could be deduced by comparing experimental results of the cathode #2 and cathode #3. For the effect of the chamber diameter, cathode #1 and cathode #2, for the effect of the orifice diameter, cathode #1 and #4, and for the effect of the ion collector area cathode #1 and #5 should be compared.

The only fix component in the parametric study is the RF antenna of the device. The employed antenna is a 5 turn antenna with an inner diameter of 42 mm and length of 40 mm.

Table 4.1. Sizes of different geometric parameters of the manufactured RF plasma cathodes.

RF Plasma Cathode	Chamber Diameter (D)	Chamber Length (L)	Orifice Diameter (D_O)	Ion Collector Area
#1	40 mm	40 mm	1 mm	20 cm^2
#2	30 mm	40 mm	1 mm	20 cm^2
#3	30 mm	50 mm	1 mm	20 cm^2
#4	40 mm	40 mm	2 mm	20 cm^2
#5	40 mm	40 mm	1 mm	30 cm^2

4.3.1. Plasma Generation

The normal way for plasma generation inside the chamber of the device is to find the best matching setting for the matching network, and after that gradually increasing the RF power. In the plasma generation experiments, the argon mass flow rate is set to a constant value, then the RF power is increased to generate the CCP and ICP plasma. After the generation of the ICP plasma, the RF power is decreased to record the lowest power that ICP plasma could be sustained (hysteresis). In these experiments, it was observed that the antenna geometry and its position with respect to the cathode is an important factor in plasma generation. For example, when a 55 mm inner diameter antenna was used, the plasma could not be ignited in most of the cathodes. Considering this, no plasma could be generated in cathode #2 by the plasma generation process explained above (even with the 42 mm inner diameter antenna).

As described in the previous section, at low RF powers a capacitively coupled plasma forms inside the cathode chamber. The lowest RF powers that can ignite a CCP plasma inside RF plasma cathodes are shown in Figure 4.13. The experiments are done from 0.5 to 10 sccm of argon mass flow rates. As can be seen in this figure, by increasing the mass flow rate, the power needed for CCP generation drops for a particular value of the mass flow rate. By increasing the mass flow rate to higher values, the power needed for CCP ignition remains constant. Cathode #3 needs the highest RF power to ignite the CCP power. Most probably, it is because of the inner diameter of the antenna, which is not close to the chamber wall of the cathode with the diameter of 30 mm.
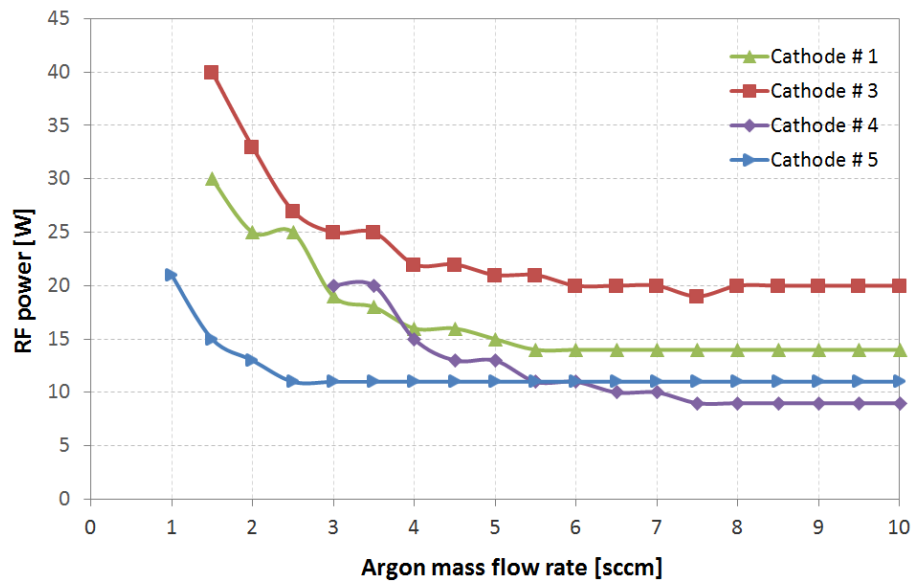
Figure 4.13. Lowest RF powers that can ignite a CCP plasma inside the RF plasma cathodes.

The lowest RF powers that can ignite an ICP plasma inside the cathodes are shown in Figure 4.14. In some cathodes, at low mass flow rates, no ICP plasma could be ignited. Similar to the CCP generation, the power needed for ICP ignition is higher, and it decreases by increasing the mass flow rate. When mass flow rate is increases to a specific value, by further increasing the mass flow rate the power needed for ICP ignition does not change and remains constant.

Like the CCP plasma ignition, cathode #3 has the poorest performance in the ICP generation. It is due to the antenna geometry and coupling with the gas. The first ICP plasma is observed at 3 sccm of argon in cathode #4. But, this cathode needs the lowest power for ICP generation. The orifice diameter of the cathode #4 is 2 mm, and in low mass flow rate conditions the pressure of the gas inside the cathode is not enough for ICP plasma ignition. The ignition of the ICP plasma inside the cathode #4 at low RF powers is considered to be due to gas flow characteristics of this cathode.

The hysteresis characteristics of the ICP plasma inside the cathodes are shown in Figure 4.15. Also for the ICP plasma sustainment, at lower mass flow rates a higher power is needed, and the power decreases to a constant value for higher mass flow rates.
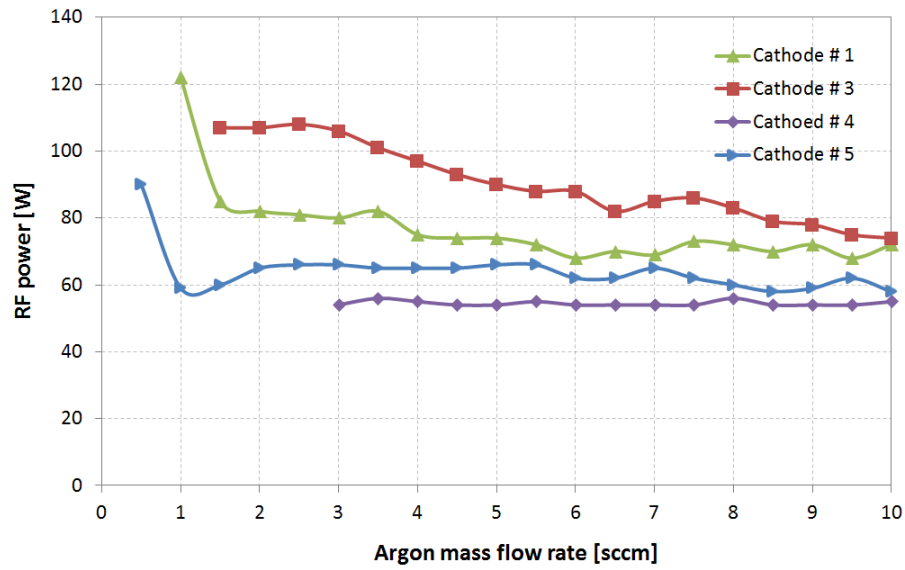
Figure 4.14. Lowest RF powers that can ignite a ICP plasma inside the RF plasma cathodes.

Except cathode #5, the cathodes need nearly the same RF power to sustain the ICP plasma.

Figure 4.15. Lowest RF powers that can sustain an ICP plasma inside the RF plasma cathodes.

An alternative method of ICP plasma generation is found during the experiments. This method is based on finding the best settings of the matching network for ICP plasma, and direct ignition of the ICP plasma by applying the RF power in-

stantaneously to the antenna. The best settings could be found by igniting an ICP plasma using the previous method of the plasma generation, and finding the matching network settings that have the lowest reflected power in ICP plasma. After finding these settings, they can be recorded and used for the same antenna, regardless of the cathode chamber properties.

The lowest RF powers that can ignite an ICP plasma inside the RF plasma cathodes using the alternative method of the ICP ignition are shown in Figure 4.16. The results of Figure 4.16 show that the power needed for ICP generation inside the RF plasma cathodes is considerably smaller compared with the previous method of the plasma generation. For example, using the previous method of the plasma generation, 74 W of RF power in 5 sccm of mass flow rate is needed to ignite the ICP inside the cathode #1, while this value is 17 W for the alternative ICP plasma generation method. Since the main purpose in RF plasma cathodes is to generate the ICP plasma, this method is considered as a proper and efficient method of plasma generation.

As mentioned above, no plasma could be generated inside the cathode #2 using the normal method. But using the alternative method, the ICP plasma is generated directly in this cathode at relatively low RF powers. As can be seen in Figure 4.16, the cathode #2 needs the highest power for ICP ignition, which is due to the antenna geometry, and the other cathodes need nearly the same power for ICP ignition.

4.3.2. Electron Extraction

A metal plate is placed 2 cm away from the orifice of the cathode. The positive potential is applied to this plate in order to extract electrons from the cathodes.

Similar to the studies of the previous section, it was observed that no electron current could be extracted before the ignition of the ICP plasma. In addition, the jump in the extracted electron current by the formation of the anode spot is observed in all experiments. A picture of the RF plasma cathode during current extraction is shown in Figure 4.17. The luminous ICP plasma, and the anode spot generated in the
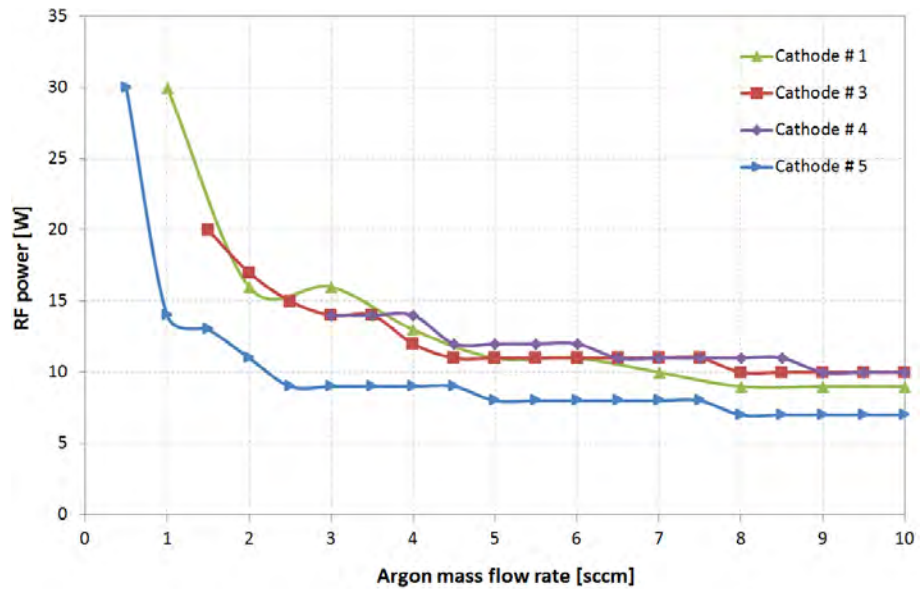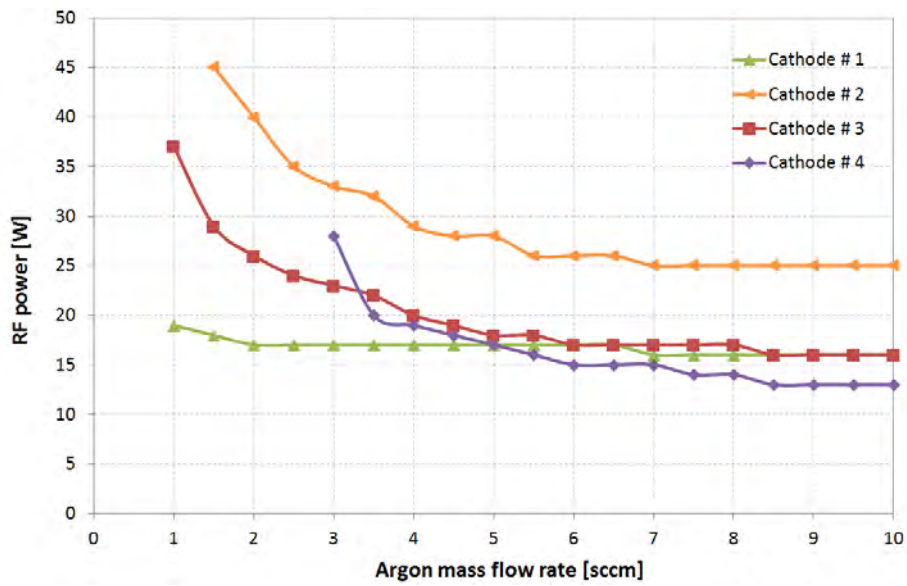
Figure 4.16. Lowest RF powers that can ignite a ICP plasma inside the RF plasma cathodes using the alternative method of the ICP ignition.

orifice of the cathode can be seen from this picture. The current extraction experiments has been conducted for various gas flow rates and power levels, and effect of the each geometric parameter on the current extraction from the device is investigated.

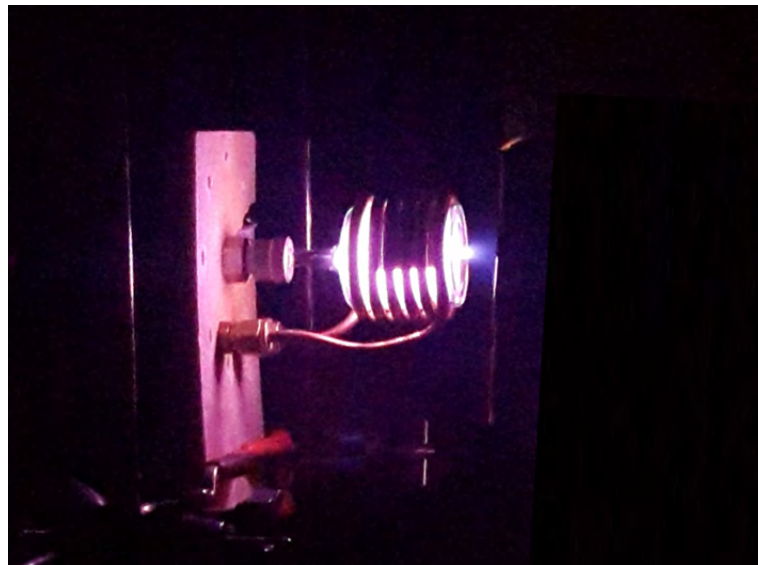Figure 4.17. Picture of the RF plasma cathode during current extraction, the luminous anode spot could be seen in the orifice of the device.

I-V characteristics of the cathode #2 for 70 W power and various gas flow rates are shown in Figure 4.18. These sets of the experiments are conducted for all of

the cathodes, and results of the cathode #2 are presented as an example of these experiments. As can be seen from Figure 4.18, at constant RF power, by increasing the mass flow rate from 0.5 sccm to 5 sccm, the extracted current increases. But by increasing the mass flow rate further to 7 and 10 sccm, the extracted current decreases. The only exception is the cathode #4, which has larger orifice diameter. The current jump and anode spot formation occurs at lower bias voltage for higher mass flow rates. No exception was observed for this result.
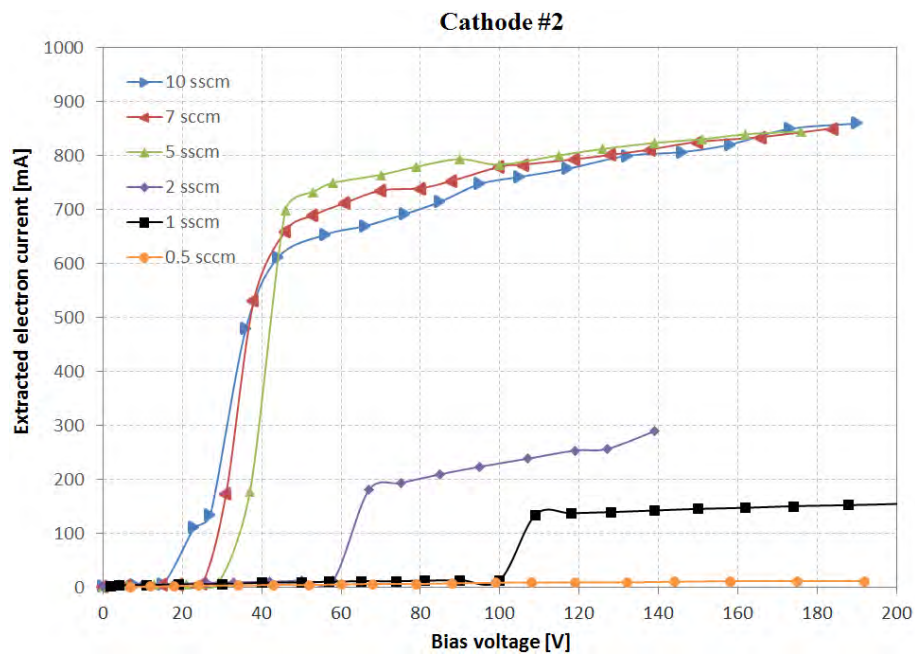
Figure 4.18. I-V characteristics of the cathode #2 for 70 W RF power and various gas flow rates.

I-V characteristics of the cathode #2 for 6 sccm of argon flow rate and various RF powers are shown in Figure 4.19. These sets of experiments are also conducted for all the cathodes, and the results for the cathode #2 are put here as representatives. As can be seen in this figure, by increasing the RF power, the extracted current increases.

The effect of the diameter of the chamber of the cathode (D) on the electron extraction characteristics of the device could be investigated by comparing I-V results of the cathode #1 and cathode #2. The chamber diameter of cathode #1 is 40 mm, while the chamber diameter of the cathode #2 is 30 mm, and the other geometric parameters are the same for these cathodes. The I-V characteristics of the cathode
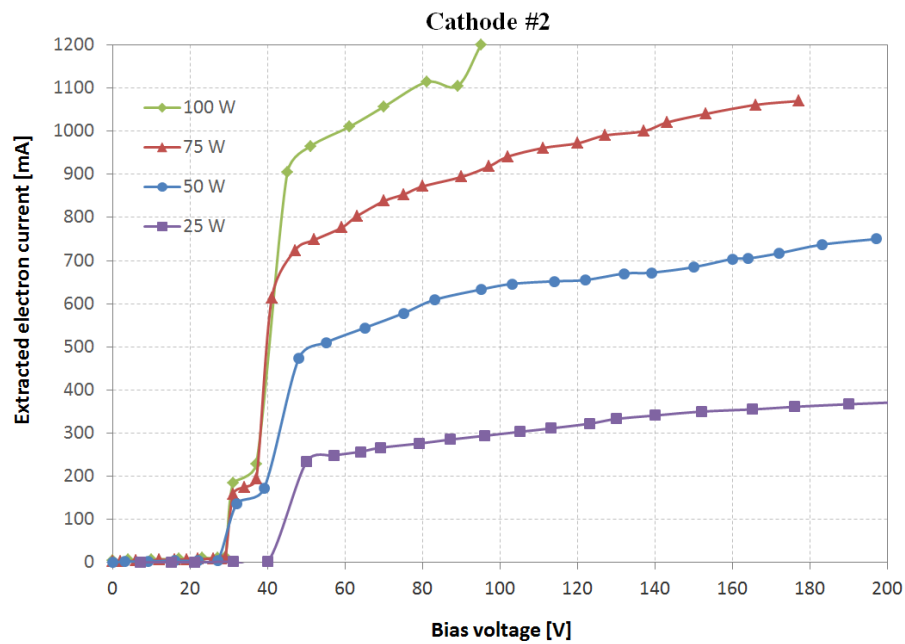
Figure 4.19. I-V characteristics of the cathode #2 for 6 sccm of argon flow rate and various RF powers.

#1 and #2 for various flow rates and powers are shown in Figures 4.20 and 4.21. For all these results, for the same flow rates and RF powers, the extracted current from cathode #2 is higher than the extracted current from cathode #1. It shows that the extracted electron current becomes higher by the diameter of the cathode being smaller. This could be due to higher gas pressure and neutral density inside the smaller cathode, which increases the plasma density inside the cathode. When the density of a plasma is higher, it could emit more electrons.

In order to investigate the effect of the length of the cathode on the electron extraction characteristics, extracted electron from cathode #2 and #3 are compared. As presented in Table 4.1, the only difference of the cathode #2 (L = 40 mm) and cathode #3 (L = 50 mm) is their length. The I-V characteristics of the cathode #2 and #3 for various flow rates and powers are shown in Figures 4.22 and 4.23. The results of these figures show that for the same mass flow rates and RF powers, the extracted electron current from the cathode #2 (L = 40 mm) is higher. This means that cathode with smaller length has a better performance in terms of the electron emission. Similar to the chamber diameter, smaller length leads to higher gas pressure
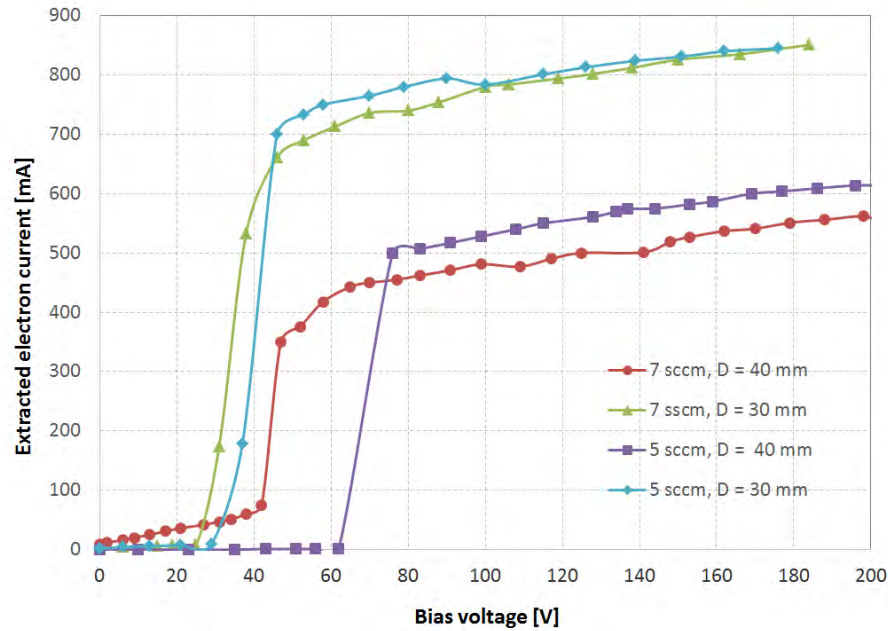
Figure 4.20. I-V characteristics of the cathode #1 (D = 40 mm) and cathode #2 (D = 30 mm) for 70 W RF power, and 5 and 7 sccm gas flow rates.

Figure 4.21. I-V characteristics of the cathode #1 (D = 40 mm) and cathode #2 (D = 30 mm) for 6 sccm argon flow rate, and 50 and 75 W RF powers.

and neutral density inside the smaller cathode, and denser plasma, which could emit more electrons.
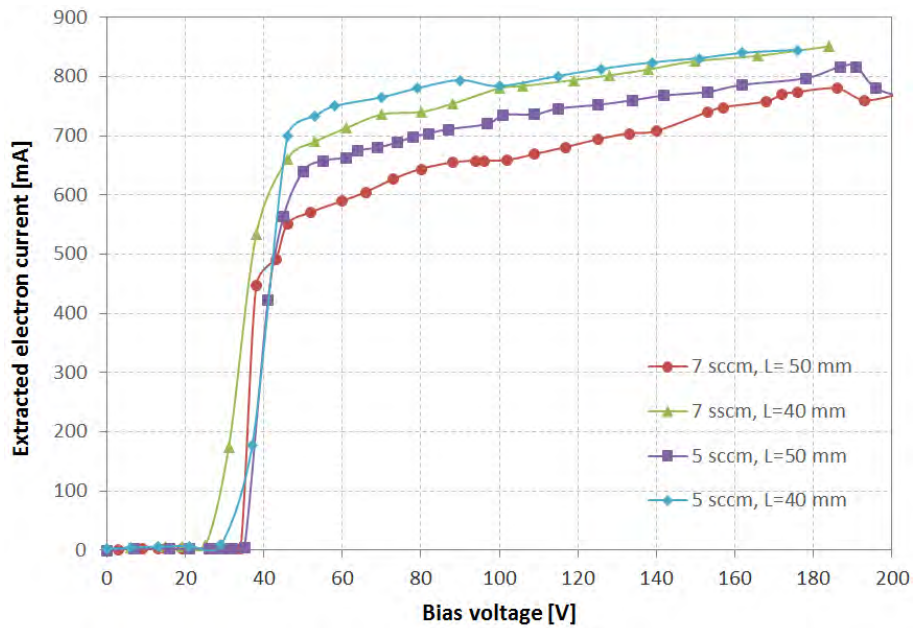
Figure 4.22. I-V characteristics of the cathode #2 (L = 40 mm) and cathode #3 (L = 50 mm) for 70 W RF power, and 5 and 7 sccm gas flow rates.

Figure 4.23. I-V characteristics of the cathode #2 (L = 40 mm) and cathode #3 (L = 50 mm) for 6 sccm argon flow rate, and 50 and 75 W RF powers.

Cathode #1 and cathode #4 are compared to understand the effect of the orifice diameter on the electron extraction from the RF plasma cathode. These cathodes have the same geometric parameter, except that the orifice diameter (D_O) of the cathode

#1 is 1 mm and that of the cathode #4 is 2 mm. The electron extraction results of the cathode #1 and #4 for various flow rates and powers are shown in Figures 4.24 and 4.25. These experimental results show that the cathode #4, which has larger orifice diameter, could provide more electron currents for the same RF powers and mass flow rates. Although for larger orifice diameters the gas pressure inside the chamber drops, the positive potential penetration into the plasma inside the chamber increases, which could increase the extracted electron current. Results of Figures 4.24 and 4.25 show that for the D_O of 2 mm, the current increasing effect of the potential penetration outweighs the current decreasing effect of the lower gas pressure inside the chamber.
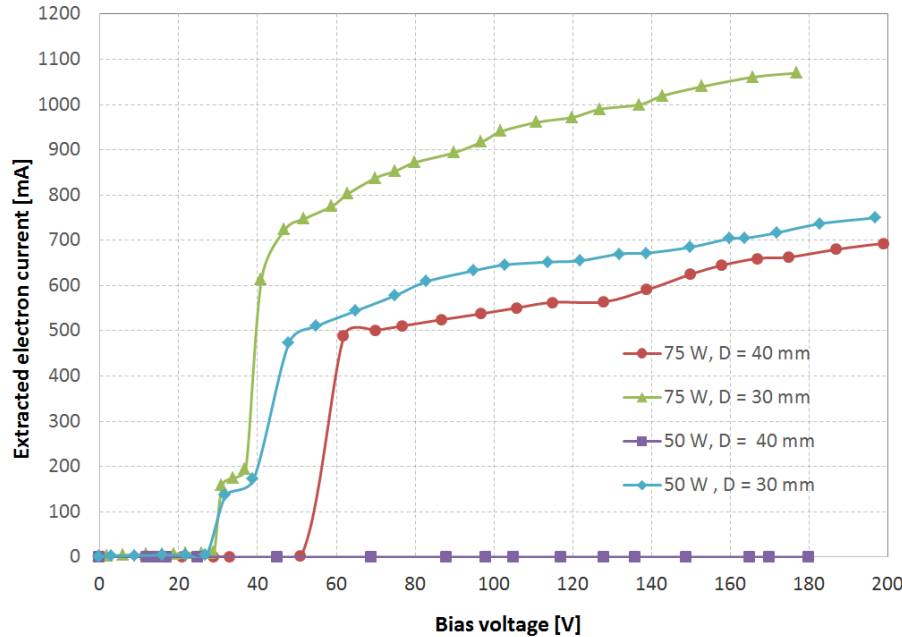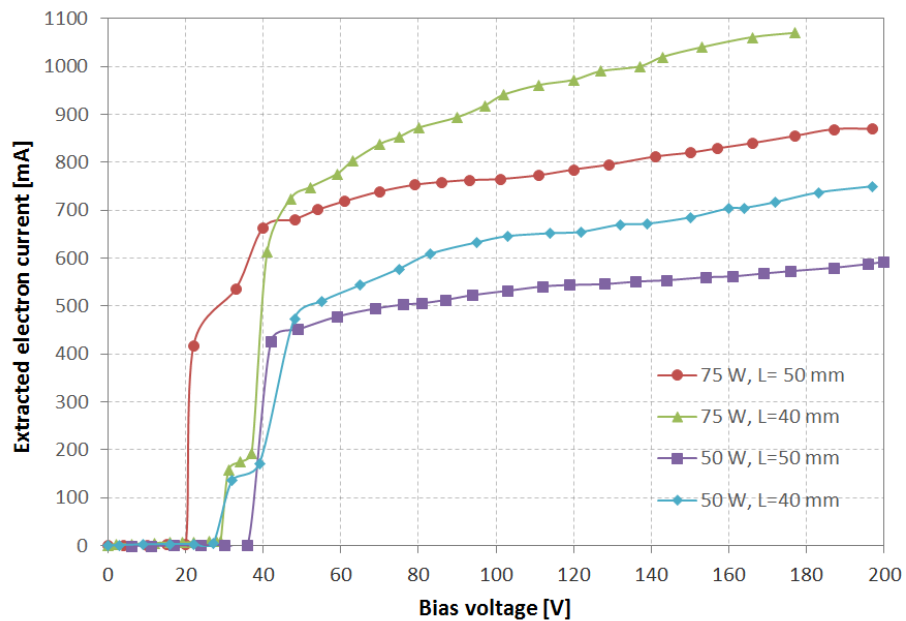

Figure 4.24. I-V characteristics of the cathode #1 (orifice diameter (D_O) = 1 mm) and cathode #4 (D_O = 2 mm) for 70 W RF power, and 5 and 7 sccm gas flow rates.

The last geometric parameter to be compared is the area of the ion collector electrode. The effect of the ion collector on the I-V characteristics of the device could be investigated by comparing the experimental results for cathode #1 and cathode #5, which their only difference is the ion collector electrode area. As presented in Table 4.1, the collector area of cathode #1 is 20 cm^2 and the collector area of the cathode #5 is 30 cm^2. The I-V characteristics of the cathode #1 and #5 for various flow rates and powers are shown in Figures 4.26 and 4.27. For the same RF powers and mass flow rates, the extracted current from cathode #5, which has larger electrode is higher than the cathode #1. Since the plasma inside the chamber is quasineutral, for each electron
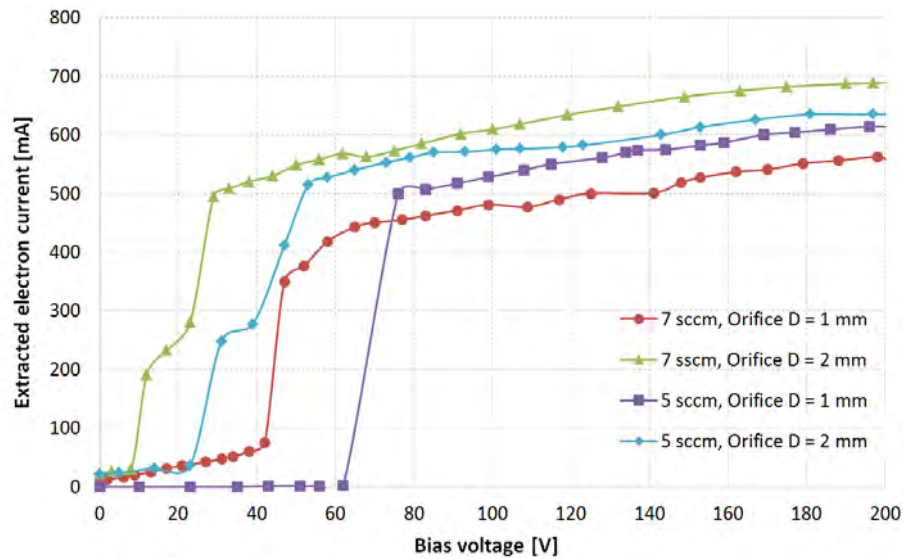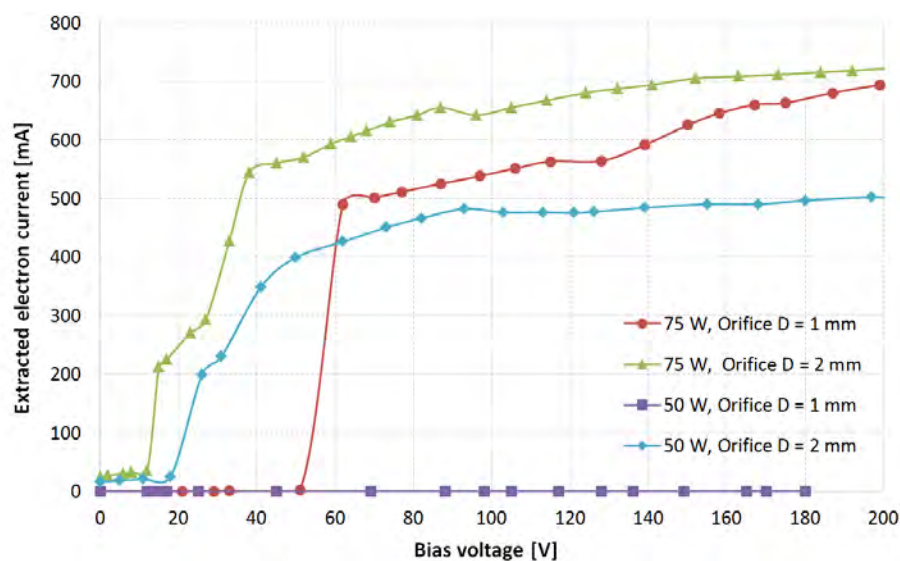
Figure 4.25. I-V characteristics of the cathode #1 (orifice diameter $(D_O) = 1$ mm) and cathode #4 ($D_O = 2$ mm) for 6 sccm argon flow rate, and 50 and 75 W RF powers.

which is lost to the positively biased electrode in front of the orifice of the cathode, an ion should be lost to the ion collector electrode (hit the electrode and become neutral by obtaining an electron from the electrode). So, in the case of the larger electrode, more ions could be lost to the ion collector, and this means that more electrons could be lost to the positively biased electrode, and more electron current could be extracted.

4.4. Advanced RF Plasma Cathode

Although the prototype RF plasma cathode is easy to manufacture and easy to use, some design parameters such as the orifice length could not be controlled properly when manufacturing the cathode chamber. Also, after manufacturing the cathode, the inside of the chamber is unreachable. So, it is not possible to change the ion collector electrode and clean the inside of the chamber, when it is needed. To solve these problems, an advanced version of the RF plasma cathode device was designed and manufactured. The 2D drawing and a picture of this design of the RF plasma cathode are shown in Figure 4.28. In this design, the chamber is also made of pyrex. But, the front plate is not integrated with the chamber. Instead, the chamber is extended
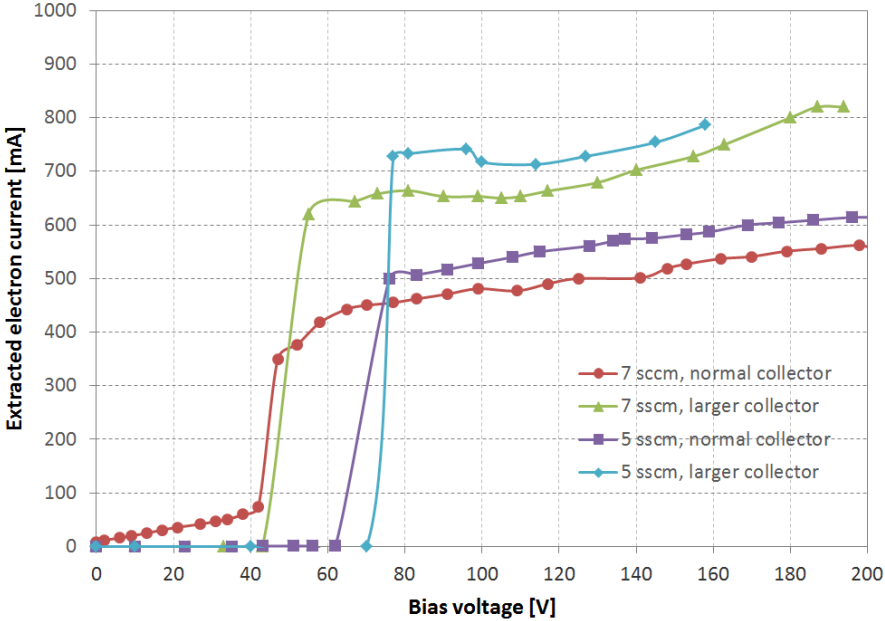
Figure 4.26. I-V characteristics of the cathode #1 (collector area = 20 cm^2) and cathode #5 (collector area = 30 cm^2) for 70 W RF power, and 5 and 7 sccm gas flow rates.
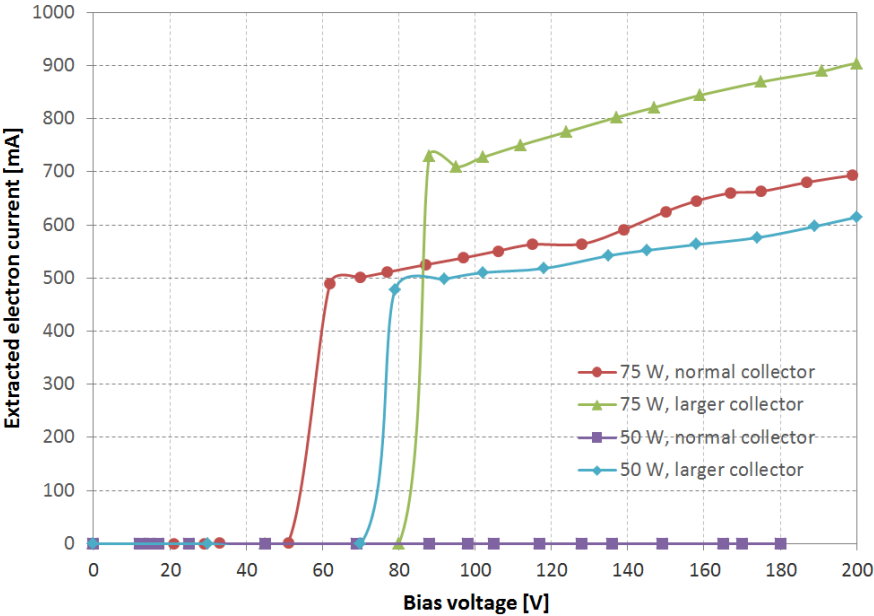
Figure 4.27. I-V characteristics of the cathode #1 (collector area = 20 cm^2) and cathode #5 (collector area = 30 cm^2) for 6 sccm argon flow rate, and 50 and 75 W RF powers.

out to the sides at its end, so that an o-ring between the extended part and the front plate is used to seal gas inside the chamber. The extended part of the chamber is pressed between the front plate and holder, which is placed behind the extended part. By pressing the extented part of the chamber, the o-ring inside the groove of the front plate accomplishes the gas sealing. The chamber and front plate are mounted on a teflon back plate. The RF antenna is also mounted on the back plate.
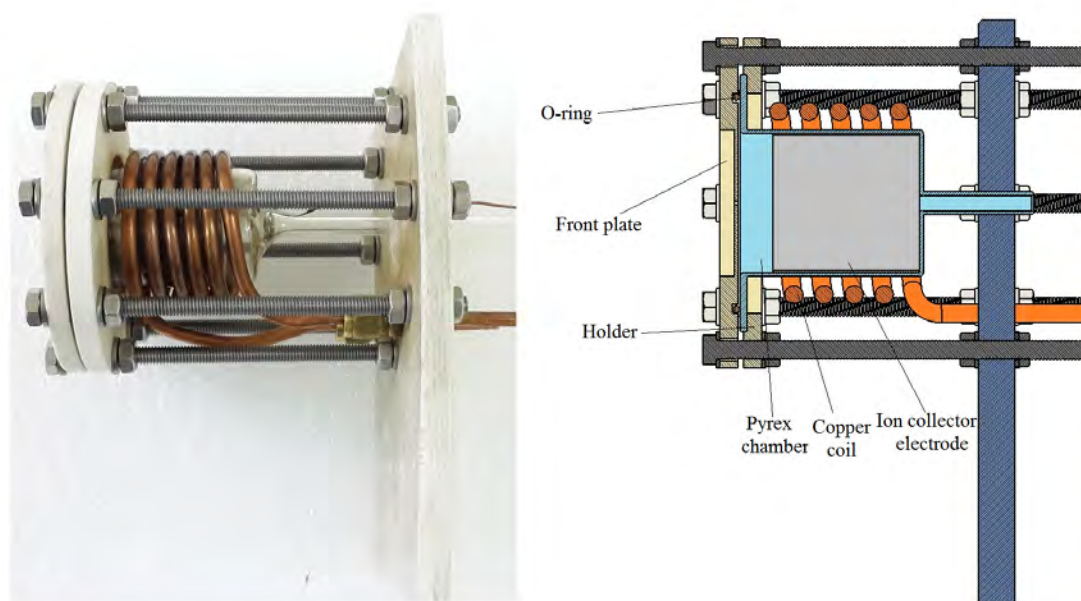
Figure 4.28. 2D drawing and picture of the advanced version of the RF plasma cathode.

In the first design, the front plate was manufactured from teflon, because of easy access and manufacturing. But, during the experimental studies it was observed that the teflon can not stand the heat generated by the formation of the anode spot in the orifice. By the formation of the anode spot, teflon front plate started to burn. Considering this problem, the new front plate was manufactured using machinable glass ceramic (MGC) discs. Pictures of the teflon and MGC front plates after the anode spot generation tests are shown in Figure 4.29. As can be seen in this figure, the teflon front plate has completely burned and deformed due to the effect of the anode spot. In contrast, the anode spot has no effect on the MGC front plate.

Pictures of the experimental setup and operation of the advanced RF plasma
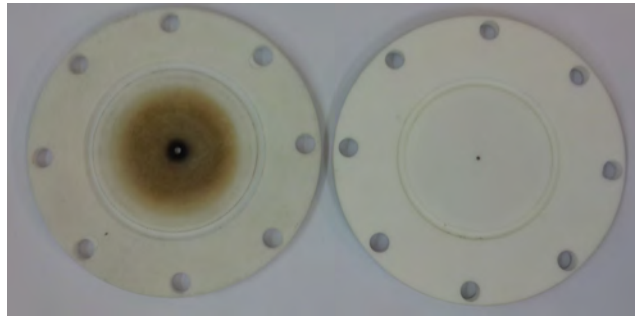
Figure 4.29. Pictures of the teflon and MGC front plates after the anode spot generation tests.

cathode are shown in Figure 4.30. As it is known from the prototype RF plasma cathode experiments, no current can be extracted from the device before ICP plasma generation. During the experimental studies of the advanced RF plasma cathode, an unknown problem was observed regrading the ICP plasma generation inside the device. Because of this problem, the current extraction experiments could not be conducted.

The first reason considered for this problem was the gas sealing. It was considered that the ICP plasma could not be ignited due to undesired confinement of the gas inside the chamber of the device. To solve this, the groove of the o-ring was modified considering the o-ring standards. In spite of this modification, the problem was not solved. It is thought that the problem in due to antenna geometry and coupling, and modifications should be done on the antenna.
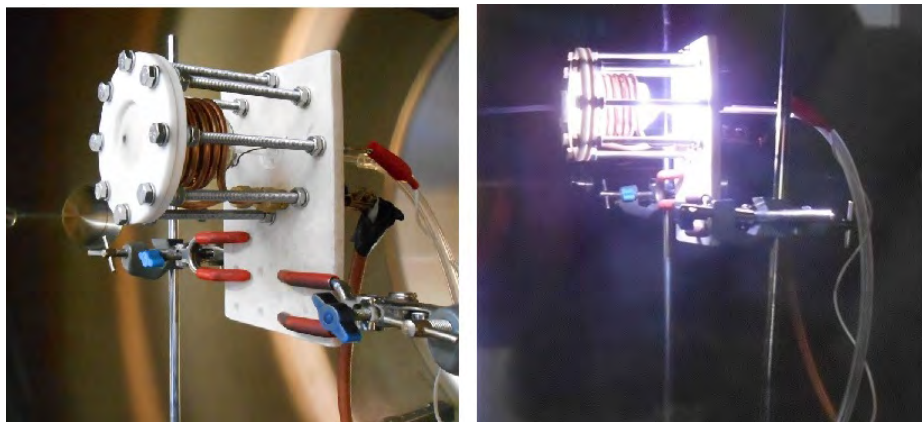
Figure 4.30. Pictures of the experimental setup and operation of the advanced RF plasma cathode.

5. CONCLUSIONS

The main design and operational principles of the plasma cathode devices are presented in this thesis. It is shown that electron emission of the plasma cathode devices strongly depends on the formation of a secondary plasma, named anode spot. This secondary plasma is formed in the orifice of the plasma cathode devices due to a applied positive potential. Before the formation of the anode spot, the extracted electron currents from the plasma cathode devices are negligible. On the other hand, the device starts to emit electrons after the formation of the anode spot.

A wide literature review about the theoretical and experimental studies of the anode spots is presented in this thesis. It is known that anode spot forms by an abrupt transition of the electron sheath in front of a positively biased electrode to a double layer. Since these types of double layer form in front of an anode, they are named as "anodic double layers" to be distinguished from other types of double layers. Some studies have modeled the formation of the anode spot as breakdown of gas between two electrodes, Except that for the case of the anode spot, the plasma breaks down between the two electrodes.

Experimental studies show that anode spot is a very dense and hot plasma. Anode spots are also very luminous and their boundary from the surrounding plasma could be observed by unaided eye. Formation of the anode spot effects the surrounding bulk plasma as well. As shown in Figure 2.11, anode spot formation increases the electron density of the bulk plasma. Other experimental results from Weatherford *et al.*'s study [19] show that the anode spot increases the plasma potential and electron temperature of the bulk plasma as well.

Despite the experimental evidences, which have shown that anode spot has much higher electron density and electron temperature compared to the bulk plasma, most of the theoretical studies in the literature have neglected the contribution of the anode spot to the extracted electron current by the positively biased electrode. These studies

neglected the electron generation inside the anode spot and have considered it only as a pathway for the electrons of the bulk plasma. In this thesis, it is shown that neglecting the electron generation inside the anode spot results in the bulk plasma being much denser than the anode spot. However, it contradicts with the experimental measurements, which have identified anode spot density to be much higher than the bulk plasma density.

Theoretical studies conducted in this thesis propose that the electron generation inside the anode spot is significant and cannot be neglected. In this model, neglecting the electron generation inside the anode spot is not a valid assumption. The high electron generation inside the anode spot and high electron density of the anode spot is related to its non-equilibrium nature. Reasons for the identifying the anode spot as a non-equilibrium steady state plasma are proposed. Kappa distribution function, as a tool for NESS plasmas, is employed to model the ionization rates inside the anode spots. The numeric results of this study show that for specific range of electron temperature, the ionization rate of the NESS plasma in much higher than the Maxwellian plasma. This higher ionization rate is identified as the cause of the significant electron generation inside the anode spot.

Two different concepts of the RF plasma device are designed and manufactured as the experimental study of this thesis. Numerous experimental tests have been conducted with the use of these RF plasma cathodes in order to understand the effect of different operational and geometric parameters on the plasma generation inside the RF plasma cathode and electron extraction from it. The results of the experimental studies show that by applying an RF power to the cathode, first a CCP plasma forms inside the chamber of the cathode. By increasing the RF power, the ICP plasma forms by the abrupt transition of the CCP plasma (known as E-H mode transition). The ICP plasma could be identified by its luminous appearance as well as the different matching characteristics. The experimental studies of this thesis have shown that the ICP plasma could be sustained at much lower RF powers than it was initially generated. This phenomenon is known as "hysteresis." It was observed that by increasing the mass flow rate, the power needed for plasma (CCP or ICP) generation inside the RF

plasma cathode decreased for a particular value of the mass flow rate. By increasing the mass flow rate to higher value, the power needed for plasma generation did not decrease, and remained constant. Also, experimental studies revealed that the antenna geometry and its parameters (such as inner diameter, length, number of turns) play an important role in the plasma generation inside the RF plasma cathode.

In order to extract electrons from the RF plasma cathodes, a metallic plate was placed in front of the orifice of the device. An important observation in the electron extraction experiments was that before the formation of the ICP plasma, the device could not emit electrons. It shows that ICP generation inside the RF plasma cathode is very important in terms of the operation of the device. Also, the I-V characteristics of the device, for which an example is presented in Figure 4.5, show that the device starts to emit electrons from a particular bias potential. At this potential, anode spot forms in the orifice of the device. These results prove the correlation of the jump in the extracted electron current and formation of the anode spot, as presented in the theoretical part of this thesis. After the formation of the anode spot, increasing the bias voltage increases the extracted electron current to a maximum value. After that, increasing the bias voltage makes the plasma unsteady, and in some cases decreases the extracted current. It was observed that when ICP plasma becomes unsteady at high bias voltages, it is extinguished in some cases and the extracted electron current becomes zero. The results of Figure 4.18 show that by increasing the mass flow rate, the extracted electron current increases and reaches a maximum value for a particular value of the mass flow rate, and after that increasing the mass flow rate decreases the extracted electron current. Increasing the RF power increases the extracted electron current as shown in Figure 4.19.

Experimental studies are conducted in order to investigate effects of the geometric parameters on the operation of the RF plasma cathode. In these experiments, four geometric parameters are studied: chamber length, chamber diameter, orifice diameter and ion collector electrode area. It was observed that the smaller length and diameter of the chamber increases the electron current. Also, with larger orifice diameter and ion collector area, the device emits more electron current.

As future work in terms of the numerical study of the plasma cathode devices, the plasma cathode operation could be modeled by considering the formation of the anode spot and the high electron generation inside it. The results of this thesis about the non-equilibrium nature of the anode spot and application of the kappa distribution for it could be implemented in future numerical studies.

Future experimental studies could be conducted in order to evaluate the performance of the RF plasma cathode with different types of the thrusters. Cathode positioning and finding the optimum distance of the cathode from the thrusters could be a part of the studies of the RF plasma cathode performance with thrusters. Also, a lifetime study of the RF plasma cathode could be important in terms of identifying the parameters and components that limit the lifetime of the device.

APPENDIX A: NUMERICAL SIMULATION OF ICP PLASMA INSIDE THE RF PLASMA CATHODE USING COMSOL MULTIPHYSICS

In order to condut a numerical study on ICP plasma characteristics inside the RF plasma cathode, a 3D drawing of the device is generated using SOLIDWORKS. The model is shown in Figure A.1. This model is taken from the Japanese concept of Rf plasma cathode [12]. The 3D model of the RF plasma cathode consists of 4 parts:

  (i) Discharge chamber (with a gas inlet),

 (ii) RF coil,

(iii) Ion collector,

(iv) Front plate (with an outlet orifice).
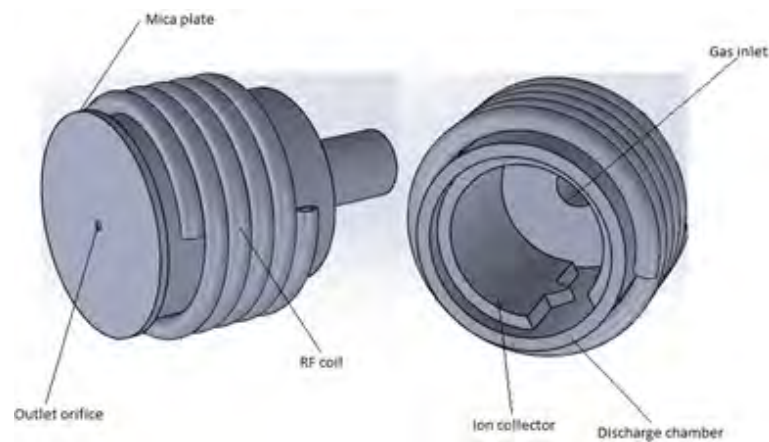
Figure A.1. 3-D model of RF plasma cathode.

Later, this geometry is transferred into COMSOL MULTIPHYSICS in order to simulate the ICP plasma generation inside the chamber of the RF plasma cathode.

COMSOL Multiphysics is a finite element simulation software. This software has a plasma interface that is developed to simulate various types of plasmas, like CCPs (capacitively coupled plasmas), DC discharges, microwave discharges, and ICPs (inductively coupled plasmas). COMSOL Multiphysics Plasma Module uses a series of

scientific publications on numerical modeling of non-equilibrium discharges.

In order to investigate the ICP modeling in COMSOL, a 2-D axi-symmetric model is generated by geometry tool of COMSOL MULTIPHYSICS. This model is shown in Figure A.2. RF plasma cathode itself can not be modeled using a 2D axi-symmetric geometry, because electromagnetic wave can not penetrate ion collector. So, in this model the ion collector is removed, and just forming ICP inside the cathode chamber is considered.
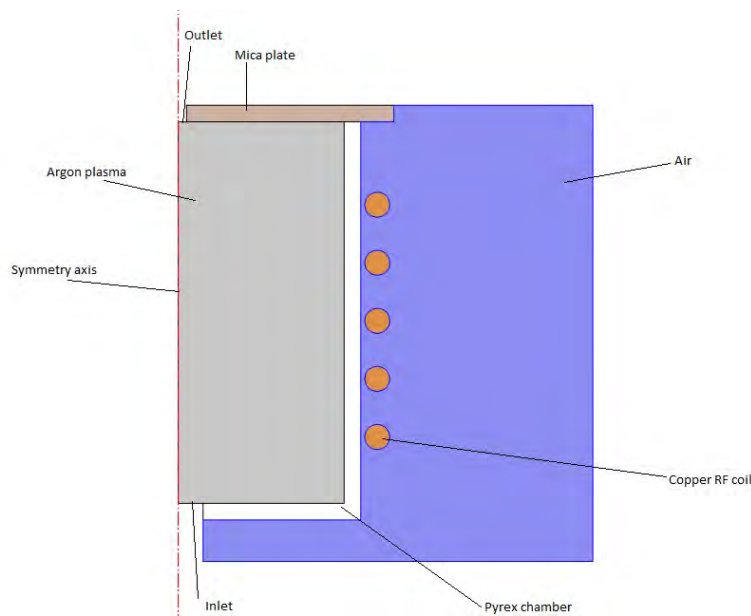
Figure A.2. 2-D model of RF plasma cathode.

The operational conditions which are used in the simulations are: Argon gas is used as plasma fluid. Inlet boundary condition is set to a constant pressure at 21 Pa. Outlet boundary condition is also set to a constant pressure (20 Pa). RF power applied to the coil is 60 W. Chamber walls and front plate are grounded.

Result for the electron density inside the chamber is shown in Figure A.3. This result is consistent with the previous results for ICPs. Maximum electron density is in the center of the chamber and its value is 2.82×10^{18} m^{-3}.
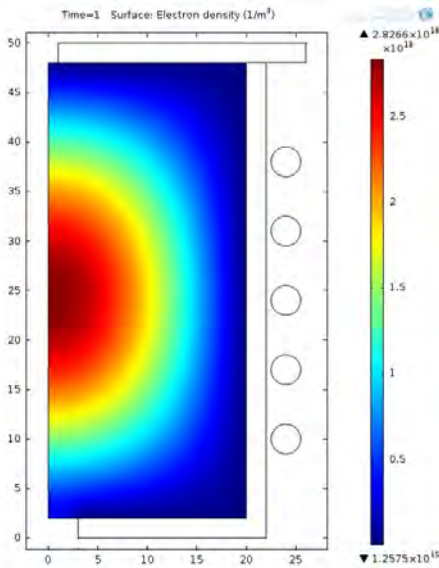
Figure A.3. Electron density inside the plasma chamber.

Results for the plasma potential is shown in Figure A.4. Maximum electric potential is 15 V and is in the center of the chamber. Plasma potential reduces from center to the walls and becomes zero at the wall, because of the set boundary conditions.
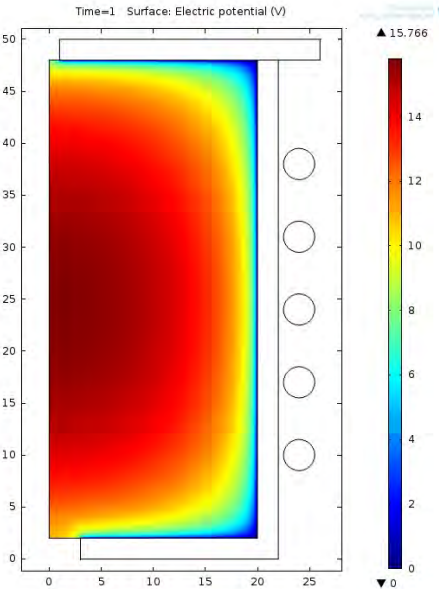
Figure A.4. Plasma potential inside the plasma chamber.

Results for the electron temperature for ICP plasma is shown in Figure A.5. It can be seen that electrons are heated in a region near the RF coil, and RF power is

deposited to plasma from this region. Maximum electron temperature is 2.25 eV.
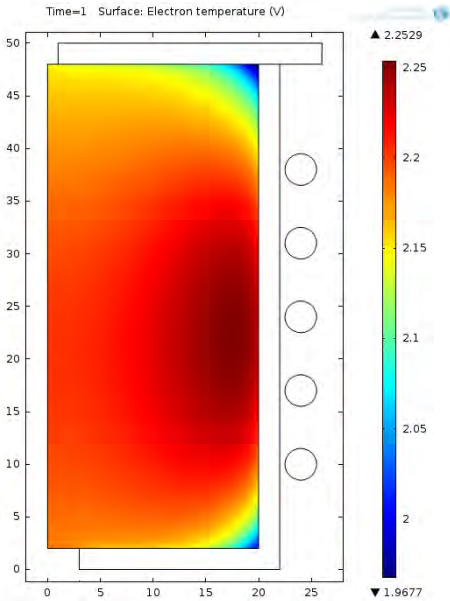
Figure A.5. Electron temperature inside the plasma chamber.

APPENDIX B: RADIO FREQUENCY ION THRUSTER DESIGN, MANUFACTURING AND TESTING

A prototype radio frequency ion thruster has been designed and manufactured. 3D technical drawings of the radio frequency ion thruster are shown in Figure B.1. The inner diameter of the chamber of this thruster is 80 mm.
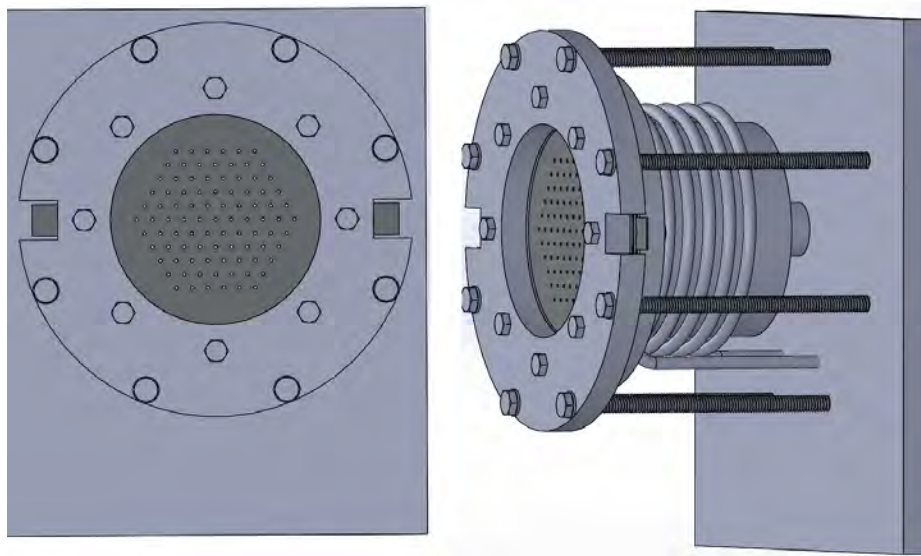
Figure B.1. 3D technical drawings of the radio frequency ion thruster from front and side views.

A 2D drawing and components of the RF ion thruster are shown in Figure B.2. The chamber of the thruster is made of pyrex. The gas inlet is olso made of pyrex and is integrated with the chamber. The gas inlet is close-ended, and there are four holes on the peripheral side of the inlet tube (on the section of the inlet which is inside the chamber). This is to prevent the direct flow of the gas to the outside of the thruster through the grid holes, and to direct the gas flow to the side walls of the chamber. A stainless steel holder cap is glued to the pyrex chamber using high-temperature resistant glue. The grid system is mounted on the holder cap by ceramic screws. The grid system consists of two grids, screen and accelerator. The grids are made of molybdenum. Spacers are made of micanit, a product of mica which can stand high temperatures and voltages. These spacers are placed between the holders

and grids. A holder lid, made of teflon, is placed at the end of the grid system. The gas sealing is achieved by pressing the grids and spacers between the lid and cap holders. The reason for using ceramic screws is to maintain the electric insulation of the grids. The chamber and grid system are mounted to a teflon back plate using metallic screws. The RF antenna is also mounted to the back plate.
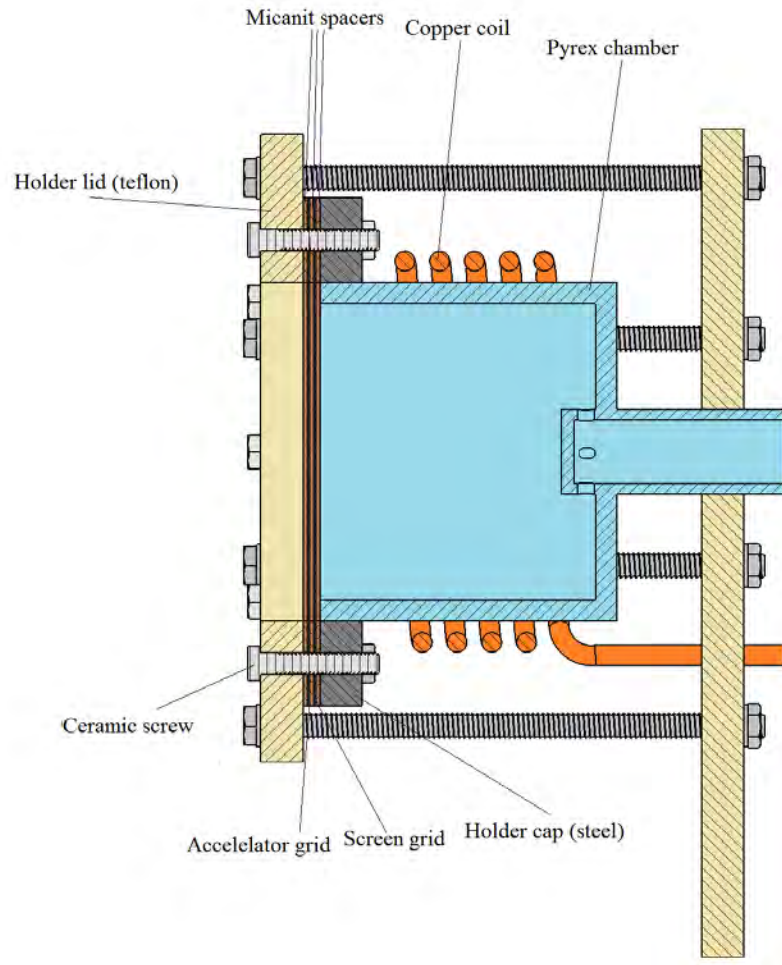
Figure B.2. 2D drawing and components of the RF ion thruster.

Pictures of the manufactured RF ion thruster and during experimental studies are shown in Figure B.3. As can be seen in this figure, the ICP plasma is generated inside the chamber of the thruster. After the plasma generation, the high positive potential is applied to the screen grid, and the accelerator grid is biased negatively with respect to ground. The juts of the grids, which the electric cables are connected to them, are exposed to the background gas of the vacuum chamber. This causes arcing problems on the jut of the screen grid that is connected to the high positive potential. Due to

this problem, the high potential was not reachable in the experiments, and no plume was observed in thruster tests.

Figure B.3. Manufactured RF ion thruster from side view and during experimental studies.

REFERENCES

1. Goebel, D. M. and I. Katz, *Fundamentals of Electric Propulsion: Ion and Hall Thrusters*, Wiley, 2008.

2. Martinez-Sanchez, M. and J. E. Pollard, "Spacecraft Electric Propulsion-An Overview", *Journal of Propulsion and Power*, Vol. 14, No. 5, pp. 688–699, 1998.

3. Weatherford, B. R., *Development and Study of an Electron Cyclotron Resonance Waveguide Plasma Cathode for Electric Propulsion Applications*, Ph.D. thesis, University of Michigan, Ann Arbor, MI, USA, 2011.

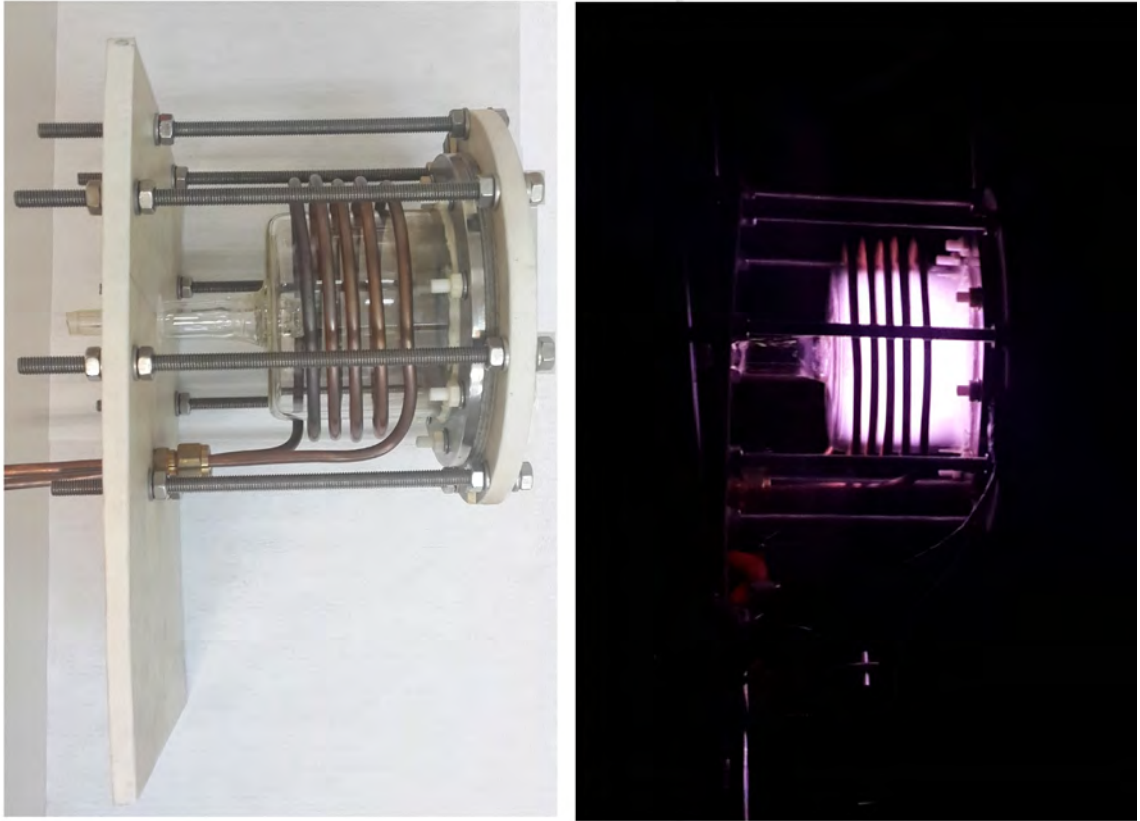4. Reader, P. D., D. P. White, and G. C. Isaacson, "Argon Plasma Bridge Neutralizer Operation with a 10-cm-Beam-Diameter Ion Etching Source", *Journal of Vacuum Science and Technology*, Vol. 15, No. 3, pp. 1093–1095, 1978.

5. Othmer, C., K.-H. Glassmeier, U. Motschmann, and I. Richter, "Numerical Parameter Studies of Ion-Thruster-Beam Neutralization", *Journal of Propulsion and Power*, Vol. 19, No. 5, pp. 953–963, 2003.

6. Patterson, M. J. and K. Mohajeri, "Neutralization Optimization", *22nd International Electric Propulsion Conference,Viareggio, Italy*, 1991, IEPC-91-151.

7. Foster, J. E., G. J. Williams, and M. J. Patterson, "Characterization of an Ion Thruster Neutralizer", *Journal of Propulsion and Power*, Vol. 23, No. 4, pp. 828–835, 2007.

8. Othmer, C., K. Glassmeier, U. Motschmann, J. Schüle, and C. Frick, "Three-Dimensional Simulations of Ion Thruster Beam Neutralization", *Physics of Plasmas*, Vol. 7, p. 5242, 2000.

9. Wheelock, A., D. L. Cooke, and N. A. Gatsonis, "Investigation of Ion Beam Neu-

tralization Processes with 2D and 3D PIC Simulations", *Computer Physics Communications*, Vol. 164, No. 1, pp. 336–343, 2004.

10. Weis, S., K. H. Schartner, H. Löb, and D. Feili, "Development of a Capacitively Coupled Insert-Free RF-Neutralizer", *29th International Electric Propulsion Conference, Princeton, NJ, USA*, 2005, IEPC-2005-086.

11. Longmier, B. W. and N. Hershkowitz, "Electrodeless Plasma Cathode for Neutralization of Ion Thrusters", *41st Joint Propulsion Conference, Tucson, AZ, USA*, 2005, AIAA-2005-3856.

12. Hatakeyama, T., M. Irie, H. Watanabe, A. Okutsu, J. Aoyagi, and H. Takegahara, "Preliminary Study on Radio Frequency Neutralizer for Ion Engine", *30th International Electric Propulsion Conference, Florence, Italy*, 2007, IEPC-2007-226.

13. Godyak, V., Y. Raitses, and N. J. Fisch, "RF Plasma Cathode-Neutralizer for Space Applications", *30th International Electric Propulsion Conference, Florence, Italy*, 2007, IEPC-2007-266.

14. Hidaka, Y., J. Foster, W. Getty, R. Gilgenbach, and Y. Lau, "Performance and Analysis of an Electron Cyclotron Resonance Plasma Cathode", *Journal of Vacuum Science and Technology A*, Vol. 25, No. 4, pp. 781–790, 2007.

15. Weatherford, B., J. Foster, and H. Kamhawi, "Electron Current Extraction from a Permanent Magnet Waveguide Plasma Cathode", *Review of Scientific Instruments*, Vol. 82, No. 9, p. 093507, 2011.

16. Watanabe, H., T. Hatakeyama, M. Irie, A. Okutsu, T. Tsukahara, J. Aoyagi, and H. Takegahara, "Study on Radio Frequency Cathode for Ion Engines", *Transactions of the Japan Society for Aeronautical and Space Sciences, Space Technology Japan*, Vol. 7, No. ists26, pp. 53–58, 2009.

17. Watanabe, H., T. Okuma, J. Aoyagi, and H. Takegahara, "Research and Develop-

ment on Inductively Coupled Plasma Cathode for Ion Engines", *31st International Electric Propulsion Conference, Florence, Italy*, 2009, IEPC-2009-027.

18. Raitses, Y., J. K. Hendryx, and N. J. Fisch, "A Parametric Study of Electron Extraction from a Low Frequency Inductively Coupled RF-Plasma Source", *31st International Electric Propulsion Conference, Florence, Italy*, 2009, IEPC-2009-024.

19. Weatherford, B., E. Barnat, and J. Foster, "Two-dimensional Laser Collision-Induced Fluorescence Measurements of Plasma Properties Near an RF Plasma Cathode Extraction Aperture", *Plasma Sources Science and Technology*, Vol. 21, No. 5, p. 055030, 2012.

20. Zhu, Y., *Modeling of a Microwave Plasma Electron Source for Neutralization of Ion Thrusters*, Ph.D. thesis, Université Toulouse III-Paul Sabatier, Toulouse, France, 2013.

21. Chabert, P., N. Braithwaite, and N. S. J. Braithwaite, *Physics of Radio-Frequency Plasmas*, Cambridge University Press, 2011.

22. Baalrud, S., N. Hershkowitz, and B. Longmier, "Global Nonambipolar Flow: Plasma Confinement where All Electrons Are Lost to one Boundary and All Positive Ions to Another Boundary", *Physics of Plasmas*, Vol. 14, No. 4, p. 042109, 2007.

23. Longmier, B. W., *Plasma Sheath Behavior in a Total Nonambipolar Radio Frequency Generated Plasma Electron Source*, Ph.D. thesis, University of Wisconsin-Madison, USA, 2007.

24. Song, B., N. d'Angelo, and R. Merlino, "On Anode Spots, Double Layers and Plasma Contactors", *Journal of Physics D: Applied Physics*, Vol. 24, No. 10, p. 1789, 1991.

25. Sanduloviciu, M., C. Borcia, and G. Leu, "Self-Organization Phenomena in Current Carrying Plasmas Related to the Non-Linearity of the Current Versus Voltage Characteristic", *Physics Letters A*, Vol. 208, No. 1, pp. 136–142, 1995.

26. Baalrud, S., B. Longmier, and N. Hershkowitz, "Equilibrium States of Anodic Double Layers", *Plasma Sources Science and Technology*, Vol. 18, No. 3, p. 035002, 2009.

27. Park, Y.-S., D.-H. Choi, K.-J. Chung, and Y.-S. Hwang, "Study on Expansion of Electron Sheath and Breakdown in it", *Bulletin of the American Physical Society*, Vol. 55, 2010.

28. Torven, S., "Formation of Double Layers in Laboratory Plasmas", *Wave Instabilities in Space Plasmas*, pp. 109–128, Springer, 1979.

29. Wagenaars, E., *Plasma Breakdown of Low-Pressure Gas Discharges*, Ph.D. thesis, Technische Universiteit Eindhoven, Eindhoven, Netherlands, 2006.

30. Braithwaite, N. S. J., "Introduction to Gas Discharges", *Plasma Sources Science and Technology*, Vol. 9, No. 4, p. 517, 2000.

31. Carlqvist, P., "Some Theoretical Aspects of Electrostatic Double Layers", *Wave Instabilities in Space Plasmas*, Vol. 74, p. 83, 1979.

32. Raadu, M. A., "The Physics of Double Layers and Their Role in Astrophysics", *Physics Reports*, Vol. 178, No. 2, pp. 25–97, 1989.

33. Langmuir, I., "The Interaction of Electron and Positive Ion Space Charges in Cathode Sheaths", *Physical Review*, Vol. 33, No. 6, p. 954, 1929.

34. Montgomery, D. and G. Joyce, "Shock-Like Solutions of the Electrostatic Vlasov Equation", *Journal of Plasma Physics*, Vol. 3, No. 01, pp. 1–11, 1969.

35. Block, L. P., "A Double Layer Review", *Astrophysics and Space Science*, Vol. 55,

No. 1, pp. 59–83, 1978.

36. Raadu, M. and J. Rasmussen, "Dynamical Aspects of Electrostatic Double Layers", *Astrophysics and Space Science*, Vol. 144, No. 1-2, pp. 43–71, 1988.

37. Coakley, P. and N. Hershkowitz, "Laboratory Double Layers", *Physics of Fluids*, Vol. 22, No. 6, pp. 1171–1181, 1979.

38. Cartier, S. L. and R. L. Merlino, "Anode-Type Double Layers in a Nonuniform Magnetic Field", *Physics of Fluids*, Vol. 30, No. 8, pp. 2549–2560, 1987.

39. Conde, L. and L. Leon, "Multiple Double Layers in a Glow Discharge", *Physics of Plasmas*, Vol. 1, No. 8, pp. 2441–2447, 1994.

40. Gurlui, S., M. Agop, M. Strat, G. Strat, and S. Bci, "Experimental and Theoretical Investigations of Anode Double Layer", *Japanese Journal of Applied Physics*, Vol. 44, No. 5R, p. 3253, 2005.

41. Strat, M., G. Strat, and S. Gurlui, "Basic Processes in Discharge Plasma Double Layers", *Journal of Physics D: Applied Physics*, Vol. 32, No. 1, p. 34, 1999.

42. Alfvén, H., "Double Layers and Circuits in Astrophysics", *IEEE Transactions on Plasma Science*, Vol. 14, No. 6, pp. 779–793, 1986.

43. Boylestad, R. L., *Introductory Circuit Analysis*, Prentice Hall, 10th edition, 2002.

44. Goebel, D. M., "Analytical Discharge Model for RF Ion Thrusters", *IEEE Transactions on Plasma Science*, Vol. 36, No. 5, pp. 2111–2121, 2008.

45. Conde, L., L. Ibanez, and C. Ferro-Fontan, "Electron Impact Ionization by Drifting Electrons in Weakly Ionized Plasmas", *Physical Review E*, Vol. 64, No. 4, p. 046402, 2001.

46. Song, B., N. D'Angelo, and R. L. Merlino, "Stability of a Spherical Double Layer

Produced Through Ionization", *Journal of Physics D: Applied Physics*, Vol. 25, No. 6, p. 938, 1992.

47. Demirel, Y., *Nonequilibrium Thermodynamics: Transport and Rate Processes in Physical, Chemical and Biological Systems*, Elsevier, second edition, 2007.

48. Holubec, V., *Non-equilibrium Energy Transformation Processes: Theoretical Description at the Level of Molecular Structures*, Springer, 2014.

49. Pierrard, V. and M. Lazar, "Kappa Distributions: Theory and Applications in Space Plasmas", *Solar Physics*, Vol. 267, No. 1, pp. 153–174, 2010.

50. Livadiotis, G. and D. McComas, "Understanding Kappa Distributions: A Toolbox for Space Science and Astrophysics", *Space Science Reviews*, Vol. 175, No. 1-4, pp. 183–214, 2013.

51. Zia, R. and B. Schmittmann, "Towards a Classification Scheme for Non-Equilibrium Steady States", *Physics Procedia*, Vol. 7, pp. 112–115, 2010.

52. Piasecki, J. and R. Soto, "Approach to a Non-Equilibrium Steady State", *Physica A: Statistical Mechanics and its Applications*, Vol. 369, No. 2, pp. 379–386, 2006.

53. Wang, J.-T., *Nonequilibrium Nondissipative Thermodynamics: With Application to Low-pressure Diamond Synthesis*, Springer, 2002.

54. Leubner, M., "Fundamental Issues on Kappa-Distributions in Space Plasmas and Interplanetary Proton Distributions", *Physics of Plasmas*, Vol. 11, No. 4, pp. 1308–1316, 2004.

55. Ermakova, N. and E. Antonova, "Particle Acceleration by Double Layers During Kappa Distributions", *Geomagnetism and Aeronomy*, Vol. 47, No. 4, pp. 423–428, 2007.

56. Hellberg, M., R. Mace, T. Baluku, I. Kourakis, and N. Saini, "Comment on Math-

ematical And Physical Aspects of Kappa Velocity Distribution [Phys. Plasmas14, 110702 (2007)]", *Physics of Plasmas*, Vol. 16, No. 9, p. 094701, 2009.

57. Livadiotis, G. and D. McComas, "Beyond Kappa Distributions: Exploiting Tsallis Statistical Mechanics in Space Plasmas", *Journal of Geophysical Research: Space Physics*, Vol. 114, No. A11, 2009.

58. Livadiotis, G. and D. McComas, "Invariant Kappa Distribution in Space Plasmas Out of Equilibrium", *The Astrophysical Journal*, Vol. 741, No. 2, p. 88, 2011.

59. Lieberman, M. A. and A. J. Lichtenberg, *Principles of Plasma Discharges and Materials Processing*, Wiley, second edition, 2005.

60. "Biagi-v8.9 Database", 2011, `http://www.lxcat.net`, [Accessed at June 2015].

61. Udiljak, R., D. Anderson, M. Lisak, V. Semenov, and J. Puech, "Improved Model for Multipactor in Low Pressure Gas", *Physics of Plasmas*, Vol. 11, No. 11, pp. 5022–5031, 2004.

62. "MFJ VersaTuner V Model MFJ-989D Instruction Manual", *MFJ Enterprises INC.*, 2014.

63. Satır, M., *Plasma Diagnostics with Retarding Potential Analyzer and Langmuir Probe*, Master's thesis, Bogazici University, Istanbul, Turkey, *In preparation*.